ABSTRACT

Title of Dissertation: DYNAMICS, ESTIMATION, AND CONTROL FOR STABILIZING THE ATTITUDE AND SHAPE OF A FLEXIBLE SPACECRAFT

Curtis Alan Merrill
Doctor of Philosophy, 2024

Dissertation Directed by: Professor Derek A. Paley
Department of Aerospace Engineering

Advances in technology have enabled the development of large spacecraft structures such as solar sails, expansive antennas, and large solar arrays. A critical design constraint for these structures is mass, necessitating lightweight construction which, in turn, increases structural flexibility. This flexibility poses significant challenges resulting from structural deformations and vibrations that complicate attitude control and can degrade the performance and lifespan of the spacecraft. The goal of this research is to develop estimation and control strategies to mitigate the effects of spacecraft flexibility.

A flexible spacecraft model is derived using a hub and appendage framework. In this model one or more flexible appendages attach to a central rigid hub. The model represents the appendages as a discretized set of flexibly connected elements called panels. Stiff springs connect the panels, and the dynamic model of the system's internal forces and moments uses coordinates in the hub's reference frame. Reaction wheels on the hub perform attitude control, while distributed pairs of magnetic torque rods on the appendage influence its shape.

Initially, the model restricts flexibility to one direction, resulting in a planar model. A Lyapunov-based control design provides a feedback law for the reaction wheel and torque rods in the planar model. Numerical simulations demonstrate that the proposed controller meets the control objectives and compares favorably to other controllers. An Extended Kalman Filter is applied to the system to perform state estimation and output feedback control, which performs at nearly the same level as state feedback control.

The modeling framework and flexibility are extended to three dimensions. The development of a control law for the magnetic torque rods considers the attitude control of a single panel using two magnetic torque rods. Due to the system being underactuated, the attitude error is defined in terms of the reduced-attitude representation. Lyapunov analysis yields a control law that stabilizes the reduced attitude and angular velocity of a rigid panel using only two magnetic torque rods. Numerical simulations validate the control law's performance for a single panel. This control law is then applied to the flexible appendage to stabilize its shape. Numerical simulations show that this implementation of shape control significantly reduces structural deformations and dampens structural oscillations compared to scenarios without shape control.

To perform state estimation of the high-dimensional flexible spacecraft model, dynamic mode decomposition generates a reduced order model that is linear with respect to the evolution of the resulting modes. A Kalman filter estimates the mode amplitudes of the reduced order model from a limited set of measurements, enabling the reconstruction of the entire system state. The optimization of the number and placement of sensors maximizes the observability of the observer. Numerical simulations demonstrate that this framework yields accurate state estimates with reduced computational cost.

Dynamics, Estimation, and Control for Stabilizing the Attitude and Shape of a Flexible Spacecraft

by

Curtis Alan Merrill

Dissertation submitted to the Faculty of the Graduate School of the
University of Maryland, College Park in partial fulfillment
of the requirements for the degree of
Doctor of Philosophy
2024

Advisory Committee:
  Professor Derek A. Paley, Chair/Advisor
  Professor Harry Dankowicz, Dean's Representative
  Professor Christine M. Hartzell
  Professor Robert M. Sanner
  Professor Michael Otte
  Professor Yancy Diaz-Mercado

Dedication

To my father, Douglas.

Acknowledgments

I am grateful to my advisor, Dr. Derek Paley, for giving me the opportunity to pursue a PhD in his laboratory. I am especially grateful for his unwavering support and flexibility during some of the most challenging periods of my life. His understanding and accommodation allowed me to navigate through personal difficulties while continuing my research. As a researcher, Dr. Paley's guidance in demonstrating how to distill complex problems into their fundamental, solvable pieces has been invaluable and enabled me to tackle problems I would have never thought possible.

I am grateful to the remainder of my dissertation committee, Dr. Sanner, Dr. Otte, Dr. Hartzell, Dr. Diaz-Mercado, and Dr. Dankowicz for their generous allocation of time, insightful feedback, and constructive criticism throughout this process. I would also like to thank Dr. Sedwick for his advice, feedback, and help in giving direction to my research.

I would like to acknowledge my father, Douglas, who passed away during my PhD studies. His endless curiosity and desire to understand how things worked instilled a love of learning in me. His lifelong enthusiasm in supporting my endeavours has always given me the confidence to reach higher.

To my mother and siblings, your unwavering support and encouragement have been a continual source of energy when I felt I didn't have any left. To my brother Bryan for treading the path before me. To my sister Tiffany, for knowing all the answers to questions about being a parent. To my sister Nicole, for always looking on the bright side. To my sister Melanie, for your empathy and for caring for Dad. And to my brother Jeff, for always making sure I wasn't burning myself out.

Finally, to my son, Leo, born during my PhD journey, your boundless enthusiasm and cheery attitude have been a source of joy and light, even during the most stressful times. And to my incredible wife, Kelly, words cannot fully capture my gratitude for your tireless support. You have always made me feel like a great husband and father even when I felt I had little to give. Your unwavering belief in me provided the foundation that made it possible to navigate the simultaneous challenges of life's difficulties and rigors of a PhD program. I could not have achieved this without you.

Table of Contents

List of Tables

List of Figures

Chapter 1: Introduction

Advances in technology have significantly expanded the potential applications for large spacecraft structures. Examples include spacecraft equipped with solar sails, expansive antennas, large solar arrays to meet substantial energy requirements, extended truss structures, and manipulator arms.

One of the most critical and demanding constraints in spacecraft design is mass. Therefore, large structures intended for space must often prioritize lightweight construction to adhere to mass constraints. The trade-off of achieving a large and lightweight structure is increased structural flexibility. Additionally, to accommodate volumetric constraints during launch, many structures are designed to be folded for launch and subsequently deployed in orbit, intentionally incorporating flexibility at folding points. Consequently, flexibility becomes a crucial consideration for the design and implementation of any large spacecraft structure. However, introducing flexibility complicates both modeling [1] and control [2], presenting a distinct set of challenges. The primary cause of these challenges are structural deformations and vibrations of the spacecraft. For example, attitude maneuvers, which involve changing the orientation of the spacecraft, introduce rotational energy into the structure, leading to bending and vibration. Additionally, in the space environment, significant thermal gradients resulting from solar heating can induce deformations of spacecraft components.

Flexibility poses two notable challenges for spacecraft operation. The first is attitude control. Deformations and oscillations can degrade the performance of an attitude controller which can compromise stability or extend settling times. Second, if the shape of the structure is critical to the spacecraft's function, or if vibrations reduce the lifespan of the structure, any deformations and oscillations degrade spacecraft performance. Addressing these problems cannot be achieved merely by stiffening the structure, as this would lead to increased mass, conflicting with mass constraints. Furthermore, in space, environmental damping is minimal and cannot be relied upon.

This dissertation explores how advanced actuation and control strategies can address the issues of attitude and shape control in flexible spacecraft. By developing these control methods, the objective is to enhance the feasibility and operability of large flexible spacecraft.

1.1 Problem Statement

The modeling framework for a flexible spacecraft used in this dissertation consists of a hub and one or more flexible appendages. The hub represents a rigid primary structure containing most of the subsystems of the spacecraft (power, attitude control, thermal control, on-board computer, scientific payloads, etc.) The appendage(s) is a flexible structure that is attached to the hub, and could represent a large solar array, an antenna, a manipulator arm, etc. Assume the appendage has some natural restoring force that causes it to have an equilibrium configuration. In this dissertation, the appendage is considered as a thin planar structure, with its equilibrium corresponding to a flat configuration. See Fig. 1.1 for a sample drawing.

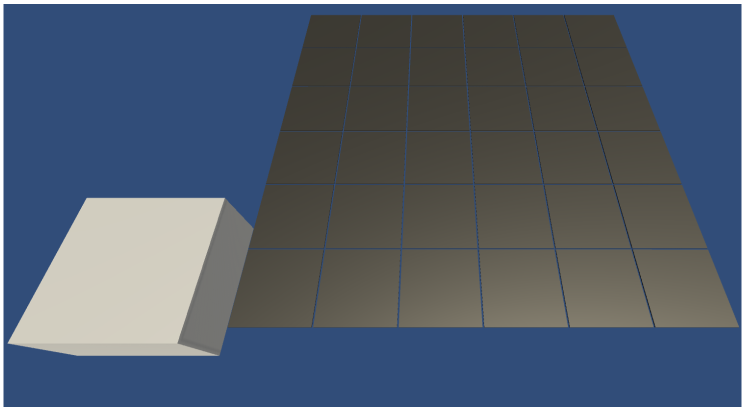

Figure 1.1: Spacecraft with hub and thin planar appendage concept drawing

As the hub performs an attitude maneuver and the spacecraft reorients, the angular impulse will excite the flexible modes of the appendage, inducing vibrations. These vibrations will cause periodic deformations of the appendage. The vibrations of the appendage will also transfer angular momentum back into the hub at their connection which affects the attitude of the hub and its control.

The actuation framework considered in this dissertation is as follows. The hub is equipped with a set of reaction wheels that enable it to fully control the attitude of the hub. The appendage has magnetic torque rods distributed across its structure that are able to generate small moments to influence the shape the of the appendage.

The objective of an attitude control law is to drive the spacecraft's attitude to a specified trajectory while being robust to disturbances induced by appendage vibrations. In this dissertation, the reference trajectory used for numerical simulations is a nadir-pointing reference, meaning the spacecraft is oriented directly towards the center of the Earth, aligned with the gravity vector. The objective of the torque rod control is to stabilize the shape of the spacecraft. Specifically, if the appendage is perturbed from its equilibrium shape by induced vibrations, the controller should dampen the vibrations and restore the appendage to its equilibrium state.

In practice, the information available about the state of a system is limited to the measurements taken from the system. Typically, controllers require knowledge of the entire system state to function effectively. To implement this type of control, an observer is needed. An observer assimilates system measurements and outputs an estimate of the full system state. This state estimate is then used as input to a controller in an output feedback framework.

For spacecraft, onboard computational power is severely limited. As the number of states in a system increases, the computational resources required to perform state estimation increase significantly. This can make real-time estimation infeasible if the number of states describing the system becomes too large, as may be the case with large flexible spacecraft.

The primary existing challenges for attitude control and shape stabilization of flexible spacecraft that are addressed in this dissertation are as follows:

1. *Construction of a generalizable flexible spacecraft dynamic model containing the state information required to implement distributed control*
2. *Development of a control law for the magnetic torque rods that is able to influence the local attitude of the appendage such that the shape of the whole appendage is stabilized.*
3. *Demonstration of the performance and impact of shape stabilizing control implemented with magnetic torque rods via numerical simulation.*
4. *Development of an estimation framework such that a high dimensional state space representation of a flexible spacecraft model can be estimated from a limited set of state measurements while minimizing computational resources*

1.2 Relation to Prior Work

The work in this dissertation builds on related research conducted by others. In this section, I highlight some of this research and discuss the contributions of this dissertation in relation to that work. First, I provide an overview of research on attitude and shape control of flexible spacecraft. Second, I review studies on underactuated spacecraft attitude control, including magnetic torque rod actuation as well as reduced actuator usage. Finally, I discuss prior work on dynamic mode decomposition and its application for state estimation.

1.2.1 Attitude and Shape Control of Flexible Spacecraft

Structural oscillation may be mitigated by attitude control laws that minimize excitation. A super-twisting sliding mode control is developed in [3] to simultaneously perform attitude tracking and vibration suppression. An extended disturbance observer and backstepping controller is proposed in [4] for attitude stabilization by rejecting disturbances resulting from the flexible spacecraft. In [5], the flexible appendages are modeled using partial differential equations; distributed and boundary controllers are implemented to compensate for disturbances and suppress vibrations. [6] treats the oscillations as a disturbance and derives a compensator and controller to guarantee robust attitude control. A controller that plans constrained low-jerk maneuvers is provided in [7]. Additional attitude control schemes focused on minimizing vibrations due to structural flexiblity include [2, 8–20].

Another research area involves active vibration suppression using additional actuators. The use of piezoelectric actuators on flexible structures to perform active vibration suppression has been studied. In [21], a constrained torque distribution algorithm with a shape input controller for piezoelectric actuators are used for attitude and shape control. A robust control scheme based on a distributed observer and controller framework is developed in [22], which also uses piezoelectric actuation for flatness control of flexible appendages. However, due to size-at-launch constraints, spacecraft with a large area-to-bus size ratio must be folded and then deployed after launch. Research in deployable space structures, such as [23], studies the deployment dynamics of folded spacecraft structures. Whereas the flexing in large lightweight spacecraft structures occurs in the structure itself, the flexing in a multibody deployable space structure may be more significant at the hinges. Consequently, while piezoelectric actuators may suppress vibrations in a flexible appendage, their utility is limited if the main source of flexibility of a spacecraft is in the interface between bodies, which might occur in a deployable space structure. To better address shape control of a multibody flexible spacecraft, instead of actuating the shape of an appendage, [24] assumes that actuators are mounted on the interface between an appendage and the hub and a control law is proposed to provide attitude and shape control. In [25], a model is formed and a control law proposed where control moment gyros are distributed across the flexible structure to provide vibration suppression. This work is extended in [26], where a global matrix formulation of the dynamics is proposed for a flexible multibodied spacecraft. In the case where the number of appendages is large or where the area-to-bus size ratio is large, the added mass for each additional actuator may prohibit implementation. One actuation method for shape control that has not been investigated is the use of magnetic torque rods to perform shape control, which is a primary subject of this dissertation.

In this dissertation I derive a dynamic spacecraft model using a hub and flexible appendage framework. The hub is actuated by reaction wheels to manage spacecraft attitude, while magnetic torque rods actuate the appendage to stabilize its shape. Flexibility is modeled by discretizing the appendage into flexibly connected elements. I initially restrict the flexibility to one dimension coinciding with the orbital plane, thus restricting the spacecraft dynamics to that plane. Using Lyapunov analysis, I derive a nonlinear state feedback control law that drives the spacecraft's attitude to a reference and stabilizes the appendage. To validate this control law, I conduct numerical simulations and compare its performance against various linear control strategies. I then implement an extended Kalman filter for state estimation, demonstrating the control law's robustness in an output feedback framework subjected to measurement noise [27].

I extend the discretization of the flexible appendage to two directions and employ a three-dimensional element connection model to capture its full flexibility across three degrees of freedom. The dynamics and control inputs for both attitude and shape are accordingly extended into three dimensions. I apply magnetic torque rod control to the flexible appendage to perform shape control. Numerical simulations confirm that integrating shape control into the flexible appendage significantly mitigates structural deformations and oscillations in response to various disturbances. However, this improvement comes at the cost of increased control effort required from the reaction wheels.

1.2.2 Underactuated Attitude Control of Spacecraft

The exploration of reduced actuator usage in research is significant not only due to its potential for weight saving potential in small spacecraft, but also because it can demonstrate the robustness of a spacecraft in the event of actuator failure. Extensive research has addressed attitude control using only two reaction wheels. In [28], a time-varying feedback law is proposed that exponentially stabilizes the attitude of a rigid spacecraft. In [29], it is shown that the angular velocity of a rigid spacecraft can be stabilized with two constant torques. One approach demonstrated in [30] is to stabilize a pointing axis of the spacecraft and ignore rotations about that axis. Another area of research evaluates using two control moment gyros instead of reaction wheels. In [31], conditions are defined under which angular velocity damping can occur using two single-gimbal control moment gyros. Full three-axis control was demonstrated in [32] using a backstepping controller under the condition that the initial total angular momentum is zero. In [33], the angular momentum restriction is loosened using the addition of a sliding-mode control to stabilize the underactuated axis. Although extensive research exists on underactuated systems employing more conventional actuators, there is comparatively limited investigation into underactuated control utilizing magnetic actuation.

Magnetic torque rods have been employed on spacecraft from very early on. The primary advantages of using magnetic actuators are that they are lightweight, small, require no consumables, and are reliable due to their lack of moving parts. One of the disadvantages to using magnetic actuation is that it renders a system inherently underactuated due to control authority only being available orthogonal to the local magnetic field. One of the earliest uses of magnetic torque rods was dumping momentum from a momentum storage device, like a reaction wheel, as in [34]. Other approaches for this application include [35], which uses the periodicity of orbital motion to analyze the problem, and [36], which uses techniques from optimal control. Magnetic actuation has also traditionally been used for the initial detumbling of a spacecraft after deployment. The most common method used is called B-dot control, which uses the rate of change of the magnetic field to determine the actuation torque. Extensive analysis has been performed to validate this control, [37–39]. More recently, there have been efforts to investigate full three-axis attitude control for spacecraft using magnetic actuation. In [40], the problem is represented by a linear time-varying system, which enables controllability analysis to be performed and, for a certain type of orbit, magnetic actuation is shown to make the system controllable. Nonlinear analysis demonstrates attitude control under the disturbance of gravity gradient torque in [41]. Other work studying three-axis attitude control using only magnetic actuation includes [42–44]. Stabilizing the attitude of spinning spacecraft has also been studied [45–49]. The consideration of duty cycling between taking measurements of the magnetic field and actuating magnetic torque rods is explored in [50, 51]. In [52] attitude control using three magnetic torque rods and one reaction wheel to minimize flexible structure excitation is explored.

While reduced actuator attitude control and magnetic actuation have been thoroughly investigated separately, there is a lack of research into magnetic attitude control with fewer than three magnetic torque rods. Detumbling a satellite with a single magnetic torque rod using a model predictive controller is shown in [53], but there is an absence of attitude stabilization. Attitude stabilization with two magnetic torque rods is investigated in [54] using controllability analyses of the linearized dynamics, but the result only holds for a specific attitude reference. The use of only two magnetic torque rods to stabilize the pointing of a body in space is investigated in this dissertation.

In this dissertation I investigate controlling the reduced attitude and angular velocity of a rigid body actuated by two magnetic torque rods. Through Lyapunov analysis, I derive a nonlinear feedback control law that effectively stabilizes the reduced attitude and angular velocity of the rigid element using only two magnetic torque rods. I validate this control law through numerical simulations and demonstrate its robustness in the presence of saturation nonlinearities. [55]

1.2.3 Shape Estimation of Flexible Spacecraft

In order for any attitude or shape control laws to be effectively applied, the state of the spacecraft including its shape must be known. In the case of a deployable structure with connected segments, the state of each of the segments may be required for distributed control. However, if a high dimensional state is needed to represent the structural dynamics, this can require an increasingly significant amount of computation power to perform state estimation. Due to the limited computation power available to a spacecraft in orbit and the need to perform estimation in real time, a high dimensional state may make state estimation and thus output feedback control infeasible. In [56] an Eigensystem realization algorithm is used to generate a reduced order model of a flexible spacecraft in order to estimate shape in real time, although it is focused primarily on modeling between input and output space which may not be sufficient for implementing control. To reconstruct the shape of a flexible spacecraft structure, [57] investigates the use of sun sensors, while [58] employs range images. [59] uses an interpolation of displacement measurements in conjunction with a filter for shape estimation. To estimate the dynamics of a flexible spacecraft, an adaptive scheme is used in [1] to learn unknown physical parameters of the spacecraft. Parameter estimation of flexible spacecraft models is further explored in [60–62].

Modal decomposition encompasses a common class of methods for making algorithms on high-dimensional systems more computationally tractable. The goal of modal decomposition is to represent a high-dimensional system with a relatively small number of modes that captures the relevant behavior of the system. Some eixsting approaches for modal decomposition and model reduction include proper orthogonal decomposition (POD) and the Eigensystem realization algorithm (ERA). POD attempts to capture the most energetic spatial modes from a dataset [63] but ignores the temporal behavior of the system. The ERA assumes the underlying system is linear and can yield inaccuarte representations if the system is too nonlinear. One method that has gained popularity, particularly in the field of fluid mechanics, that captures spatial and temporal structures of a system and lends itself well to state estimation is dynamic mode decomposition (DMD) [64]. DMD is a data-driven algorithm that was first developed for analyzing fluid flows. It is closely related to the Koopman operator, which is a way to represent a finite-dimensional nonlinear system as an infinite-dimensional linear system. The goal of DMD is to decompose data from time series measurements into modes that capture the underlying dynamics of the system [65]. DMD may also be used to perform state estimation by using measurements of the system to estimate the DMD mode amplitudes using a Kalman filter, which can be used to estimate the full system state. This framework, described in [66], is referred to as the DMD Kalman filter and, if the DMD modes are an approximation of the Koompan modes, is equivalent to the Koopman-Kalman filter [66]. While DMD is popular in the field of fluid mechanics, it has not received the same level of attention or use in other fields. However, the model-order reduction and linear estimation framework it enables make it a promising approach to apply to state estimation of flexible spacecraft.

In this dissertation I employ dynamic mode decomposition to generate a data driven modal decomposition of the flexible spacecraft model. The modal decomposition yields a reduced order model such that the amplitudes of the modes used to form the model evolve linearly with time. The reduced order model enables full state estimation from a limited set of measurements. I validate application of this framework to this problem through numerical simulations which demonstrate accurate state estimates with measurement noise and a substantial reduction in model order. Leveraging this state estimation framework, I optimize the number and placement of sensors to maximize system observability.

1.3 Outline of Dissertation

This dissertation is outlined as follows.

Chapter 2 provides an overview of some of the foundational material useful for subsequent chapters. Orbital and attitude dynamics of spacecraft are reviewed and modeling for magnetic actuation is shown. The procedure for dynamic mode decomposition is also provided.

Chapter 3 derives a planar version of the flexible spacecraft model. Lyapunov analysis yields a nonlinear control law that controls the attitude and shape of the model with state and output feedback.

Chapter 4 extends the flexible spacecraft model to three dimensions. A control law is developed to facilitate shape control using two magnetic torque rods. Numerical simulations confirm the effectiveness and validity of this control law.

Chapter 5 employs dynamic mode decomposition to provide a reduced order model of the spacecraft which enables full state estimation. Numerical simulations validate this approach. The location and number of sensors providing measurements are optimized to maximize system observability.

Chapter 6 summarizes the dissertation and provides suggestions research directions for ongoing and future work.

Chapter 2: Background

This chapter reviews foundational material for the analyses presented in Chapters 3 to 5. I begin by outlining the approach for modeling spacecraft dynamics, including translational dynamics and the use of rotation matrices to represent attitude. I then describe the modeling for Earth's magnetic field and for magnetic torque rods and summarize the inherent challenges associated with utilizing them for attitude control. Lastly I provide an overview of dynamic mode decomposition and review the framework the decomposition provides for performing state estimation using a reduced order model.

2.1 Spacecraft Dynamics and Control

The equations and models fundamental to describing the spacecraft dynamics and control used in this dissertation are summarized in this section.

2.1.1 Orbital Dynamics

In this dissertation orbital motion is modeled using the two-body problem. Specifically, the translational motion of a body in orbit is described by

$$\ddot{\boldsymbol{r}} = -\frac{mu}{r^3}\boldsymbol{r}, \tag{2.1}$$

where μ is the gravitational parameter for the orbited body.

2.1.2 Attitude Dynamics on the Special Orthogonal Group

Consider the rotational dynamics of a spacecraft modeled as a rigid body. Consider the Earth-centered inertial (ECI) reference frame $\mathcal{I} = \{\boldsymbol{e}_1, \boldsymbol{e}_2, \boldsymbol{e}_3\}$ and a body-fixed reference frame $\mathcal{B} = \{\boldsymbol{b}_1, \boldsymbol{b}_2, \boldsymbol{b}_3\}$ attached to the center of mass of the spacecraft $\mathcal{B}$. The attitude of the spacecraft relative to the inertial frame can be expressed using several parameterizations, such as Euler angles, quaternions, or modified Rodrigues parameters. A rotation matrix $\boldsymbol{R} \in \mathrm{SO}(3)$ is used here to avoid kinematic singularities and unwinding that can result from other representations [67]. Additionally, it is advantageous because it can be represented in a reduced form for applications such as pointing, where not all degrees of freedom need to be considered. This is relevant for controlling the attitude of sections of a flexible structure that are constrained by their attachment to adjoining sections, making rotation matrices a convenient representation of attitude. The special orthogonal group $SO(3)$ is the group of rigid-body rotations defined as $SO(3) = \{\boldsymbol{R} \in \mathbb{R}^{3\times3} | \boldsymbol{R}^T\boldsymbol{R} = \mathcal{I}, \det(\boldsymbol{R}) = 1\}$. The rotational equations of motion on $SO(3)$ are [67]

$$\dot{\boldsymbol{R}} = \boldsymbol{R}\widehat{\boldsymbol{\omega}} \tag{2.2}$$

$$\boldsymbol{J}\dot{\boldsymbol{\omega}} = \boldsymbol{J}\boldsymbol{\omega} \times \boldsymbol{\omega} + \boldsymbol{\tau}, \tag{2.3}$$

where $\boldsymbol{J}$ is the spacecraft moment of inertia, $\boldsymbol{\omega}$ is its angular velocity, and $\boldsymbol{\tau}$ is the total external moment on the spacecraft. The hat map $\wedge : \mathbb{R}^3 \to \mathrm{so}(3)$ transforms a vector into a skew-symmetric matrix, i.e., $\widehat{\boldsymbol{a}}\boldsymbol{b} = \boldsymbol{a} \times \boldsymbol{b}$, i.e.,

$$\widehat{\boldsymbol{a}} = \begin{bmatrix} 0 & -a_3 & a_2 \\ a_3 & 0 & -a_1 \\ -a_2 & a_1 & 0 \end{bmatrix} \tag{2.4}$$

Rotation matrices are fundamental to the flexible spacecraft model defined in Section 4.2, and are used as input to the control law derived in Section 4.3.

2.1.3 Magnetic Torque Rod Control

This dissertation uses a simplified model of the magnetic field of the Earth. Specifically, the magnetic field of the Earth is modeled as a dipole. For an object in orbit at position $\boldsymbol{r} = [x,\ y,\ z]^T$, the magnetic field of the Earth in the inertial frame is [68]

$$\boldsymbol{B}(\boldsymbol{\mu}, \boldsymbol{r}) = \frac{3(\boldsymbol{\mu}_E \cdot \hat{\boldsymbol{r}})\hat{\boldsymbol{r}} - \boldsymbol{\mu}_E}{r^3}. \tag{2.5}$$

Assume the inertial frame is such that $\boldsymbol{\mu}$ is aligned with $\hat{z}$. The magnetic field in Cartesian coordinates is

$$\boldsymbol{B} = \frac{E_m}{r^5}\left[3xz,\ 3yz,\ 3z^2 - r^2\right]^T, \tag{2.6}$$

where $E_m = \mu_0 \mu_E / 4\pi$ specifies the strength of the magnetic field for Earth.

Magnetic torque rods operate by generating a magnetic field that interacts with the local magnetic field; the interaction of these two fields produces a moment. Consider a magnetic dipole generated by magnetic torque rods denoted $\boldsymbol{m}$ and a local magnetic field denoted $\boldsymbol{B}$. The moment $\boldsymbol{\tau}$ that is produced by the magnetic torque rods is [69]

$$\boldsymbol{\tau} = \boldsymbol{m} \times \boldsymbol{B}. \tag{2.7}$$

This equation underscores the primary challenge of using magnetic torque rods for attitude control: control authority is restricted to be orthogonal to the local magnetic field $\boldsymbol{B}$. This problem is exacerbated when there are fewer than three magnetic torque rods. Without loss of generality, assume that there are two magnetic torque rods along the first and second axes of the local body frame. The resulting torque in the body frame is

$$\boldsymbol{\tau} = \boldsymbol{m} \times \boldsymbol{B} = \begin{bmatrix} m_2 B_3 & -m_1 B_3 & m_1 B_2 - m_2 B_1 \end{bmatrix}^T . \tag{2.8}$$

In this case, control authority about the first and second axes is zero when the magnetic field component along the third axis is zero. Additionally, the moment that is generated about the third axis is coupled. For control applications, if m_1 and m_2 are selected to produce specific moments about the first and second axes, there will inherently be an additional undesired moment about the third axis.

The magnetic torque rod modeling is used to define the control inputs to the flexible spacecraft model in Section 4.2 and their limitations are addressed in Section 4.3.

2.2 Data-Driven Analysis Techniques for State Estimation

2.2.1 Dynamic Mode Decomposition

Consider a sequence of evolving measurements arising from either simulated or experimental data. Each individual measurement is referred to as a snapshot and the snapshots at time t_k are denoted $\chi(t_k)$. Assume that the time step between each snapshot is constant, i.e., $t_{k+1} - t_k = \Delta t$ for all k. If there are m snapshots, a matrix can be formed from these snapshots such that kth

column corresponds to the vector of measurements at time k, i.e.,

$$X = \begin{bmatrix} | & | & & | \\ \chi(t_1) & \chi(t_2) & \dots & \chi(t_m) \\ | & | & & | \end{bmatrix}. \tag{2.9}$$

Next, two data matrices are formed from the sequence of snapshots such that the kth column in the second matrix corresponds to the advancement in time of the kth column of the first matrix by Δt.

$$X_0 = \begin{bmatrix} | & | & & | \\ \chi(t_1) & \chi(t_2) & \dots & \chi(t_{m-1}) \\ | & | & & | \end{bmatrix} \tag{2.10}$$

$$X_1 = \begin{bmatrix} | & | & & | \\ \chi(t_2) & \chi(t_3) & \dots & \chi(t_m) \\ | & | & & | \end{bmatrix} \tag{2.11}$$

The goal of dynamic mode decomposition is to find an eigendecomposition of the matrix A that linearly approximates the evolution of the dynamics of the system by one time step Δt, i.e,. $X_1 = AX_0$. The best fit in the least-squares sense for A can be computed using the psuedoinverse denoted †, i.e., $A = X_1 X_0^{\dagger}$. However, if the dimension of X_0 is very large, this may become unreasonable to compute. Instead, the singular value decomposition (SVD) of X_0 is taken, i.e.,

$$X_0 = U\Sigma V^* \tag{2.12}$$

where $*$ denotes the conjugate transpose. The psuedoinverse of the SVD may be taken as $X_0^{\dagger} = V\Sigma^{-1}U^*$, yielding

$$A = X_1 V\Sigma^{-1}U^*. \tag{2.13}$$

An optimal low-dimensional representation of A denoted $\tilde{A}$ may be defined by the columns of U is [64]

$$\tilde{A} = U^* A U = U^* X_1 V \Sigma^{-1}. \tag{2.14}$$

Let Λ be the eigenvalues of $\tilde{A}$ in matrix form and W the matrix of right eigenvectors of $\tilde{A}$. The DMD eigenvalues are given by Λ and the DMD modes given by [64]

$$\Phi = UW. \tag{2.15}$$

Let $\alpha(t_k)$ represent the mode amplitudes of the vector snapshot $\chi(t_k)$ in the DMD basis, i.e. $\chi(t_k) \approx \Phi\alpha(t_k)$. Then the approximate solution for the time evolution of snapshots can be reconstructed by [64]

$$\chi(t_k) \approx \Phi\Lambda^{(t_k - t_1)/\Delta t}\alpha(t_1) \tag{2.16}$$

The degree to which the DMD modes and eigenvalues represent the system dynamics is dependent on the linearity of the system. If the system is linear, only the mode amplitudes depend on the initial condition and the system dynamics may be accurately reconstructed via Eq. (2.16). The more nonlinear the system is, the more that the modes and eigenvalues obtained via DMD will also depend on the initial condition of the dataset [70].

2.2.2 Mode Amplitude Kalman Filter

According to the Koopman observer framework [66], a subset of measurements from the system can be utilized in conjunction with the DMD modes in a linear observer to estimate the mode amplitudes of the DMD representation. These estimated amplitudes can be then used to reconstruct the complete state of the original system. This process is performed as follows.

Consider a matrix C that is formed from the columns of the DMD modes Φ [66]

$$\begin{aligned} &\left.C_i = \boldsymbol{\phi}_i\right\} && \text{if } \boldsymbol{\phi}_i \text{ is real} \\ &\left.\begin{aligned} C_i &= \mathrm{Re}(\boldsymbol{\phi}_i) \\ C_{i+1} &= \mathrm{Im}(\boldsymbol{\phi}_i) \end{aligned}\right\} && \text{if } \boldsymbol{\phi}_i \text{ and } \boldsymbol{\phi}_{i+1} \text{ are complex conjugates.} \end{aligned} \tag{2.17}$$

Let $\boldsymbol{z}_k$ denote a vector of DMD mode amplitudes. The state $\boldsymbol{\eta}_k$ of the underlying system at timestep k can be estimated from the mode amplitudes by

$$\hat{\boldsymbol{\eta}}_k \approx C\boldsymbol{z}_k. \tag{2.18}$$

Consider also a block diagonal matrix F that is formed from the DMD eigenvalues [66] such that F has a diagonal entry $F_{i,i} = \lambda_i$, if λ_i is real, and block diagonal entry

$$\begin{bmatrix} F_{i,i} & F_{i,i+1} \\ F_{i+1,i} & F_{i+1,i+1} \end{bmatrix} = \begin{bmatrix} \mathrm{Re}(\lambda_i) & \mathrm{Im}(\lambda_i) \\ -\mathrm{Im}(\lambda_i) & \mathrm{Re}(\lambda_i) \end{bmatrix} \tag{2.19}$$

if λ_i and λ_{i+1} are complex conjugates. The matrix F represents a linear operator that advances the vector of mode amplitudes $\boldsymbol{z}_k$ forward in time by one timestep, i.e.,

$$\boldsymbol{z}_k = F\boldsymbol{z}_{k-1}. \tag{2.20}$$

The matrices Eqs. (2.18) and (2.20) define a linear dynamical system where the state is the DMD mode amplitudes and the observation is the state of the underlying system. Assume also that only some subset of the state of the underlying system is measured. Let $\boldsymbol{y}_k \in \mathbb{R}^{n_x}$ denote the portion of the state vector that is measured and $\boldsymbol{x}_k \in \mathbb{R}^{n_y}$ denote the portion that is to be estimated. The state vector $\boldsymbol{\eta}$ is reordered such that the observed portion of the state is partitioned from the unobserved portion of the state [66], i.e.,

$$\boldsymbol{\eta}_k = \begin{bmatrix} | \\ \boldsymbol{y}_k \\ | \\ \boldsymbol{x}_k \\ | \end{bmatrix}. \tag{2.21}$$

Note that when performing DMD, the snapshot matrix containing the training data must similarly be reordered.

$$X = \begin{bmatrix} | & | & & | \\ \boldsymbol{y}(t_1) & \boldsymbol{y}(t_2) & \dots & \boldsymbol{y}(t_m) \\ | & | & & | \\ \boldsymbol{x}(t_1) & \boldsymbol{x}(t_2) & \dots & \boldsymbol{x}(t_m) \\ | & | & & | \end{bmatrix}. \tag{2.22}$$

The C matrix is reordered the same way and partitioned such that the first n_y rows corresponding to the measured states are denoted C_y and the remaining n_x row corresponding to the unmeasured states are denoted C_x. The linear dynamical system may now be written as [66]

$$\boldsymbol{z}_k = F\boldsymbol{z}_{k-1} \tag{2.23a}$$

$$\boldsymbol{y}_k \approx C_y\boldsymbol{z}_k \tag{2.23b}$$

$$\boldsymbol{x}_k \approx C_x\boldsymbol{z}_k \tag{2.23c}$$

If the system given by Eq. (2.23) is observable, then a state observer may be applied to estimate the DMD mode amplitudes. For a linear system subject to Gaussian process and measurement noise, the Kalman filter represents an optimal observer. Consequently, a Kalman filter may be used to estimate the mode amplitude amplitudes given a set of measurements of the underlying system. The Kalman filter of the mode amplitudes is as follows [71]:

Estimate propagation:

$$\hat{\boldsymbol{z}}_{\bar{k}} = F\hat{\boldsymbol{z}}_{k-1} \tag{2.24}$$

$$P_{\bar{k}} = FP_{k-1}F^T + Q \tag{2.25}$$

$$\tag{2.26}$$

Kalman Gain:

$$K_k = P_{\bar{k}}C_y\left(C_yP_{\bar{k}}C_y^T + R\right)^{-1} \tag{2.27}$$

Measurement assimilation:

$$\hat{\boldsymbol{z}}_k = \hat{\boldsymbol{z}}_{\bar{k}} + K(\boldsymbol{y}_k - C_y\hat{\boldsymbol{z}}_{\bar{k}}) \tag{2.28}$$

$$P_k = (I - KC_y)P_{\bar{k}} \tag{2.29}$$

Estimate of $\boldsymbol{x}$:

$$\hat{\boldsymbol{x}}_k = C_x\hat{\boldsymbol{z}}_k \tag{2.30}$$

The DMD Kalman filter provides a framework for generating a reduced-order model of a system and enabling state estimation with a limited subset of measurements [66].

Chapter 3: Estimation and Control of a Planar Multibody Flexible Spacecraft

3.1 Introduction

This chapter introduces the modeling concepts used to represent the hub and flexible appendage. The flexibility of the appendage is modeled by discretizing its structure into rigid elements, referred to as panels, which are flexibly connected via damped spring-like hinges. This modeling choice most naturally represents a deployable spacecraft structure that is folded for launch and deployed in orbit. However, by varying the discretization size, as well as the spring and damping coefficients of the panel connections, the model may be adapted to represent different types of structures, such as continuous flexible structures. The accuracy of using a discretized approach with springs to model constraints and flexibility for a continuous structure is not the subject of this research, but it is explored in [1]. Initially, the appendages are restricted to bend in only one direction. If this rotation occurs about the same axis as the angular momentum of the spacecraft's orbit, the spacecraft's dynamics can be fully described within the orbital plane. This reduction in degrees of freedom simplifies the problem, enabling insight into the system's fundamental behavior through analysis. A dynamic state-space model for the hub and appendages is developed using coordinates relative to a body-frame attached to the hub.

The proposed actuation consists of a reaction wheel in the spacecraft hub and a magnetic torque rod in each of the panels, subject to constraints on allowable outputs. The state-space system is linearized, enabling the application of linear state feedback control, such as a linear-quadratic regulator (LQR). The control nonlinearities motivate the design of a nonlinear feedback controller. Structural deformations and vibrations, along with an artificial potential energy describing the attitude error, form a candidate Lyapunov function. Lyapunov analysis of the system yields a stabilizing feedback control law for the torque rods and reaction wheels. Numerical simulations demonstrate the effectiveness of this control law and the impact of using torque rods to stabilize the appendage shape. An extended Kalman filter is implemented to perform state estimation, and the control law is evaluated when using output feedback.

The contributions of this chapter are as follows: (1) a planar multibody dynamic model of a flexible spacecraft actuated by reaction wheels and magnetic torque rods including orbital motion, gravity gradient torque, and a magnetic field that varies with orbital position; (2) a state-feedback controller based on a Lyapunov design that tracks a desired attitude, suppresses oscillations in the appendages, and compares favorably to a linear control design; and (3) an estimation framework and corresponding output feedback design based on rate measurements of each spacecraft component assimilated by an Extended Kalman Filter. Numerical simulations are performed to validate the efficacy of the proposed control law, first under idealized conditions and then under more realistic conditions. State estimation and output feedback are added to the model to demonstrate the retention of performance with limited sensing and measurement noise.

The chapter is organized as follows. Section 3.2 develops the dynamics model of the spacecraft. Section 3.3 proposes the feedback control design and includes simulation results. Section 3.4 describes the estimation and output feedback control. Finally, Section 3.5 summarizes the chapter.

3.2 Planar Multibody Flexible Spacecraft Model

Consider a spacecraft that consists of a central hub with two adjoining flexible appendages. Each appendage is discretized into a set of elements, referred to as panels. Consider also an Earth-centered inertial frame $\mathcal{I} = (O, \hat{\mathrm{e}}_x, \hat{\mathrm{e}}_y, \hat{\mathrm{e}}_3)$, an Earth-centered rotating frame that rotates at the orbital rate of the spacecraft $\mathcal{P} = (O, \hat{\mathrm{e}}_r, \hat{\mathrm{e}}_\theta, \hat{\mathrm{e}}_3)$, a body-fixed frame affixed to the central hub of the spacecraft $\mathcal{A} = (C, \hat{\mathbf{a}}_1, \hat{\mathbf{a}}_2, \hat{\mathbf{a}}_3)$, and body-fixed frames affixed to each of the component panels comprising the appendages of the spacecraft $\mathcal{B}^{(i)} = (B^{(i)}, \hat{\mathbf{b}}_1^{(i)}, \hat{\mathbf{b}}_2^{(i)}, \hat{\mathbf{b}}_3^{(i)})$, $i = 1, ..., 2N$. Angle θ defines the relative orientation of $\mathcal{P}$ with respect to $\mathcal{I}$, γ is the orientation of $\mathcal{A}$ with respect to $\mathcal{I}$, and α_i is the orientation of $\mathcal{B}^{(i)}$ with respect to $\mathcal{A}$.

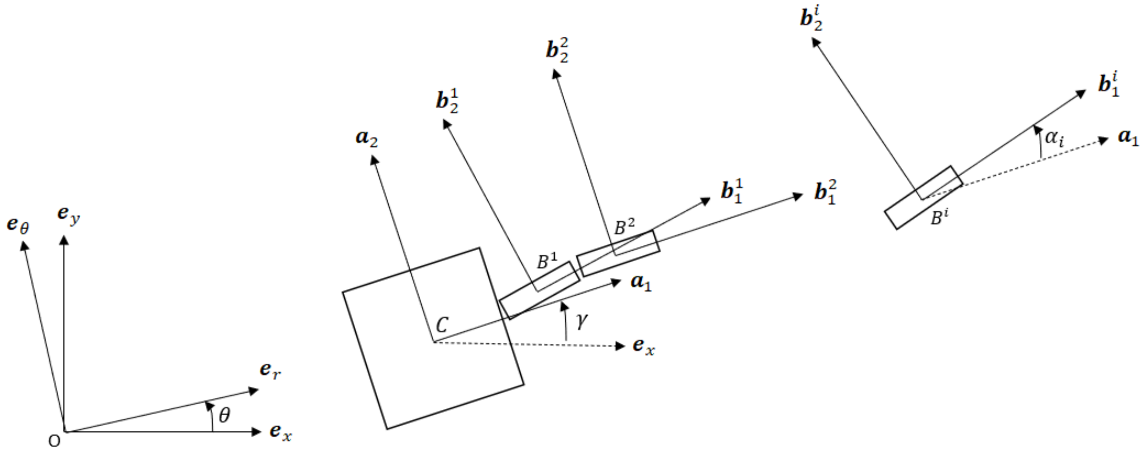

Figure 3.1: Reference frames used for the flexible spacecraft model. Frame $\boldsymbol{\mathcal{A}}$ is fixed to the hub; frames $\boldsymbol{\mathcal{B}}^{(i)}, i = 1, \ldots, 2N$, are fixed to each appendage

To model structural flexibility, the connection of the each of the panels is modeled as a damped spring-like hinge. The discretization size, as well as the stiffness and damping coefficients of the hinges, can be adjusted to simulate various types of flexible structures, such as hinged deployable structures or continuously flexible structures. See Fig. 3.2 for an illustration of the discretized approximation.

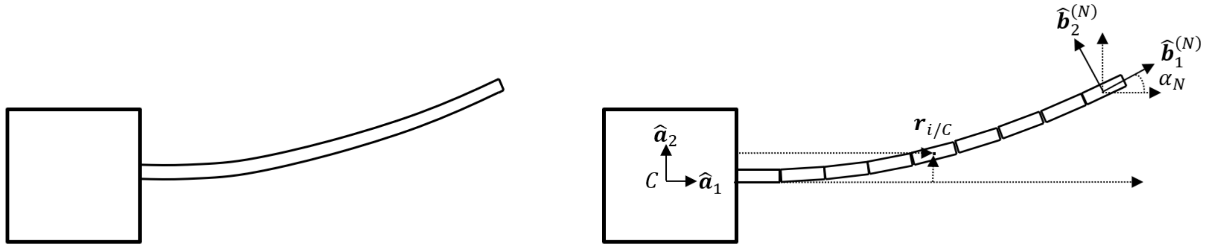

Continuous Model

Discretized Model

Figure 3.2: Discretized representation of structural flexibility

Assume that the hinged panel connections have one degree of freedom, specifically that the ith panel may only rotate about the $\hat{\mathbf{b}}_3^{(i)}$ axis. This constraint ensures that $\hat{\mathbf{b}}_3^{(i)} = \hat{\mathbf{a}}_3$ for all i. If the rotation of the hub is restricted to the $\hat{\mathbf{a}}_3$ axis, and $\hat{\mathbf{a}}_3$ is aligned with $\hat{\mathbf{e}}_h$, then all spacecraft component rotations occur about $\hat{\mathbf{e}}_h$ and all spacecraft motion is confined to the orbital plane. Consequently, it is only necessary to consider two-dimensional dynamics.

The following assumptions are made about the considered spacecraft: each panel is the same size, $L_i = L_j \ll \forall i, j \in \{1, ..., 2N\}$, the hub is significantly larger and more massive than each individual panel, $I_p \ll I_C$, the appendages do not reach very high angular rates relative to the hub, $\dot{\alpha}_i \ll 1$, the relative translational velocities of the appendages remain small, $\dot{x}_{i/C} \ll \dot{y}_{i/C}$, and the reaction wheels produce torque on the order of milli-Newton meters, $u_{\text{rw}} \ll 1$.

3.2.1 Multibody Dynamics

This section derives the dynamics of the spacecraft in the reference frame of the hub and models its internal forces, control inputs, and disturbances to yield the equations of motion for the system. To refer to each of the components of the spacecraft notationally, the indexing scheme shown in Fig. 3.3 is used.

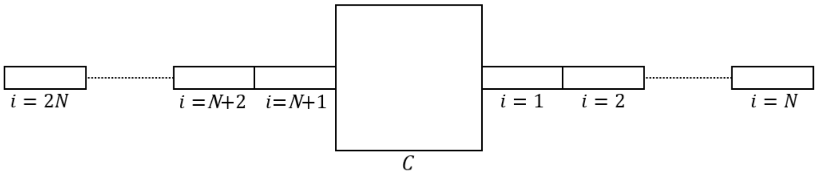

Figure 3.3: Indexing for proposed spacecraft structure consisting of a hub (C) and 2 flexibly connected appendages modeled with N panels each

First, the dynamics of the hub C and each of the panels comprising the appendages are derived. For the hub,

$$\mathbf{r}_{C/O} = x_C\hat{\mathbf{e}}_x + y_C\hat{\mathbf{e}}_y \tag{3.1}$$

$$^{\mathcal{I}}\mathbf{v}_{C/O} = \dot{x}_C\hat{\mathbf{e}}_x + \dot{y}_C\hat{\mathbf{e}}_y \tag{3.2}$$

$$^{\mathcal{I}}\mathbf{a}_{C/O} = \ddot{x}_C\hat{\mathbf{e}}_x + \ddot{y}_C\hat{\mathbf{e}}_y. \tag{3.3}$$

Consider reference frame $\mathcal{A}$. The inertial derivative of unit vector $\hat{\mathbf{a}}_1$ is $^{\mathcal{I}}\frac{d}{dt}\hat{\mathbf{a}}_i = {}^{\mathcal{I}}\boldsymbol{\omega}^A \times \hat{\mathbf{a}}_i$, where $^{\mathcal{I}}\boldsymbol{\omega}^A = \dot{\gamma}\hat{\mathbf{a}}_3$ is the angular velocity of frame A in the inertial reference frame. Using the two-dimensional orbital plane reference frame, the angular velocity of the hub is restricted to the $\hat{\mathbf{a}}_3 = \hat{\mathbf{e}}_3$ direction with magnitude $\dot{\gamma}$. For the panels,

$$\mathbf{r}_{i/O} = \mathbf{r}_{C/O} + \mathbf{r}_{i/C} = x_C\hat{\mathbf{e}}_x + y_C\hat{\mathbf{e}}_y + x_{i/C}\hat{\mathbf{a}}_1 + y_{i/C}\hat{\mathbf{a}}_2. \tag{3.4}$$

Differentiating with respect to time yields

$$ {}^{\mathcal{I}}\mathbf{v}_{i/O} = {}^{\mathcal{I}}\frac{d}{dt}\mathbf{r}_{i/O} = \dot{x}_C\hat{\mathbf{e}}_x + \dot{y}_C\hat{\mathbf{e}}_y + \dot{x}_{i/C}\hat{\mathbf{a}}_1 + \dot{y}_{i/C}\hat{\mathbf{a}}_2 + x_{i/C}(\dot{\gamma}\hat{\mathbf{e}}_3 \times \hat{\mathbf{a}}_1) + y_{i/C}(\dot{\gamma}\hat{\mathbf{e}}_3 \times \hat{\mathbf{a}}_2) \tag{3.5} $$

$$ = \dot{x}_C\hat{\mathbf{e}}_x + \dot{y}_C\hat{\mathbf{e}}_y + \dot{x}_{i/C}\hat{\mathbf{a}}_1 + \dot{y}_{i/C}\hat{\mathbf{a}}_2 + \dot{\gamma}x_{i/C}\hat{\mathbf{a}}_2 - \dot{\gamma}y_{i/C}\hat{\mathbf{a}}_1. \tag{3.6} $$

Differentiating again yields the inertial acceleration, i.e.,

$$ {}^{\mathcal{I}}\mathbf{a}_{i/O} = \ddot{x}_C\hat{\mathbf{e}}_x + \ddot{y}_C\hat{\mathbf{e}}_y + \ddot{x}_{i/C}\hat{\mathbf{a}}_1 + \ddot{y}_{i/C}\hat{\mathbf{a}}_2 + \ddot{\gamma}x_{i/C}\hat{\mathbf{a}}_2 - \ddot{\gamma}y_i\hat{\mathbf{a}}_1 + 2\dot{\gamma}\dot{x}_{i/C}\hat{\mathbf{a}}_2 - 2\dot{\gamma}\dot{y}_{i/C}\hat{\mathbf{a}}_1 - \dot{\gamma}^2x_{i/C}\hat{\mathbf{a}}_1 - \dot{\gamma}^2y_{i/C}\hat{\mathbf{a}}_2. \tag{3.7} $$

Euler's first law is applied to the hub and to each panel. It is convenient to express the forces on the hub in reference frame $\mathcal{A}$. The total force on the hub is $\mathbf{F}_C = X_C\hat{\mathbf{a}}_1 + Y_C\hat{\mathbf{a}}_2$, which implies

$$ \ddot{x}_C\hat{\mathbf{a}}_1 + \ddot{y}_C\hat{\mathbf{a}}_2 = \frac{X_C}{m_C}\hat{\mathbf{a}}_1 + \frac{Y_C}{m_C}\hat{\mathbf{a}}_2. \tag{3.8} $$

The sum of the forces on each panel is $\mathbf{F}_i = X_i\hat{\mathbf{a}}_1 + Y_i\hat{\mathbf{a}}_2$. Applying Euler's first law to the ith appendage yields

$$ {}^{\mathcal{I}}\mathbf{a}_{i/O} = \frac{X_i}{m_i}\hat{\mathbf{a}}_1 + \frac{Y_i}{m_i}\hat{\mathbf{a}}_2 \tag{3.9} $$

To control the shape of the entire spacecraft and maintain its alignment with the hub, it is convenient to analyze the dynamics of each panel relative to the hub. The resulting control problem is to drive the relative angle, as well as the relative translational and angular velocities, to zero. To express the equations of motion in the hub's reference frame, the kinematics for the panel and hub are substituted into Eq. (3.7) and the expression is rearranged to solve for the acceleration of the panels relative to the hub, i.e.,

$$\begin{aligned}\ddot{x}_{i/C}\hat{\mathbf{a}}_1+\ddot{y}_{i/C}\hat{\mathbf{a}}_2 = & \frac{X_i}{m_i}\hat{\mathbf{a}}_1+\frac{Y_i}{m_i}\hat{\mathbf{a}}_2-\frac{X_C}{m_C}\hat{\mathbf{a}}_1-\frac{Y_C}{m_C}\hat{\mathbf{a}}_2-\ddot{\gamma}x_{i/C}\hat{\mathbf{a}}_2+\ddot{\gamma}y_i\hat{\mathbf{a}}_1 \\ & -2\dot{\gamma}\dot{x}_{i/C}\hat{\mathbf{a}}_2+2\dot{\gamma}\dot{y_{i/C}}\hat{\mathbf{a}}_1+\dot{\gamma}^2x_{i/C}\hat{\mathbf{a}}_1+\dot{\gamma}^2y_{i/C}\hat{\mathbf{a}}_2.\end{aligned} \tag{3.10}$$

The terms are collected to arrive at the following scalar differential equations:

$$\ddot{x}_{i/C}=\frac{X_i}{m_i}-\frac{X_C}{m_C}+\ddot{\gamma}y_{i/C}+2\dot{\gamma}\dot{y}_{i/C}+\dot{\gamma}^2x_{i/C} \tag{3.11}$$

$$\ddot{y}_{i/C}=\frac{Y_i}{m_i}-\frac{Y_C}{m_C}-\ddot{\gamma}x_{i/C}-2\dot{\gamma}\dot{x}_{i/C}+\dot{\gamma}^2y_{i/C}. \tag{3.12}$$

Next, Euler's second law is applied to the hub and panels, with the total internal moments on each defined as M_C and M_i, respectively, i.e.,

$$\frac{d}{dt}{}^{\mathcal{I}}\mathbf{h}_C=\frac{d}{dt}I_C\dot{\gamma}\hat{\mathbf{a}}_3=I_C\ddot{\gamma}\hat{\mathbf{a}}_3=M_C\hat{\mathbf{a}}_3 \tag{3.13}$$

$$\frac{d}{dt}{}^{\mathcal{I}}\mathbf{h}_i=\frac{d}{dt}I_p(\dot{\gamma}+\dot{\alpha}_i)\hat{\mathbf{a}}_3=I_p(\ddot{\gamma}+\ddot{\alpha}_i)\hat{\mathbf{a}}_3=M_i\hat{\mathbf{a}}_3. \tag{3.14}$$

The state for each panel described in two dimensions is

$$\xi_i=\begin{bmatrix}x_{i/C} & y_{i/C} & \alpha_{i/C} & \dot{x}_{i/C} & \dot{y}_{i/C} & \dot{\alpha}_{i/C}\end{bmatrix}^T. \tag{3.15}$$

The modeling of the forces and moments acting on each component, i.e., X_C, Y_C, M_C, X_i, Y_i, and M_i, are defined next.

3.2.2 Internal Force Model

Assume that the panels are connected to each other and to the hub with damped spring-like hinges. The attachment force of each hinge is modeled as a spring with spring coefficient k_s and damping coefficient c_s. The attachment moment is modeled as a torsion spring that is linearly proportional to the relative angle between the components that it connects, with spring coefficient k_t and damping coefficient c_t. With the spring modeling, the relative force between two components can be computed by determining the relative position and velocity of adjoining edges. The relative position and velocity of adjoining edges of the ith panel to its adjacent panel for $i = 1, ..., N$ are expressed as

$$\mathbf{r}_{i/i+1} = \mathbf{r}_{i/C} + \frac{L_i}{2}\hat{\mathbf{b}}_1^{(i)} - \mathbf{r}_{(i+1)/C} + \frac{L_{i+1}}{2}\hat{\mathbf{b}}_1^{(i+1)} \tag{3.16}$$

$$^{\mathcal{A}}\mathbf{v}_{i,=/i+1} =^{\mathcal{A}} \mathbf{v}_{i/C} + \frac{L_i}{2}\frac{^{\mathcal{A}}d}{dt}\hat{\mathbf{b}}_1^{(i)} -^{\mathcal{A}} \mathbf{v}_{(i+1)/C} + \frac{L_{i+1}}{2}\frac{^{\mathcal{A}}d}{dt}\hat{\mathbf{b}}_1^{(i+1)} \tag{3.17}$$

$$\mathbf{r}_{i,=/i-1} = \mathbf{r}_{i/C} - \frac{L_i}{2}\hat{\mathbf{b}}_1^{(i)} - \mathbf{r}_{(i-1)/C} - \frac{L_{i-1}}{2}\hat{\mathbf{b}}_1^{(i-1)} \tag{3.18}$$

$$^{\mathcal{A}}\mathbf{v}_{i/i-1} =^{\mathcal{A}} \mathbf{v}_{i/C} - \frac{L_i}{2}\frac{^{\mathcal{A}}d}{dt}\hat{\mathbf{b}}_1^{(i)} -^{\mathcal{A}} \mathbf{v}_{(i-1)/C} - \frac{L_{i-1}}{2}\frac{^{\mathcal{A}}d}{dt}\hat{\mathbf{b}}_1^{(i-1)}. \tag{3.19}$$

For $i = N+1, ..., 2N$ the negation of the shown position and velocity is used due to the indexing scheme increasing in the opposite direction on the other side of the spacecraft. The resulting internal force on an appendage from an adjacent appendage is

$$\mathbf{F}_{i,j} = -k_s\mathbf{r}_{i/j} - c_s^{\mathcal{A}}\mathbf{v}_{i/j}. \tag{3.20}$$

The torque resulting from the internal forces is

$$\mathbf{T}_{i/i+1} = \frac{L_i}{2}\hat{\mathbf{b}}_1^{(i)} \times \mathbf{F}_{i/i+1}, \quad \mathbf{T}_{i/i-1} = -\frac{L_i}{2}\hat{\mathbf{b}}_1^{(i)} \times \mathbf{F}_{i/i-1}. \tag{3.21}$$

The internal moment resulting from the spring hinge is modeled as

$$\mathbf{M}_{i/i+1} = -k_t(\alpha_i - \alpha_{i+1}) - c_t(\dot{\alpha}_i - \dot{\alpha}_{i-1}), \quad \mathbf{M}_{i/i-1} = k_t(\alpha_i - \alpha_{i-1}) - c_t(\dot{\alpha}_i - \dot{\alpha}_{i-1}). \tag{3.22}$$

The forces and moments for the end appendages and for the hub are included in Appendix A.1. These equations provide a complete description of the internal forces and moments acting on the modeled spacecraft. The unforced dynamics of the spacecraft can then be described as a state-space system. Due to the primary investigation being attitude and shape control, the translational dynamics of the appendages are expressed in the reference frame of the hub, and the translational dynamics of the hub are excluded from the analysis. Therefore, the total state of the system $\boldsymbol{\eta}$ representing the attitude and shape of the spacecraft is defined as

$$\boldsymbol{\eta} = \begin{bmatrix}\gamma & \dot{\gamma} & \xi_1^T & \xi_2^T & \dots & \xi_N^T & \xi_{N+1}^T & \dots & \xi_{2N}^T\end{bmatrix}^T, \tag{3.23}$$

and the unforced dynamics are

$$\dot{\boldsymbol{\eta}} = \boldsymbol{f}(\boldsymbol{\eta}). \tag{3.24}$$

For convenience, the portion of the state for the hub orientation γ and rate $\dot{\gamma}$ is denoted $\boldsymbol{\eta}_C$ and the remainder of the state vector describing the appendages is denoted $\boldsymbol{\eta}_p$, i.e., $\boldsymbol{\eta} = [\boldsymbol{\eta}_C \; \boldsymbol{\eta}_p]^T$.

3.2.3 Control Input Model

Assume that there is a reaction wheel in the hub and that each of the panels are equipped with a torque rod. Assume also that the reaction wheel has some saturation limit K_{rw} and that the control input is simply the reaction wheel torque, so that the torque generated by the reaction wheel in response to control input u_{rw} is

$$\tau_{\text{rw}} = \text{sat}(u_{\text{rw}}) = \begin{cases} -K_{\text{rw}}, & u_{\text{rw}} \leq -K_{\text{rw}} \\ u_{\text{rw}}, & -K_{\text{rw}} < u_{\text{rw}} < K_{\text{rw}} \\ K_{\text{rw}}, & u_{\text{rw}} \geq K_{\text{rw}}. \end{cases}$$

Assume each torque rod is aligned with the $\mathbf{b}_1^{(i)}$ axis of the body frame assigned to the respective spacecraft segment. Torque rods typically operate by turning on and off electrical current through a coil, resulting in a discrete set of control inputs. Assume that the control input for the ith torque rod $u_i$is modeled as the desired dipole generated by the torque rod, and the maximum possible magnitude of the dipole is denoted K_{tr}. Using the sign function to implement the discrete control input set can lead to chattering around $u_i = 0$; the deadband function is used instead. The possible dipoles generated by each torque rod are as follows:

$$m_i = K_{\text{tr}}\text{dbd}(u_i, \lambda) = \begin{cases} -K_{\text{tr}} & u_i < -\lambda \\ 0 & -\lambda < u_i < \lambda \\ K_{\text{tr}} & u_i > \lambda \end{cases}$$

To ensure that the torque developed by a magnetic torque rod is confined to the $\hat{\mathbf{e}}_3$ direction, only polar orbits are considered. The magnetic dipole resulting from the torque rod expressed in an Earth-centered polar frame is

$$\mathbf{m}_i = \begin{bmatrix} m_i \cos\psi_i \\ m_i \sin\psi_i \\ 0 \end{bmatrix}, \tag{3.25}$$

where ψ is defined as the angle between the spacecraft's colatitude θ and the body frame axis $\hat{\mathbf{b}}_2^{(i)}$, i.e., $\psi_i = \theta - \gamma - \alpha_i$, for the appendages. The Earth's magnetic field is modeled as a dipole, and in the fixed reference frame of the orbital plane, can be expressed as

$$\mathbf{B} = \begin{bmatrix} 2H_e \left(\frac{R}{\rho}\right)^3 \cos\theta \\ H_e \left(\frac{R}{\rho}\right)^3 \sin\theta \\ 0 \end{bmatrix}. \tag{3.26}$$

The torque developed by this control input can then be computed by taking the cross-product of the resulting torque rod dipole 3.25 and the Earth's magnetic field 3.26, i.e.,

$$\boldsymbol{\tau}_{\text{tr}} = 2H_e \left(\frac{R}{\rho}\right)^3 K_{\text{tr}}\text{dbd}(u_i, \lambda)(\sin\psi_i \sin\theta - 2\cos\psi_i \cos\theta)\hat{\mathbf{e}}_3. \tag{3.27}$$

Defining the input vector as

$$\boldsymbol{u} = \begin{bmatrix} u_1 & u_2 & \dots & u_{2N}, u_{\text{rw}} \end{bmatrix}^T, \tag{3.28}$$

the forced dynamics can then be written as

$$\dot{\boldsymbol{\eta}} = \boldsymbol{f}(\boldsymbol{\eta}, \boldsymbol{u}). \tag{3.29}$$

3.2.4 Gravity Gradient Effects

When considering large spacecraft, a significant disturbance moment comes from the gravity gradient effect, which results from each part of the spacecraft experiencing a slightly different magnitude of gravitational force from Earth. The generalized first-order approximation of gravity gradient torque is [68]

$$\boldsymbol{\tau}_G = \frac{3\mu}{\rho^5}\boldsymbol{\rho} \times \mathbb{I}\boldsymbol{\rho}, \tag{3.30}$$

where $\boldsymbol{\rho} = \rho\hat{\mathbf{e}}_r$ is the vector from the center of the Earth to the center of mass of the body and $\mathbb{I}$ is its moment of inertia tensor. In the body frames of the hub and panels, respectively,

$$\boldsymbol{\rho}_C = \rho_C \cos{(\theta - \gamma)}\hat{\mathbf{a}}_1 - \rho_C \sin{(\theta - \gamma)}\hat{\mathbf{a}}_2, \quad \boldsymbol{\rho}_i = \rho_i \cos{\psi_i}\hat{\mathbf{b}}_1^{(i)} - \rho_i \sin{\psi_i}\hat{\mathbf{b}}_2^{(i)} \tag{3.31}$$

I approximate the moment of inertia tensor of the hub as a cube of side-length s and the panels as thin rods of length L. The moment of inertia tensors are

$$\mathbb{I}_C = \begin{bmatrix} I_c & 0 & 0 \\ 0 & I_c & 0 \\ 0 & 0 & I_c \end{bmatrix} \tag{3.32}$$

$$\mathbb{I}_i = \begin{bmatrix} I_p & 0 & 0 \\ 0 & 0 & 0 \\ 0 & 0 & I_p \end{bmatrix} \tag{3.33}$$

where $I_c = \frac{1}{6}s^2$ and $I_p = \frac{1}{12}L_i^2$. The first-order approximation for gravity gradient torque for the hub is therefore zero and, for the panels,

$$\boldsymbol{\tau}_G = -\frac{\mu m_i L_i^2}{8\rho_i^3}\sin(2\psi)\hat{\mathbf{a}}_3. \tag{3.34}$$

The gravity gradient effect is applied as a disturbance in numerical simulations to evaluate control robustness.

3.3 State Feedback Control

This section considers reference tracking of a nadir-pointing attitude trajectory in a low altitude polar orbit (see Appendix C.1 for orbital parameters). The proposed controller tracks the desired trajectory while maintaining spacecraft flatness.

3.3.1 Linear Feedback Control

The equilibrium of the system Eq. (3.24) is when each appendage is flat and unmoving relative to the hub reference frame. The dynamics of the undisturbed system are linearized by taking the Jacobian of the dynamics at the equilibrium condition. The orientation of the reference frame γ does not appear in the Jacobian of the unforced state dynamics. This indicates that the unforced dynamics of the system are invariant with respect to the orientation of the hub, which arises from using the reference frame of the hub to express the appendage dynamics. For the panels, the equilibrium for $x_{i/C}$ is $x_{\text{eq}}^{(i)} = \pm(\frac{s}{2} + \frac{2i-1}{2}L)$; it is positive for $i = 1, ..., N$ and negative for $i = N+1, ..., 2N$. Thus the equilibrium state of each appendage is $\xi_{\text{eq}}^{(i)} = \pm \begin{bmatrix} x_{\text{eq}}^{(i)} & 0 & 0 & 0 & 0 & 0 \end{bmatrix}^T$. Because the dynamics of each component of the satellite are explicitly dependent on only the states of the adjacent components and the hub, the linearized unforced dynamics from Eq. (3.24) can be written in block matrix form, where the blocks are defined as

$$A_C = \frac{\partial \dot{\boldsymbol{\eta}}_C}{\partial \boldsymbol{\eta}}, \quad A_C^{(i)} = \frac{\partial \dot{\boldsymbol{\xi}}_i}{\partial \boldsymbol{\eta}_C}, \quad A_i = \frac{\partial \dot{\boldsymbol{\xi}}_i}{\partial \boldsymbol{\eta}_p}. \tag{3.35}$$

The overall system Jacobian is

$$A = \frac{\partial \mathbf{f}}{\partial \boldsymbol{\eta}} = \begin{bmatrix} A_C & 0 & \dots & \dots & 0 \\ A_C^{(1)} & A_1 & 0 & \dots & 0 \\ A_C^{(2)} & 0 & A_2 & \dots & 0 \\ \vdots & \vdots & \vdots & \ddots & \vdots \\ A_C^{(2N)} & 0 & 0 & \dots & A_{2N} \end{bmatrix}. \tag{3.36}$$

To evaluate the stability of the unforced spacecraft structure, the eigenvalues of A are computed. By inspection, for any number of appendages, A has two eigenvalues with zero real part and the rest have a negative real part. The two imaginary axis eigenvalues correspond to the orientation and angular velocity of the hub, because in the unforced case there is no external damping of the hub's angular motion. Thus, the unforced dynamics of the appendages near the equilibrium point are stable due to the damping of the hinges, but the unforced dynamics of the hub are not.

The input-to-state linearization of the dynamics Eq. (3.29) can also be described in block matrix form by taking

$$B_C = \frac{\partial \dot{\boldsymbol{\eta}}_C}{\partial \mathbf{u}} = \begin{bmatrix} 0 & \dots & 0 \\ \\ 0 & \dots & \frac{1}{I_C} \end{bmatrix} \tag{3.37}$$

$$B_i = \frac{\partial \dot{\boldsymbol{\xi}}_i}{\partial \mathbf{u}} = \begin{bmatrix} 0^{4\times 1} & \dots & \dots & \dots & \dots & \dots & \dots & 0^{4\times 1} \\ 0 & \dots & \dots & \dots & \dots & \dots & 0 & -\frac{x_{\text{eq}}^{(i)}}{I_C} \\ 0 & \dots & 0 & \frac{E}{I_p} & 0 & \dots & 0 & -\frac{1}{I_C} \end{bmatrix}, \tag{3.38}$$

where $E = 2H_e(\frac{R}{\rho})^3$ and $\frac{E}{I_p}$ appears in the ith column of B_i. The total matrix is

$$B = \frac{\partial \boldsymbol{\eta}}{\partial \mathbf{u}} = \begin{bmatrix} B_C^T & B_1^T & B_2^T & \dots & B_{2N}^T \end{bmatrix}^T. \tag{3.39}$$

and the portion of the matrix dealing with the torque rods is

$$B_p = \begin{bmatrix} B_1^T & B_2^T & \dots & B_{2N}^T \end{bmatrix}^T \tag{3.40}$$

The closed-loop linearized dynamics are

$$\dot{\boldsymbol{\eta}} = A\boldsymbol{\eta} + B\boldsymbol{u}. \tag{3.41}$$

From the closed-loop linear dynamics a linear-quadratic regulator (LQR) generates a gain matrix such that the state feedback control law $\boldsymbol{u} = -K\boldsymbol{\eta}$ is an optimal controller that exponentially stabilizes the origin. LQR serves as a baseline controller for the nonlinear system Eq. (3.29), because it is optimal, can be tuned to exhibit desired performance characteristics, and is computationally inexpensive. However, because the actuators are modeled with physical operation characteristics in mind, additional nonlinearities are introduced into the system. Specifically, the saturation nonlinearities and discrete control inputs from Section 3.2.3 are applied to the output of the LQR controller before it is applied to the system. The addition of these nonlinearities undermines the optimality and performance of the LQR and motivates the Lyapunov-based control design described next.

3.3.2 Nonlinear Feedback Control

An energy-like function that describes the kinetic and potential energy of the spacecraft appendages in the reference frame of the hub is

$$T(\boldsymbol{\eta}_p) = \frac{1}{2}\sum_{i=1}^{2N}\left[m_i(\dot{x}_{i/C}^2 + \dot{y}_{i/C}^2) + I_i\dot{\alpha}_i^2 + (k_s(x_{i/j}^2 + y_{i/j}^2) + k_t\alpha_{i/j}^2)\right], \tag{3.42}$$

where the subscript i/j denotes the position or angle of appendage i relative to appendage j; $j = i - 1$ for $i \notin \{1, N+1\}$ and $j = C$ for $i \in \{1, N+1\}$.

Assume the spacecraft is intended to be nadir-pointing. Then the desired attitude for the spacecraft hub is such that frame $\mathcal{A}$ aligns with frame $\mathcal{P}$ and the desired angular velocity of the hub is the angular rate ω_O of the orbit. An artificial potential energy minimized by the hub's desired attitude and angular velocity is

$$U(\boldsymbol{\eta}_C) = \frac{1}{2}k_p(\gamma - \theta)^2 + \frac{1}{2}I_p(\dot{\gamma} - \omega_O)^2. \tag{3.43}$$

A candidate Lyapunov function is the summation of Eqs. (3.42) and (3.43), i.e.,

$$V(\boldsymbol{\eta}) = T(\boldsymbol{\eta}_p) + U(\boldsymbol{\eta}_C). \tag{3.44}$$

Consider a diagonal matrix describing the spring, mass, and inertia properties of the system, i.e.,

$$M = \text{diag}[M_c, M_p], \tag{3.45}$$

where

$$M_c = \text{diag}[k_p, I_c],$$

$$M_p = \text{diag}[M_1, ..., M_{2N}],$$

with

$$M_i = \text{diag}[k_{s,i}, k_{s,i}, k_{t,i}, m_i, m_i, I_i].$$

Consider also a matrix that captures the relative position and angle of adjacent appendages, i.e.,

$$\mathcal{L} = \text{diag}(\mathcal{L}_c, \mathcal{L}_p) \tag{3.46}$$

where $\mathcal{L}_c$ corresponds to the the hub and $\mathcal{L}_p$ corresponds to the appendages, i.e.,

$$\mathcal{L}_p = \text{diag}(\mathcal{L}_1, ..., \mathcal{L}_N, \mathcal{L}_{N+1}, ..., \mathcal{L}_{2N}). \tag{3.47}$$

The matrix blocks are

$$\mathcal{L}_c = \mathcal{I}_2 \tag{3.48}$$

$$\mathcal{L}_i = \begin{cases} \mathcal{I}_6 & i \in \{1, N+1\} \\ \\ \text{diag}[-1, -1, -1, 0, 0, 0, \mathcal{I}_6] & i \notin \{i, N+1\} \end{cases} \tag{3.49}$$

Let $\boldsymbol{\eta}_{C,d} = [\gamma - \gamma_d \quad \omega - \omega_d]^T$ denote the orientation and angular velocity of the hub relative to the desired values. The state vector including these desired values is $\boldsymbol{\eta}_d = [\boldsymbol{\eta}_{C,d} \quad \boldsymbol{\eta}_p]^T$ The vector of relative states is computed using $\mathcal{L}$, i.e.,

$$\boldsymbol{\eta}_{rel} = \mathcal{L}\boldsymbol{\eta}_d \tag{3.50}$$

The Lyapunov function candidate Eq. (3.44) in matrix form is

$$V(\boldsymbol{\eta}_{rel}) = \frac{1}{2}\boldsymbol{\eta}_{rel}^T M \boldsymbol{\eta}_{rel}. \tag{3.51}$$

The following lemma enables analysis of the Lyapunov candidate function derivative using the linearized dynamics of the system.

Lemma 1: Let $\dot{\boldsymbol{x}} = \boldsymbol{f}(\boldsymbol{x}, \boldsymbol{u})$ be a nonlinear system with $\boldsymbol{x} = 0$ as its equilibrium point. Let $A = \frac{\partial \boldsymbol{f}}{\partial \boldsymbol{x}}$ and $B = \frac{\partial \boldsymbol{f}}{\partial \boldsymbol{u}}$ be the linearization of $\boldsymbol{f}$ about its equilibrium point with $\boldsymbol{u} = 0$. Consider a control input $\boldsymbol{u} = \boldsymbol{g}(\boldsymbol{x})$ that contains no constant terms so that the closed-loop linear system becomes

$$\dot{\boldsymbol{x}} = A\boldsymbol{x} + B\boldsymbol{g}(\boldsymbol{x}). \tag{3.52}$$

If the quadratic potential $V(\boldsymbol{x})$ satisfies $\dot{V}(\boldsymbol{x}) < -c\|\boldsymbol{x}\|^2 < 0$ along solutions of the closed loop linear system Eq. (3.52), then $V(\boldsymbol{x})$ is a Lyapunov function for the original nonlinear system. See Appendix B.3 for the proof of this lemma.

Differentiating the candidate Lyapunov function Eq. (3.51) with respect to time yields

$$\dot{V}(\boldsymbol{\eta}_{rel}, \dot{\boldsymbol{\eta}}_{rel}) = \boldsymbol{\eta}_{rel}^T M \dot{\boldsymbol{\eta}}_{rel}. \tag{3.53}$$

The linearized dynamics $\dot{\boldsymbol{\eta}}_{rel} = A\boldsymbol{\eta}_{rel} + B\boldsymbol{u}$ are substituted into $\dot{V}$ to yield

$$\dot{V}(\boldsymbol{\eta}_{rel}, \dot{\boldsymbol{\eta}}_{rel}) = \boldsymbol{\eta}_{rel}^T AM\boldsymbol{\eta}_{rel} + \boldsymbol{\eta}_{rel}^T MB\boldsymbol{u}. \tag{3.54}$$

For convenience of analyzing the Lyapunov function derivative, the output is collected into two terms relating to the energy of the hub $\dot{V}_C$, and the appendages $\dot{V}_p$, such that $\dot{V} = \dot{V}_C + \dot{V}_p$. The splitting is carried out as follows

$$\dot{V} = \left[\begin{array}{c} (\mathcal{L}_c\boldsymbol{\eta}_{c,d})^T \\ \hline (\mathcal{L}_p\boldsymbol{\eta}_p)^T \end{array}\right] \left[\begin{array}{c} MA_C \\ \hline MA_p \end{array}\right] \left[\begin{array}{c} \boldsymbol{\eta}_{rel} \\ \hline \boldsymbol{\eta}_{rel} \end{array}\right] + \left[\begin{array}{c} (\mathcal{L}_c\boldsymbol{\eta}_{c,d})^T \\ \hline (\mathcal{L}_p\boldsymbol{\eta}_p)^T \end{array}\right] \left[\begin{array}{c} B_C \\ \hline B_p \end{array}\right] \left[\begin{array}{c} u_{rw} \\ \hline u_1 \\ \vdots \\ u_{2N} \end{array}\right] = \left[\begin{array}{c} \dot{V}_C \\ \hline \dot{V}_p \end{array}\right], \tag{3.55}$$

where A_C and B_C are the first two rows of the the Jacobian matrix A, and A_p and B_p consist of the remaining rows of matrices A and B.

The expression for V_p can be expanded as

$$\dot{V}_p = \boldsymbol{\eta}_{rel,p}^T M A_p \boldsymbol{\eta}_{rel} + \boldsymbol{\eta}_{rel,p}^T M B_p \mathbf{u}_i. \tag{3.56}$$

The first term in the expression may be equivalently expressed as $\boldsymbol{\eta}_{rel,p}^T M A_p \boldsymbol{\eta}_{rel,p}$, where A_p excludes the first two columns of A to make it a square matrix. This truncation does not change the value of $\dot{V}_p$ because the state variables of the appendages are expressed in the hub's reference frame and thus do not depend on the state of the hub. With the exclusion of the dynamics of the hub, the two zero eigenvalues are also excluded, thus A_p is Hurwitz. Because M is positive definite, the product MA_p is also Hurwitz. Consequently,

$$\boldsymbol{\eta}_{rel,p}^T M A_p \boldsymbol{\eta}_{rel,p} < 0. \tag{3.57}$$

Assuming that the spacecraft is near the equilibrium, then the translational velocities of each appendage relative to the hub are small. The expansion of the second term is

$$\boldsymbol{\eta}_{rel,p}^T B_p \mathbf{u}_i = E \sum_{i=1}^{2N} \dot{\alpha}_i u_i \tag{3.58}$$

This expression suggests that a control law for each torque rod of

$$u_i = -\mathrm{dbd}(\dot{\alpha}_i) K_{tr} \tag{3.59}$$

guarantees that $\boldsymbol{\eta}_p^T M B_p \mathbf{u}_i \leq 0$ for all i and minimizes $\dot{V}_p$ subject to the the control constraints of the torque rods. Under the proposed control law, $\dot{V}_p < 0$.

V_C is now considered. Expanding the expression

$$\dot{V}_C = \boldsymbol{\eta}_{rel,C}^T M A_C \boldsymbol{\eta} + \boldsymbol{\eta}_{rel,C}^T M B_C u_{rw}, \tag{3.60}$$

yields

$$\dot{V}_C = (\dot{\gamma} - \omega_O)(k_p(\gamma - \theta) + \beta_C(\dot{\alpha}_1 + \dot{\alpha}_{N+1}) + \beta_k(\alpha_1 + \alpha_{N+1}) + u_{rw}) - u_{rw}\frac{I_p}{I_C}\sum_{i=1}^{2N}\dot{\alpha}_i, \tag{3.61}$$

where constants β_C and β_k are defined as

$$\beta_k = k_t - \frac{Lk_s s}{4} \tag{3.62}$$

$$\beta_C = c_t - \frac{Lc_s s}{4} \tag{3.63}$$

The following control law is proposed:

$$u_{rw} = -\beta_C(\dot{\alpha}_1 + \dot{\alpha}_{N+1}) - \beta_k(\alpha_1 + \alpha_{N+1}) - k_p(\gamma - \theta) - k_L(\dot{\gamma} - \omega_O). \tag{3.64}$$

Substituting the proposed control law into $\dot{V}_C$ yields

$$\dot{V}_C = -k_L(\dot{\gamma} - \omega_O)^2, \tag{3.65}$$

which implies $\dot{V}_C \leq 0$ under the proposed control law Eq. (3.64). This expression can also be written as

$$\dot{V}_C = \boldsymbol{\eta}_{c,d}^T P \boldsymbol{\eta}_{c,d}, \tag{3.66}$$

where

$$P = \begin{bmatrix} 0 & kp \\ -kp & -k_L \end{bmatrix} \tag{3.67}$$

Combining $\dot{V}_C$ and $\dot{V}_p$ resulting from the proposed control laws yields

$$\dot{V}(\boldsymbol{\eta}_{rel}, \dot{\boldsymbol{\eta}}_{rel}) = \boldsymbol{\eta}_{rel,p}^T M A_p \boldsymbol{\eta}_{rel,p} - EK_{tr}\sum_{i=1}^{2N}\dot{\alpha}_i \mathrm{dbd}(\dot{\alpha}_i) - k_L(\dot{\gamma} - \omega_O)^2. \tag{3.68}$$

Note that

$$\dot{V}(\boldsymbol{\eta}_{rel}, \dot{\boldsymbol{\eta}}_{rel}) \leq \boldsymbol{\eta}_{rel,p}^T M A_i \boldsymbol{\eta}_{rel,p} + \boldsymbol{\eta}_{c,d}^T P \boldsymbol{\eta}_{c,d} = \begin{bmatrix}\boldsymbol{\eta}_{c,d} & \boldsymbol{\eta}_{rel,p}\end{bmatrix}^T \begin{bmatrix} P & 0 \\ 0 & MA_i \end{bmatrix} \begin{bmatrix}\boldsymbol{\eta}_{c,d} & \boldsymbol{\eta}_{rel,p}\end{bmatrix}, \tag{3.69}$$

where the last term can be rewritten as

$$\boldsymbol{\eta}_{rel}^T \Pi \boldsymbol{\eta}_{rel}, \tag{3.70}$$

with

$$\Pi = \begin{bmatrix} P & 0 \\ 0 & MA_i \end{bmatrix}. \tag{3.71}$$

Therefore,

$$\dot{V}(\boldsymbol{\eta}_{rel}, \dot{\boldsymbol{\eta}}_{rel}) \leq \boldsymbol{\eta}_{rel}^T \Pi \boldsymbol{\eta}_{rel} \leq -c\|\boldsymbol{\eta}_{rel}\|^2 \leq \boldsymbol{\eta}_{rel,p}^T MA_p \boldsymbol{\eta}_{rel,p} < 0. \tag{3.72}$$

along solutions of the closed-loop linear system Eq. (3.41). According to Lemma 1, the proposed control law asymptotically stabilizes the origin of the nonlinear system Eq. (3.29).

From a practical standpoint, the control law resulting from Lyapunov analysis is favorable for implementation. The torque rod control law acts in the opposite direction of the angular velocity of the appendage relative to the hub. It is also computationally simple and easily implementable using angular velocity measured with gyros. The control law for the reaction wheel contains proportional and derivative control terms with tuneable gains and also terms that become relevant if the appendages directly affixed to the hub are not flat.

3.3.3 Simulation Results

Numerical simulations illustrate the performance of the closed-loop system. The simulations conducted involve an initial value problem where the system starts with an initial condition set some distance from the nadir reference. The controller then actuates the spacecraft to track the reference, and the response is observed. This scenario simulates a real-world situation where a spacecraft maneuvers to a different pointing target, such as transitioning from sun alignment to nadir alignment. To better understand controller behavior and performance, several controllers are simulated and compared. In addition to the proposed Lyapunov-based controller, an LQR controller is implemented. To demonstrate the performance loss resulting from the application of the saturation and deadband functions described in Section 3.2.3 to the control signal, the performance of the LQR controller with and without these nonlinearities is compared. The LQR controller is tuned to keep the control effort near the saturaton limits. Additionally, to better understand the effect of the torque rods on system performance, the Lyapunov-based controller without the β_k, β_c terms, and without the torque rod inputs was also tested; this leaves a proportional-derivative controller for the reaction wheel.

Idealized Model

The first simulation assumes an idealized scenario where there are no disturbance forces or moments. Assume that the torque generated by the torque rods is not subject to varying magnitudes due to the time-varying angles of incidence with the magnetic field lines of the Earth and, instead, that the maximum control authority is available to the torque rods at all times, i.e., $\tau_{\text{tr}} = 2H_e(\frac{R}{\rho})^3 u_i$. The control objective is to track a reference pointing angle $\theta(t) = \omega_0 t + \theta_0$, where θ_0 is the latitude of the spacecraft at $t = 0$, and an angular velocity of ω_0. This reference corresponds to a constantly nadir-pointing attitude. The simulation is an initial value problem such that the controller drives the spacecraft from some initial value problem to the reference trajectory. The initial state of the spacecraft hub is shown in Table C.1, and the appendages are initially at equilibrium (flat and unmoving relative to the hub). The physical parameters for the spacecraft are shown in Table C.2.

The dbd function from Eq. (3.27) is used instead of the sgn function, because in the limit of the deadband approaching zero the dbd function becomes the sgn function, and the dbd function is preferable for implementation as it reduces chatter. The LQR controller is tuned such that the cost applied to the control inputs yields values that are near to the saturation limits. The gains used for the control laws are shown in the Appendix C.1.

The two primary performance metrics used to measure the overall flatness of the system are the mean-squared angular error and the distance between the two end panels (N and $2N$) in the $\hat{\mathbf{a}}_2$ direction , i.e., $|y_{N/c} - y_{2N/c}|$. These metrics are shown in Fig. 3.4. Oscillations in these metrics correspond to vibrations in the flexible appendages on the spacecraft. Comparing the settling time for these oscillations across different control strategies demonstrate the impact of control in damping structural vibration. To illustrate the impact on individual panels, the angles relative to flat of the outermost panels where the highest offsets would be expected are shown in Fig. 3.5. To illustrate the impact of appendage oscillations on the hub, the error in the hub's attitude and angular velocity is shown in Fig. 3.6. Finally, the actuation effort for the reaction wheel and the torque rod on the outermost panel of the appendage are shown in Fig. 3.7.

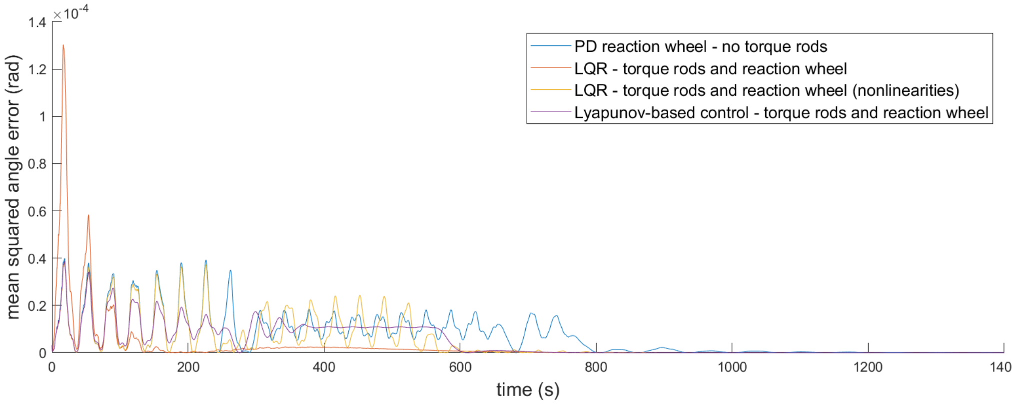

(a) Mean squared angle error

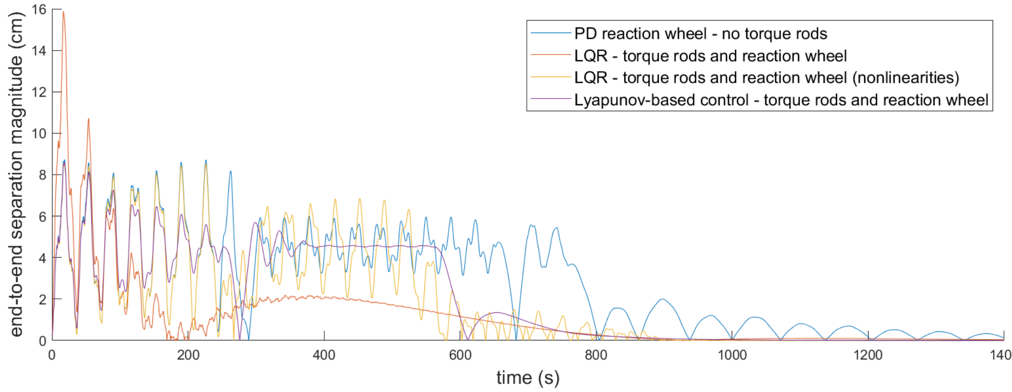

(b) End-to-end separation

Figure 3.4: Comparison of the control performance of PD, LQR, and Lyapunov-based controllers over a 1400 second simulation. In (a) the mean squared angle error is shown and (b) shows the difference in vertical displacement between the two end appendages. The Lyapunov-based controller damps oscillations from the system more quickly than the other controllers.

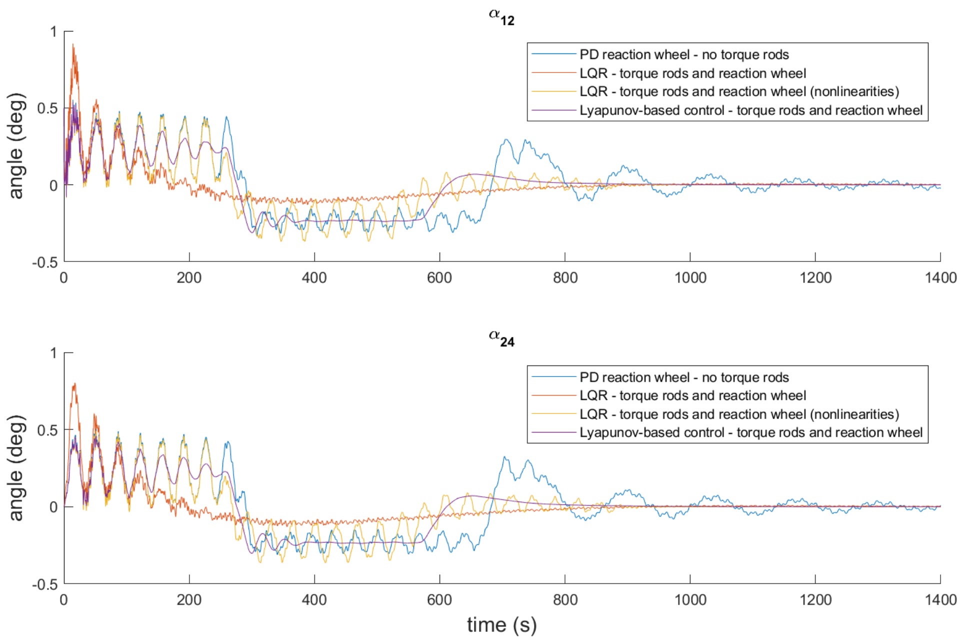

Figure 3.5: Comparison of the control performance of PD, LQR, and Lyapunov-based controllers with respect to the angular offset of the outermost panels over a 1400 second simulation. The Lyapunov-based controller damps angular oscillations more quickly than the other controllers

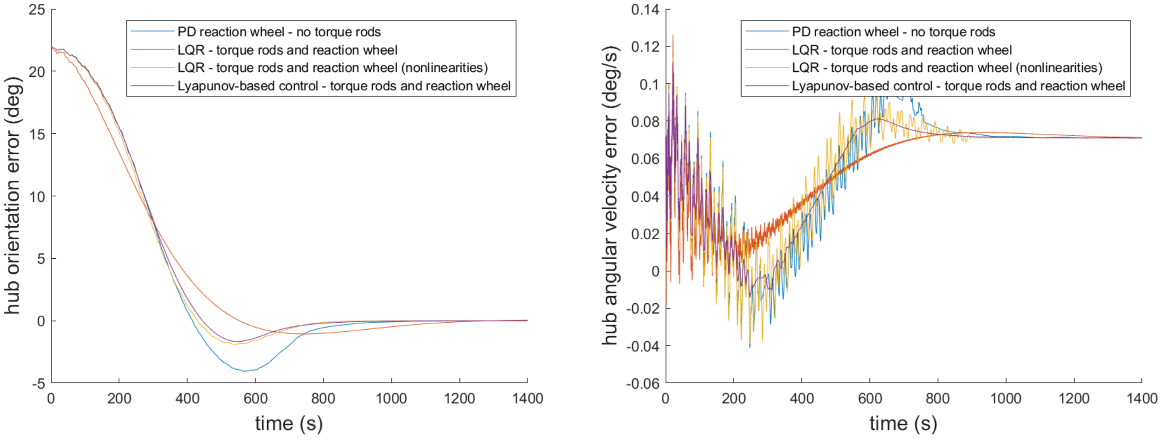

(a) Hub attitude error

(b) Hub angular velocity error

Figure 3.6: Comparison of the control performance of PD, LQR, and Lyapunov-based controllers with respect to the hub attitude and angular velocity over a 1400 second simulation.

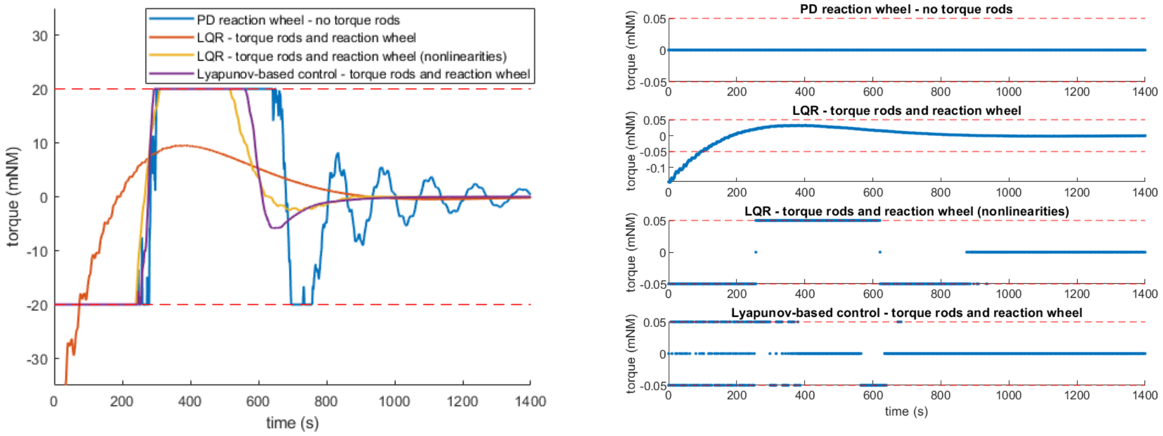

(a) Reaction wheel input

(b) Torque rod input

Figure 3.7: Comparison of the control performance of PD, LQR, and Lyapunov-based controllers over a 1400 second simulation. (a) The reaction wheel control histories and (b) shows the torque rod control history for panel $i = N$. The LQR controller attempts to use the torque rods to assist in the attitude control, as the control inputs mirror each other, whereas the Lypaunov controller mirrors the oscillations shown in the performance metrics because it is used to damp out the oscillations in the appendages.

Simulations show that the Lyapunov-based controller performs better than either of the other two controllers in removing oscillations from the system. Examining Fig. 3.4 and Fig. 3.5 reveals that at around 200 seconds, the oscillations with the Lyapunov-based control are smaller compared to those with other controllers. By 400 seconds, these oscillations have completely damped out, whereas they persist with the other controllers. This effect is also demonstrated in Fig. 3.6b, where some jitter in the angular velocity of the hub due to appendage oscillations is observed persisting after 400 seconds. This jitter is not present with the Lyapunov-based control. For controlling hub attitude, the Lyapunov-based controller performs equivalently to the

LQR controller even with the applied nonlinearities. However, the control input plots shown in Fig. 3.7 indicate that the torque rod control mirrors the shape of the reaction wheel control. This suggests that the LQR controller uses the torque generated by the torque rods to assist the reaction wheel in controlling the hub's attitude and angular velocity. Consequently, the torque rods do not significantly contribute to damping out oscillations. This shortcoming illustrates a challenge of implementing LQR control for high-dimensional systems such as the planar flexible spacecraft model: constructing the Q and R gain matrices requires a separate gain value for each state and input of the system. While the LQR controller is theoretically able to perform at least as well as the Lyapunov-based control, the correct tuning to achieve that performance is difficult to find. In this model, the state space has 146 states and 25 inputs, resulting in 171 different values that must be tuned. Consequently, it becomes difficult to adjust each parameter to values that result in the desired behavior. Conversely, for the Lyapunov-based control, there are only two gains k_p and k_L, which makes tuning the system to achieve the desired behavior simpler.

The performance of the PD control of the reaction wheel and the exclusion of torque rods demonstrate the utility of the torque rods and of incorporating knowledge of the appendage states into the controller. Fig. 3.7a reveals that the control signal for the PD controller takes significantly longer to converge to zero. This is a consequence of the appendages imparting angular momentum to the hub that the controller must manage. The LQR controller uses the full system state and thus can factor the appendages into the control signal, and the Lyapunov-based controller benefits from increased damping as well as some knowledge of the appendages through the β terms.

Orbital Model

A second simulation was performed where the following orbital effects were included: the disturbance resulting from gravity gradient torque modeled in Eq. (3.30), and the time-varying effects of the orientation of the torque rods relative to Earth's magnetic field in Eq. (3.27). The spacecraft parameters used in the previous simulation are utilized. While the orbit remains unchanged, the initial latitude is set to 45 degrees, corresponding to half of the maximum torque available to the torque rods. The initial condition of the hub relative to the nadir reference is kept the same as in the previous simulation.

The flatness metrics are shown in Fig. 3.8 to evaluate controller performance with time-varying control authority of the torque rods and external disturbances. The performance of the controller for the hub's attitude and angular velocity is depicted in Fig. 3.9.

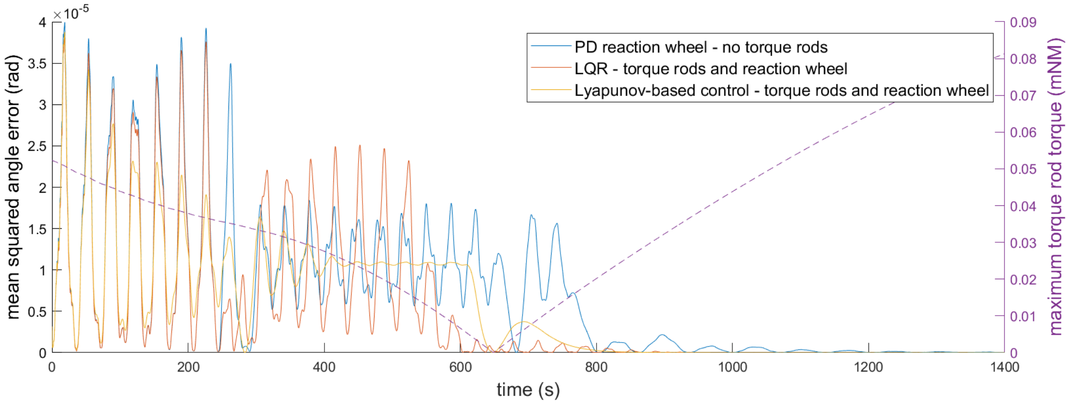

(a) Mean squared angle error

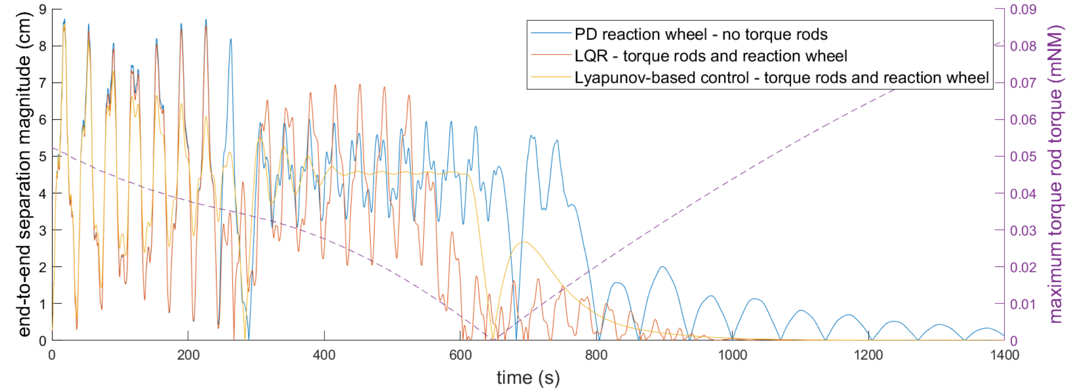

(b) End-to-end separation

Figure 3.8: Comparison of the control performance of PD, LQR, and Lyapunov-based controllers over a 1400 second on-orbit simulation with time-varying control authority. (a) The mean squared angle error and (b) the difference in vertical displacement between the two end appendages.

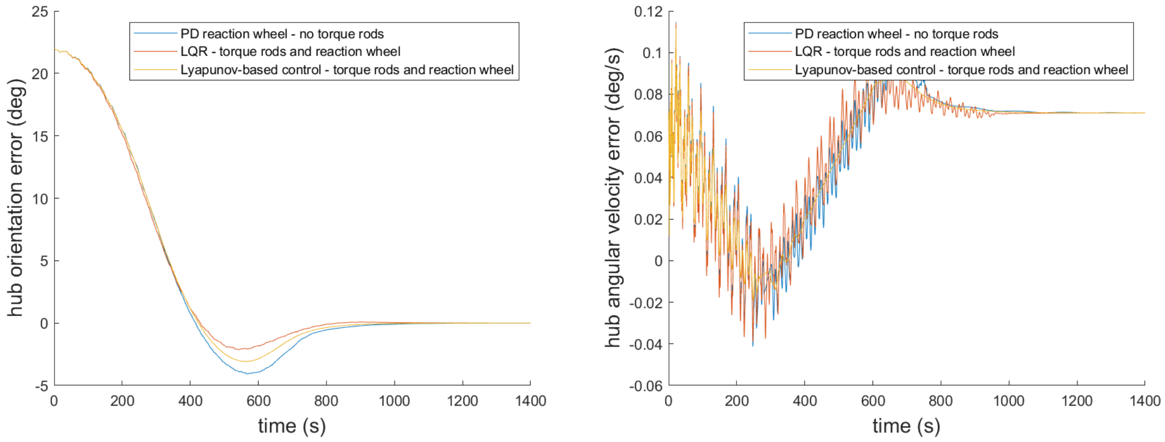

(a) Hub attitude error

(b) Hub angular velocity error

Figure 3.9: Comparison of the control performance of PD, LQR, and Lyapunov-based controllers with time-varying control authority over a 1400 second simulation. (a) The hub attitude error and (b) the hub angular velocity error

The simulations show that despite reduced and time-varying control authority, the Lyapunov-based control law still is able to use the torque rods to damp out the oscillations from the appendages. The damping takes longer to achieve than in the idealized case as a result of the lower average control authority. The added orbital effects have negligible impact on the control of the hub's attitude and angular velocity, suggesting that, for the chosen spacecraft parameters, the gravity gradient torque is easily managed by the controller.

To further illustrate the impact of the time-varying control authority of the torque rods, simulations using the Lyapunov-based control law are conducted across different initial latitudes. For a polar orbit, the control authority at the reference attitude is solely a function of the latitude of the spacecraft. By varying the initial true anomaly at epoch, the available magnetic control authority changes accordingly, demonstrating the sensitivity of the control law to different levels of control authority at epoch. The latitudes chosen are 0 degrees, 45 degrees, and 90 degrees, corresponding to having zero, half of the maximum, and the maximum torque available to the torque rods at the start of the simulation, respectively. Fig. 3.10 depicts the torque available over the duration of the simulation for each initial condition.

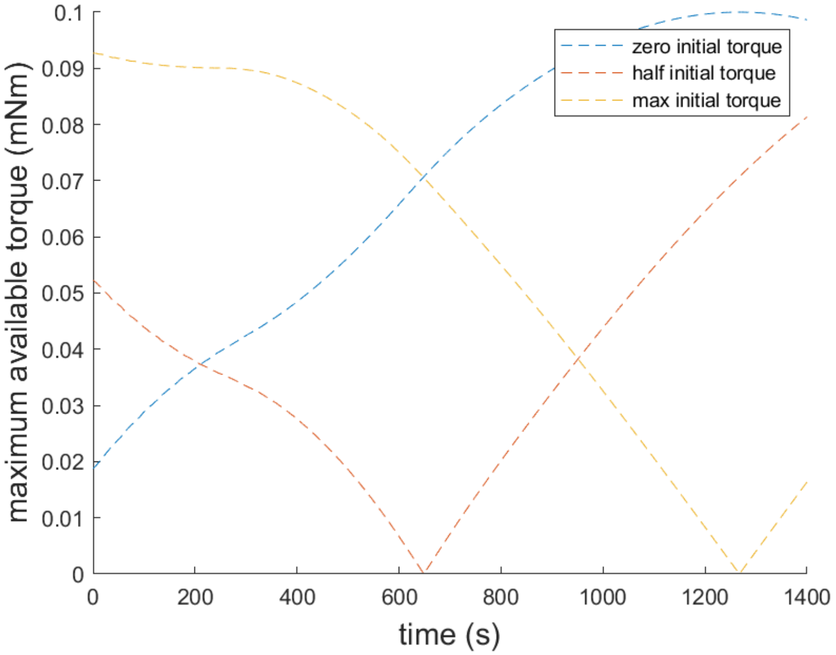

Figure 3.10: Available torque to torque rods

The flatness metrics are shown in Fig. 3.11 to evaluate the differences in controller performance with varying levels of control authority available. The performance of the controller for the hub's attitude and angular velocity is depicted in Fig. 3.12.

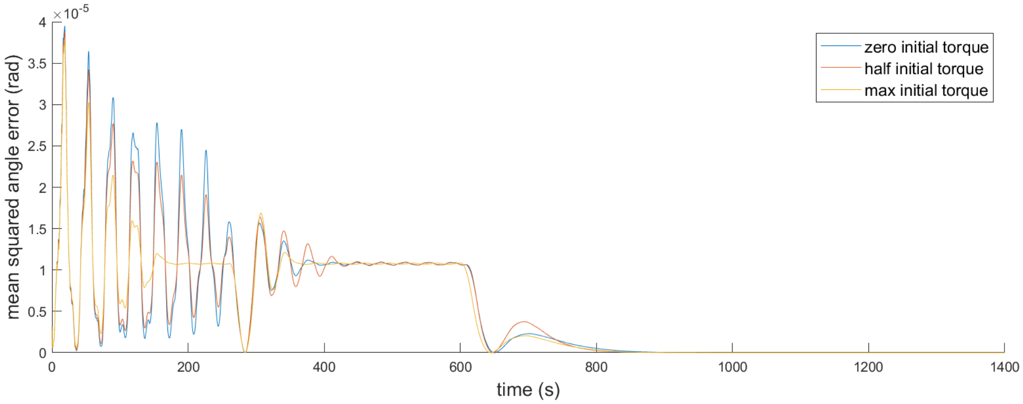

(a) Mean squared angle error

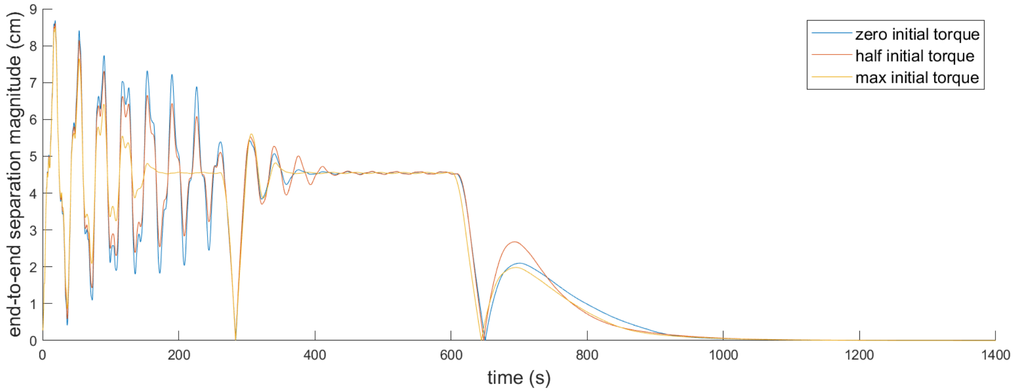

(b) End-to-end separation

Figure 3.11: Comparison of the the Lyapunov-based controller with varying levels of torque rod control authority initially available over a 1400 second simulation. (a) The mean squared angle error and (b) the difference in vertical displacement between the two end appendages.

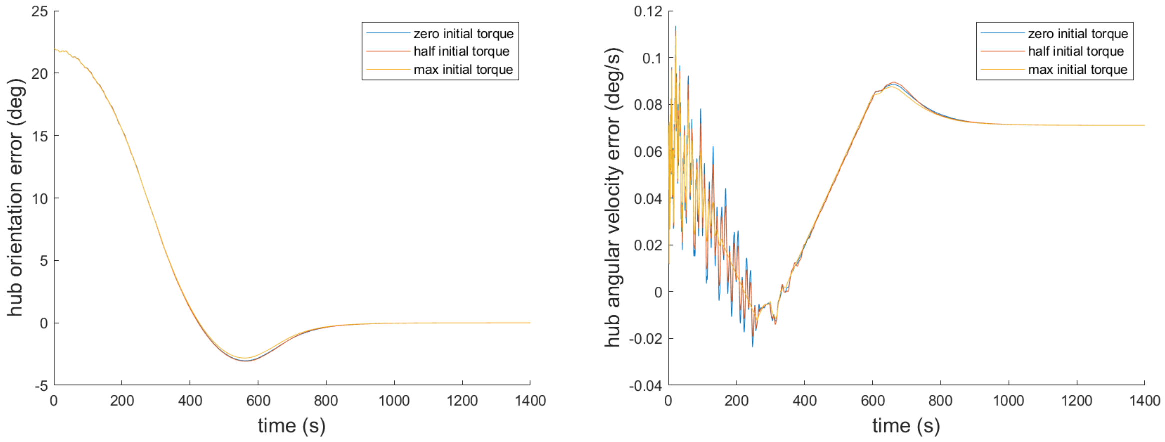

(a) Hub attitude error

(b) Hub angular velocity error

Figure 3.12: Comparison of the the Lyapunov-based controller with varying levels of torque rod control authority initially available over a 1400 second simulation.(a) The hub attitude error and (b) the hub angular velocity error

The simulation results in Fig. 3.11 demonstrate that even when starting with the minimum available torque, induced oscillations can still be removed from the system, albeit at a slower rate. They also illustrate that, for best performance in achieving flatness, having more torque available to the torque rods at the beginning of a maneuver enables quicker damping of induced oscillations. Further characterization of this behavior would be useful for a spacecraft mission designer, as it would enable them to plan maneuvers at times when a desired level of flatness could be maintained.

Fig. 3.12 demonstrates that the torque rods have a minor impact on the attitude and angular velocity of the hub. During maneuvers, the additional angular momentum of the appendages effectively increases the rotational inertia of the hub. The torque rods act to counteract the angular momentum of the appendages relative to the hub, thereby diminishing this effect. Consequently, the scenario with maximum initial torque exhibits slightly smaller overshoot compared to the other cases. This leads to a reduction in the control effort required for the reaction wheels, although the effect is limited by the relatively small magnitude of torque generated by the torque rods.

3.4 Output Feedback Control

This section considers an observer to estimate the the system state from a limited set of measurements. The controller described in Section 3.3 is paired with an observer in an output feedback control framework.

3.4.1 Measurement Function and State Estimation

In most applications, information about the full state of a system is not measured or available as input to a state feedback controller. Consequently, a state estimator must be used to convert measurements into state estimates that can then be used as inputs to the controller. The nonlinear dynamics of the system with the linearized model developed in Section 3.3 makes this model well suited for an Extended Kalman Filter (EKF). An EKF is an estimator that applies a Kalman filter to the dynamics of a nonlinear system linearized about an equilibrium point [71]. An EKF is performed using two steps: a prediction step and an update step. Given a state-space system in discrete time defined as

$$\boldsymbol{\eta}_{k+1} = \boldsymbol{f}(\boldsymbol{\eta}_k, \boldsymbol{u}_k) \tag{3.73}$$

$$\boldsymbol{z}_k = h(\boldsymbol{\eta}_k), \tag{3.74}$$

an EKF is implemented as follows.

The prediction step is [71]

$$\hat{\eta}_{k|k-1} = \mathbf{f}(\hat{\eta}_{k-1|k-1}, \boldsymbol{u}_k). \tag{3.75}$$

$$P_{k|k-1} = A_k P_{k-1|k-1} A_k^T + Q_k, \tag{3.76}$$

where A_k is the Jacobian of the system dynamics evaluated at the current state estimate, and Q_k is the process noise covariance. The update step to incorporate the measurement data is [71]

$$\tilde{y}_k = \boldsymbol{z}_k - h(\hat{\eta}_{k|k-1}) \tag{3.77}$$

$$S_k = C_k P_{k|k-1} C_k^T + R_k \tag{3.78}$$

$$K_k = P_{k|k-1} C_k^T S_k^{-1} \tag{3.79}$$

$$\hat{\eta}_{k|k} = \hat{\eta}_{k|k-1} + K_k \tilde{y}_k \tag{3.80}$$

$$P_{k|k} = (I - K_k C_k) P_{k|k-1} \tag{3.81}$$

where C_k is the linearized measurement equation $\frac{\partial h}{\partial \boldsymbol{\eta}}$ evaluated at the current state estimate and R_k is the measurement noise covariance.

Assume that the attitude and angular velocity of the hub and the rates of each of the panels relative to the hub are measured directly, e.g.,

$$\boldsymbol{z}_k = \begin{bmatrix} \gamma & \dot{\gamma} & \dot{x}_{1/C} & \dot{y}_{1/C} & \dot{\alpha}_{1/C} & \cdots & \dot{x}_{2N/C} & \dot{y}_{2N/C} & \dot{\alpha}_{2N/C} \end{bmatrix}^T. \tag{3.82}$$

The resulting measurement function is a linear function of the state and can be expressed in block matrix form

$$C = \begin{bmatrix} H_c & 0 & 0 & \dots & 0 \\ 0 & H_i & 0 & \dots & 0 \\ 0 & 0 & H_i & \dots & 0 \\ 0 & 0 & 0 & \ddots & 0 \\ 0 & 0 & 0 & 0 & H_i \end{bmatrix}, \tag{3.83}$$

where

$$H_c = \begin{bmatrix} 1 & 0 \\ 0 & 1 \end{bmatrix},$$

and

$$H_i = \begin{bmatrix} 0 & 0 & 0 & 1 & 0 & 0 \\ 0 & 0 & 0 & 0 & 1 & 0 \\ 0 & 0 & 0 & 0 & 0 & 1 \end{bmatrix}.$$

The measurement function is described by a matrix multiplication, $h(\boldsymbol{\eta}) = C\boldsymbol{\eta}$, and can be directly used in the EKF.

To evaluate its suitability in an output feedback control framework, an EKF was implemented and applied to a numerical simulation of the unforced dynamics of the system. The simulation consisted of setting the initial condition of the system to a point in state space a small distance away from the equilibrium point and simulating the resulting unforced dynamic response. Gaussian noise is applied to the measurement of the system and the initial estimate of the EKF is set to the equilibrium point. See Appendix C.1 for the parameters used for the EKF. To measure the performance of the EKF, plots of the state estimate error are shown. Specifically plots of the attitude estimate error of the hub, and the mean error magnitude of the appendages attitude, angular velocity, and vertical displacement are used.

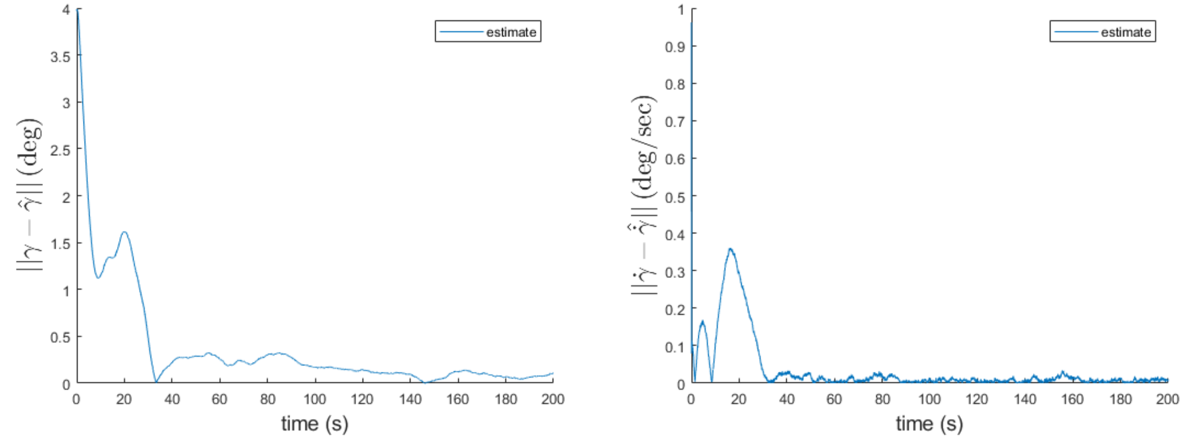

(a) Hub attitude error

(b) Hub angular velocity error

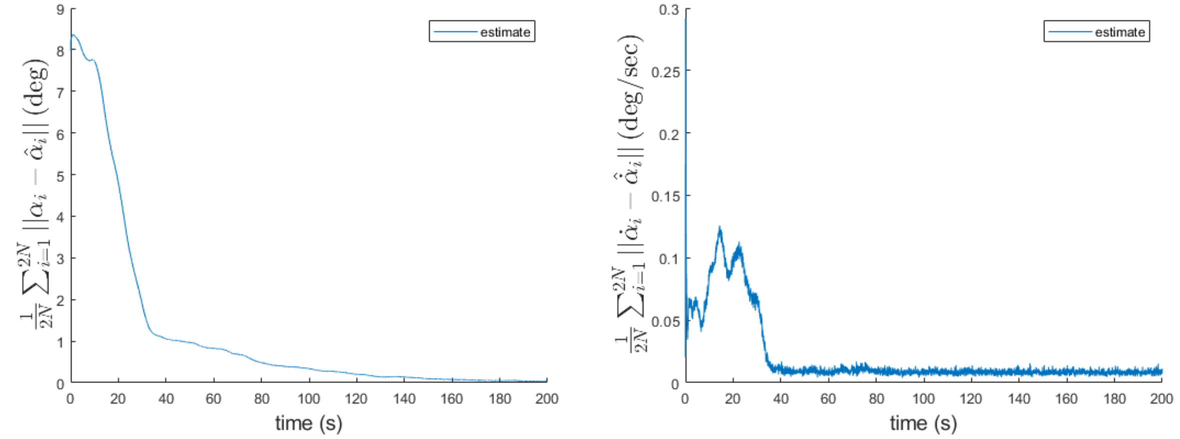

(c) Average panel attitude error

(d) Average panel angular velocity error

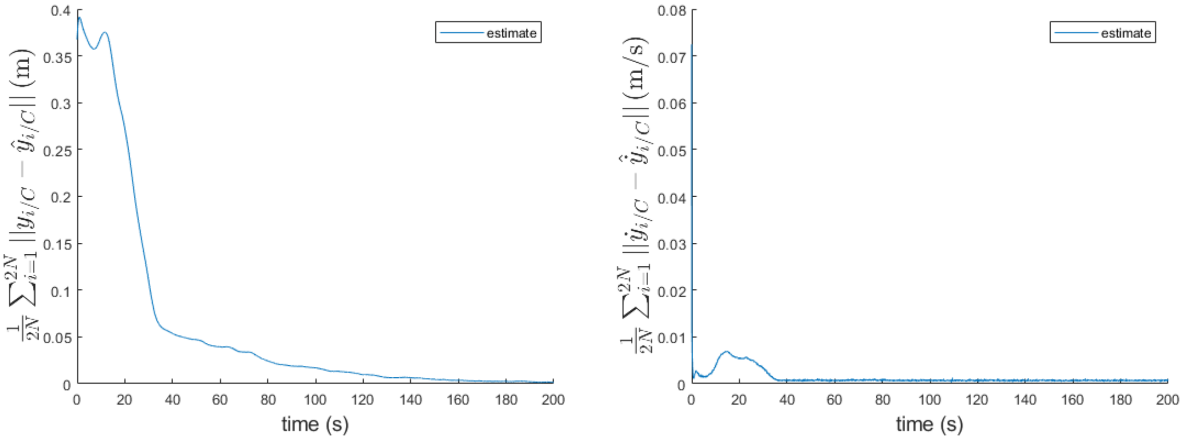

(e) Average panel displacement error

(f) Average panel velocity error

Figure 3.13: State estimation error of the extended Kalman filter applied to a simulation of the system's unforced dynamics. (a) The estimation error magnitude of the hub attitude, (b) the estimation error magnitude of the hub angular velocity, (c) the average panel attitude estimation error magnitude, (d) the average panel angular velocity estimation error magnitude, (e) the average panel displacement estimation error magnitude, and (f) the average panel velocity estimation error magnitude. The state estimate converges to the true state estimate after around 150 seconds, with some residual noise left in the angular velocity estimate.

The numerical simulations show that the state estimate converges to the true state around 150 seconds, except for the panel angular velocity estimates, which retains some of the measurement noise. This effect is likely due to the stiffness of the state space system causing the estimator to respond to variations in the angular rate measurements too quickly. However, these effects can be mitigated in the output feedback controller by setting the deadband for the torque rods such that near an angular velocity of zero, the residual noise will fall within the deadband and not cause noisy control inputs.

3.4.2 Simulation Results

The state estimator was then used in an output feedback control framework. In this simulation the same estimator parameters are used. The simulation parameters and initial conditions are the same as the orbital model with orbital effects and disturbances as in Section 3.3.3. The initial state estimate is set to be the same as the initial condition. In practice, between maneuvers after the oscillations have been damped out, the state estimate will have converged to the equilibrium (flat state) and will thus be approximately true once the next maneuver begins. Each of the controllers in Section 3.3 are implemented with output feedback and the performance of each are compared with the the Lyapunov controller with state feedback. The flatness metrics, angles relative to flat of the outermost panels, and the hub's attitude and angular velocity error are shown in are shown in Fig. 3.14, the angles relative to flat of the outermost panels are shown in Fig. 3.15, and the error in the hub's attitude and angular velocity is shown in Fig. 3.16.

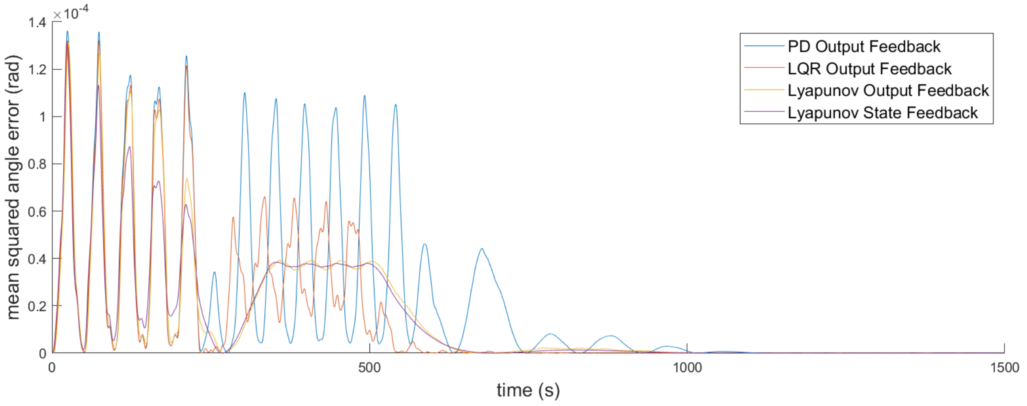

(a) Mean squared angle error

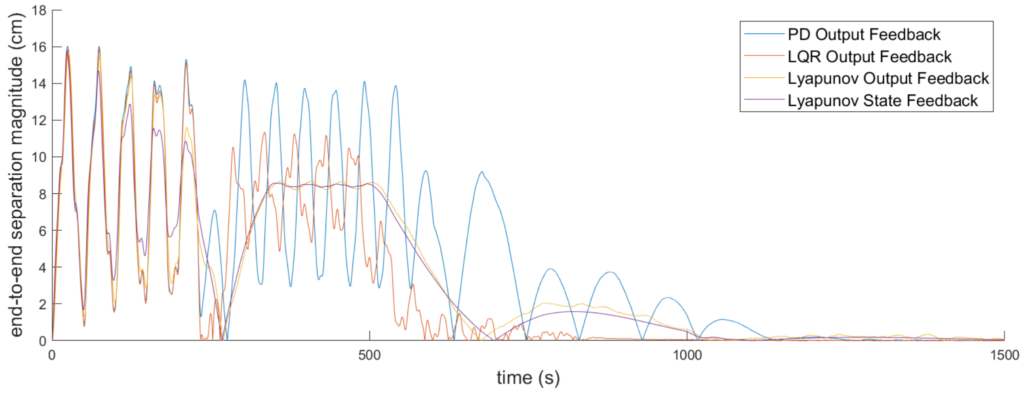

(b) End-to-end separation

Figure 3.14: Comparison of PD, LQR, and Lyapunov-based controllers using output feedback and Lyapunov state feedback control. In (a) the mean squared angle error is shown and (b) shows the difference in vertical displacement between the two end appendages.

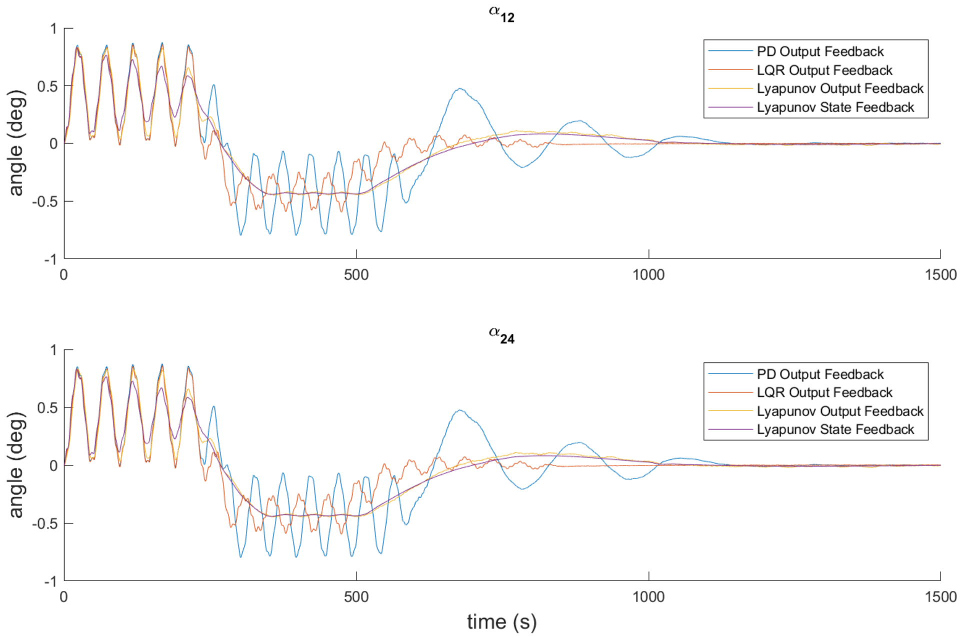

Figure 3.15: Comparison of PD, LQR, and Lyapunov-based controllers using output feedback and Lyapunov state feedback control with respect to the angular offset of the outermost panels.

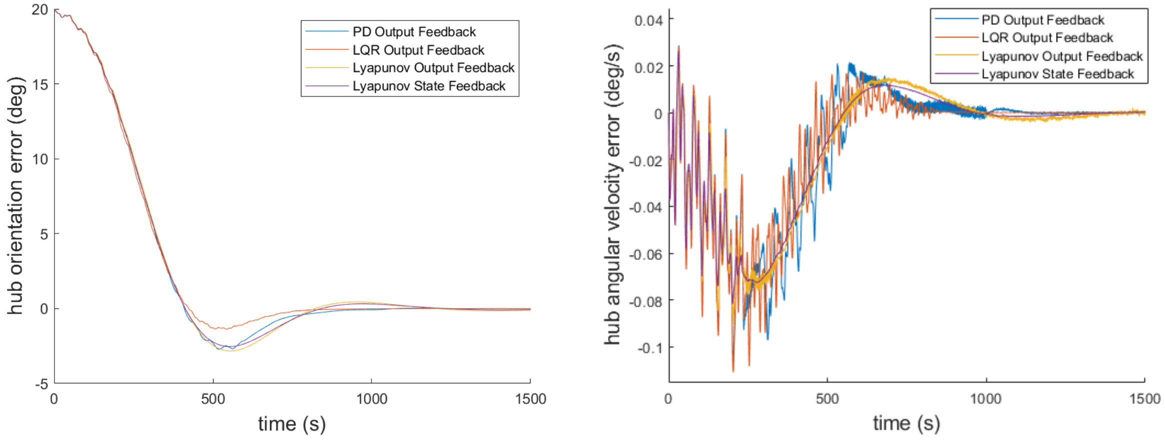

(a) Hub attitude error

(b) Hub angular velocity error

Figure 3.16: Comparison of the control performance of PD, LQR, and Lyapunov-based controllers using output feedback with Lyapunov-based state feedback control with respect to the hub attitude and angular velocity error.

The output feedback control is able to achieve the control objectives of tracking a reference attitude and angular velocity while removing oscillations from the structure to maintain flatness. For attitude tracking, the output feedback controller retains the performance of the state feedback control. For shape control, the Lyapunov controller in output feedback does help to damp out structural oscillations, although not as quickly as the state feedback control. Specifically, while the settling time of each control is similar, the damping between 100-300 seconds in the simulation is more significant for the state feedback control. Because the controller relies on the estimate of the angular velocity of each of the panels, this reduction in performance can be attributed to the time it takes for the angular velocity estimates to converge.

3.5 Conclusion

This chapter proposes a feedback control law for a spacecraft model consisting of a central hub and multiple flexibly connected appendages on either side of this hub. This model could represent either the flexibility of a large single appendage or the behavior of a deployable space structure after it had been deployed. To control the shape and attitude of this model, actuation consisting of a reaction wheel on the hub and magnetic torque rods on each of the appendages is proposed. Springs to model internal forces and moments, external disturbances, and actuator constraints are considered in modeling the dynamics of the system. The nonlinearities in the model suggest a Lyapunov-based approach to the control design. By performing Lyapunov analysis on the system dynamics, feedback control laws for the reaction wheel and each torque rod are obtained. Numerical simulations show that the proposed controller removes vibrations from the system more quickly than both a system without torque rods and a system with torque rods but with a different control law. The implementation of an Extended Kalman filter provides state estimation from a measurement of the rate terms of each component of the spacecraft. The EKF combined with the Lyapunov-based control and numerical simulations demonstrated stabilization of the system with output feedback control. The output feedback controller retains most of the performance of the state feedback control.

Chapter 4: Attitude and Shape Control of a Flexible Spacecraft in Three Dimensions

4.1 Introduction

In this chapter, I extend the planar flexible spacecraft model to a full three-dimensional model using similar concepts. In the 3D model, the appendage is considered planar instead of one-dimensional. The flexibility of the appendage is similarly modeled via discretization into individual flexibly connected panels; however, compared with the planar model, the appendage is discretized along two different axes. I extend the multibody dynamics to three dimensions using rotation matrices to represent the attitude of each component. Like the planar model, I model the panel connections with stiff damped springs to simulate the physical panel connections and a damped torsional spring to simulate flexibility between panels. However, unlike the planar model, the panels are not constrained to rotate in only one direction.

In three dimensions, the torque generated by the magnetic torque rods is no longer isolated to a fixed axis of rotation. Furthermore, to control the additional rotational degrees of freedom of a panel, an additional torque rod per panel is required. However, the additional torque rod results in an output torque that is coupled, meaning the direction cannot be fully specified by the input, as described in Section 2.1.3. To address the actuation of magnetic torque rods for shape control, I first consider a single panel actuated by two magnetic torque rods. Using the reduced-attitude representation to describe the panel's attitude, I employ Lyapunov's direct method to derive a control law that stabilizes the relevant degrees of freedom. This control law is also applicable for controlling the reduced attitude of a rigid spacecraft for pointing applications, as demonstrated by simulations.

I apply the derived torque rod control law to each torque rod pair on the panels of the three-dimensional spacecraft model to implement shape control. Through simulation, I investigate the performance of the controller and assess the impact of shape control in response to two types of disturbances: maneuver-induced oscillations and thermoelastic bending.

The contributions of this chapter are (1) a nonlinear feedback control law for two-axis attitude control of a rigid body actuated by two magnetic torque rods; (2) a state-space representation of the dynamics of a spacecraft consisting of a hub and a planar flexible appendage modeled by a discretized set of flexibly connected elements; and (3) simulation validation demonstrating that applying the magnetic torque rod control law to the spacecraft model effectively removes vibrations of the flexible appendage.

The remainder of the chapter is organized as follows: Section 4.2 presents the proposed three-dimensional spacecraft model; Section 4.3 describes two-axis attitude control, derives a control law for two magnetic torque rods using Lyapunov analysis, and validates the control law through simulation on a single rigid body; Section 4.4 proposes a control design to achieve attitude and shape control of the spacecraft model and is validated via simulation; Section 4.5 provides a summary of the chapter.

4.2 Three-Dimensional Flexible Spacecraft Model

Consider a spacecraft consisting of a hub and a large flexible appendage connected to the hub. This appendage could represent a large solar array, antenna, solar sail, or other relevant structure. To model the flexibility of the structure, assume that the appendage is modeled as a discretized set of flexibly connected rigid square elements referred to as panels. This modeling choice can represent a deployable structure that is folded for launch and deployed in space, but by varying the size of the panel discretization and the flexibility of the panel connections, can be generalized to represent a continuous flexible planar structure.

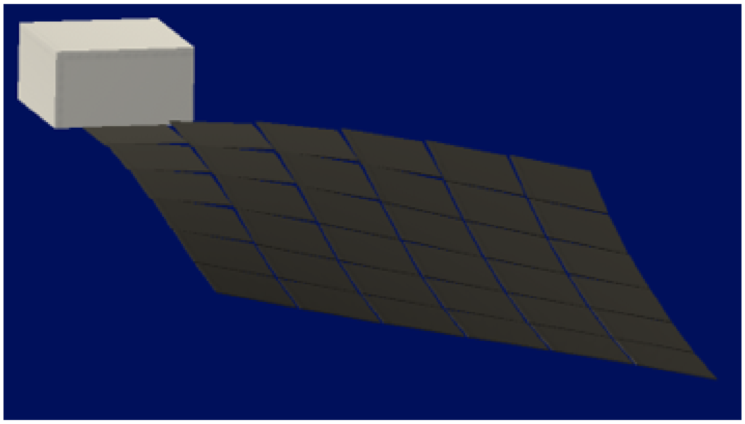

Figure 4.1: Spacecraft with a hub and a flexible appendage modeled as N flexibly connected panels

Consider an Earth-centered inertial frame $\mathcal{I} = (O, \hat{\mathbf{e}}_x, \hat{\mathbf{e}}_y, \hat{\mathbf{e}}_3)$, a body-fixed frame affixed to the central hub of the spacecraft $\mathcal{A} = (C, \hat{\mathbf{a}}_1, \hat{\mathbf{a}}_2, \hat{\mathbf{a}}_3)$, and body-fixed frames affixed to each of the component panels of the appendage $\mathcal{B}^{(i)} = (B^{(i)}, \hat{\mathbf{b}}_1^{(i)}, \hat{\mathbf{b}}_2^{(i)}, \hat{\mathbf{b}}_3^{(i)})$, $i = 1, ..., 2N$. The panels are assumed to all be the same size with side length L, and their body-fixed reference frames are such that the origin is at the center of the panel, and the $\hat{\mathbf{b}}_1^{(i)}$ and $\hat{\mathbf{b}}_2^{(i)}$ axes are aligned with the panel edges.

The state of the hub consists of its position, velocity, attitude, and angular velocity, i.e.,

$$\boldsymbol{\eta}_C = \begin{bmatrix}\mathbf{r}_{C/O} & \mathbf{v}_{C/O} & R_C & \boldsymbol{\omega}_C\end{bmatrix}^T, \tag{4.1}$$

where the attitude is represented by a rotation matrix. To better capture the shape of the flexible appendage with the states of the panels, the position and velocity of the panels relative to and in the reference frame of the hub are used, i.e.,

$$\boldsymbol{\eta}_i = \begin{bmatrix}\mathbf{r}_{i/C} & \mathbf{v}_{i/C} & R_{B_i} & \boldsymbol{\omega}_{B_i}\end{bmatrix}^T. \tag{4.2}$$

The state of the full spacecraft model is then a concatenation of the hub and all panels making up the appendage, i.e.,

$$\boldsymbol{\eta} = [\boldsymbol{\eta}_C \quad \boldsymbol{\eta}_1 \quad \boldsymbol{\eta}_2 \quad \dots \quad \boldsymbol{\eta}_N]^T, \tag{4.3}$$

where N is the number of elements comprising the appendage.

4.2.1 Spacecraft Attitude and Shape Dynamics

The dynamics for the state of the hub are as follows:

$$\begin{aligned} \dot{\mathbf{r}}_{C/O} &= \dot{\mathbf{v}}_{C/O} && (4.4)\\ \dot{\mathbf{v}}_{C/O} &= \frac{\boldsymbol{F}_C}{m_C} && (4.5)\\ \dot{R}_C &= R_C \boldsymbol{\omega}_C^{\times} && (4.6)\\ J_C \dot{\boldsymbol{\omega}}_C &= -\boldsymbol{\omega}_C^{\times} J_C \boldsymbol{\omega}_C + \boldsymbol{M}_C && (4.7) \end{aligned}$$

where the $^\times$ operator is a mapping from $\mathbb{R}^3$ to a 3×3 skew-symmetric matrix such that $a^\times b = a \times b$, where $\boldsymbol{\tau}_C$ is the total external torque experienced by the hub, and where the derivatives are taken with respect to the inertial frame.

To derive the dynamics of each panel in the reference frame of the hub, the inertial frame dynamics must first be considered. The position of panel i in the inertial frame is

$$\mathbf{r}_{i/O} = \mathbf{r}_{C/O} + \mathbf{r}_{i/C}. \tag{4.8}$$

Differentiating twice yields the acceleration of each panel in the inertial frame, i.e.,

$$\boldsymbol{a}_{i/O} = \boldsymbol{a}_{C/O} + \boldsymbol{a}_{i/C} + \dot{\boldsymbol{\omega}}_C \times \boldsymbol{r}_{i/C} + 2\boldsymbol{\omega}_C \times \boldsymbol{v}_{i/C} + \boldsymbol{\omega}_C \times (\boldsymbol{\omega}_C \times \boldsymbol{r}_{i/C}). \tag{4.9}$$

Rearranging and substituting in $\boldsymbol{F}_C = m_C \boldsymbol{a}_C$ and $\boldsymbol{F}_i = m_i \boldsymbol{a}_i$, where $\boldsymbol{F}_C$ and $\boldsymbol{F}_i$ are the total forces on the hub and ith panel respectively, yields

$$\boldsymbol{a}_{i/C} = \frac{\boldsymbol{F}_i}{m_i} - \frac{\boldsymbol{F}_C}{m_C} - \dot{\boldsymbol{\omega}}_C \times \boldsymbol{r}_{i/C} - 2\boldsymbol{\omega}_C \times \boldsymbol{v}_{i/C} - \boldsymbol{\omega}_C \times (\boldsymbol{\omega}_C \times \boldsymbol{r}_{i/C}). \tag{4.10}$$

The dynamics for the ith panel are

$$\begin{aligned}
\dot{\mathbf{r}}_{i/C} &= \dot{\mathbf{v}}_{i/C} && (4.11)\\
\dot{\mathbf{v}}_{i/C} &= \frac{\boldsymbol{F}_i}{m_i} - \frac{\boldsymbol{F}_C}{m_C} - \dot{\boldsymbol{\omega}}_C \times \boldsymbol{r}_{i/C} - 2\boldsymbol{\omega}_C \times \boldsymbol{v}_{i/C} - \boldsymbol{\omega}_C \times (\boldsymbol{\omega}_C \times \boldsymbol{r}_{i/C}) && (4.12)\\
\dot{R}_{B_i} &= R_{B_i} \boldsymbol{\omega}_{B_i}^{\times} && (4.13)\\
J_{B_i} \dot{\boldsymbol{\omega}}_{B_i} &= -\boldsymbol{\omega}_{B_i}^{\times} J_{B_i} \boldsymbol{\omega}_{B_i} + \boldsymbol{M}_i && (4.14)
\end{aligned}$$

4.2.2 Flexural Modeling and Dynamics

Assume that each of the panels are connected to each adjacent panel and at each connection there is a torsional spring that generates a restoring moment for adjacent panels with offset attitudes. In order to avoid the unnecessary complexities associated with explicitly considering the panel connections as constraints, the attachment force of each panel is modeled as a stiff damped spring with spring coefficient k_s and damping coefficient c_s. Assume the torsional springs at adjacent panels are linearly proportional to the relative angle between the panels that it connects, with spring coefficient k_t and damping coefficient c_t. With the spring modeling, the attachment force and resulting moment between two adjacent panels can be computed from the relative position and velocity of the panel edges. The position of an edge in a panel's reference frame is

$$\mathbf{L} = \pm \begin{bmatrix} \frac{L}{2} & 0 & 0 \end{bmatrix} \quad \text{or} \quad \pm \begin{bmatrix} 0 & \frac{L}{2} & 0 \end{bmatrix}. \tag{4.15}$$

The relative position between the edges of two adjacent panels i and j is

$$\mathbf{r}_{i,j/\text{edge}} = \mathbf{r}_{i/C} + R_{C/B_i}\mathbf{L} - (\mathbf{r}_{j/C} - R_{C/B_i}\mathbf{L}), \tag{4.16}$$

where R_{C/B_i} is the rotation matrix from B_i to C computed by $R_{C/B_i} = R_C^T R_{B_i}$. The relative velocity between the edges of panels i and j is derived by taking the derivative of $\mathbf{r}_{i,j/\text{edge}}$, which yields

$$\mathbf{v}_{i,j/\text{edge}} = \mathbf{v}_{i/C} + R_{C/B_i}(\boldsymbol{\omega}_i - R_{B_i/C}\boldsymbol{\omega}_C) \times \mathbf{L} - (\mathbf{v}_{j/C} + R_{C/B_i}(\boldsymbol{\omega}_j - R_{B_i/C}\boldsymbol{\omega}_C) \times (-\mathbf{L})) \tag{4.17}$$

The force on panel i resulting from panel j is

$$\mathbf{F}_{i,j} = -k_s \mathbf{r}_{i,j/\text{edge}} - c_s \mathbf{v}_{i,j/\text{edge}}, \tag{4.18}$$

where $\boldsymbol{F}_{j,i} = -\boldsymbol{F}_{i,j}$. The moment on i resulting from the attachment with j is

$$\mathbf{T}_{i,j} = \mathbf{L} \times (R_{B_i/C}\mathbf{F}_{i,j}). \tag{4.19}$$

Similarly, the moment arising from the torsional spring between two adjacent panels is computed from the relative attitude and angular velocity of adjacent panels. Assume that the restoring moment opposes the relative orientation of adjacent panels. The matrix logarithm of a rotation matrix parameterizes a rotation in three-dimensional space by a direction $\boldsymbol{\xi}$ and magnitude θ of rotation providing a convenient way to define the magnitude and direction of the restoring moment induced by the torsional spring. The matrix logarithm of a rotation matrix R is

$$\text{logm}(R) = \begin{cases} \theta = \cos^{-1}\left(\frac{\text{Trace}(R)-1}{2}\right) \in \mathbb{R} \\ \boldsymbol{\xi} = \frac{1}{2\sin\theta} \begin{bmatrix} r_{32} - r_{23} \\ r_{13} - r_{31} \\ r_{21} - r_{12} \end{bmatrix} \in \mathbb{R}^3 \end{cases} \tag{4.20}$$

The relative orientation between adjacent panels i and j is computed by taking $\text{logm}(R_{B_i/B_j})$ to get $\theta_{i,j}$ and $\boldsymbol{\xi}_{i,j}$. The relative angular velocity between adjacent panels i and j is the difference between their angular velocities given in reference frame $B^{(i)}$, i.e.,

$$\boldsymbol{\omega}_{i,j} = \boldsymbol{\omega}_i - R_{B_i/B_j}\boldsymbol{\omega}_j. \tag{4.21}$$

The resulting moment is

$$\mathbf{M}_{i,j} = -k_t\theta\boldsymbol{\xi}_{i,j} - c_t\boldsymbol{\omega}_{i,j}. \tag{4.22}$$

Assume that the spacecraft is subject to gravity from Earth, that there is some 3 axis control system on the hub, e.g., a set of reaction wheels, and that the appendage is connected to the hub via a single panel indexed $i = 1$. Then the total force and moment exerted on the hub via the flexible appendage is

$$\boldsymbol{F}_C = -\mu m_C \frac{\mathbf{r}_{C/O}}{\|\mathbf{r}_{C/O}\|^3} + \boldsymbol{F}_{C,1} \tag{4.23}$$

$$\boldsymbol{M}_C = \boldsymbol{T}_{C,1} + \boldsymbol{M}_{C,1} + \boldsymbol{u}_C. \tag{4.24}$$

The total force and moment on each panel comprising the appendage is

$$\boldsymbol{F}_i = -\mu m_i \frac{\mathbf{r}_{i/O}}{\|\mathbf{r}_{i/O}\|^3} + \sum_{j\in\mathcal{N}_i} \boldsymbol{F}_{i,j} \tag{4.25}$$

$$\boldsymbol{M}_i = \sum_{j\in\mathcal{N}_i} \left(\boldsymbol{T}_{i,j} + \boldsymbol{M}_{i,j}\right), \tag{4.26}$$

where $\mathcal{N}_i$ is the set of all panels connected to panel i.

4.2.3 Control Input Model

Assume that the hub has three reaction wheels aligned with each of its body frame axes, i.e., $(\hat{\mathbf{a}}_1, \hat{\mathbf{a}}_2, \hat{\mathbf{a}}_3)$. Assume also that each reaction wheel has some saturation limit K_{rw} and that the control input is simply the reaction wheel torque. The saturation is applied to each reaction wheel individually. The torque generated by the reaction wheels in response to control input $\boldsymbol{u}_{\text{rw}}$ is

$$\boldsymbol{\tau}_{\text{rw}} = \begin{bmatrix} \text{sat}(u_{\text{rw},1}) & \text{sat}(u_{\text{rw},2}) & \text{sat}(u_{\text{rw},3}) \end{bmatrix}^T \tag{4.27}$$

where the subscript denotes each axis component of the control input and where

$$\text{sat}(u_{\text{rw},k}) = \begin{cases} -K_{\text{rw}} & u_{\text{rw},k} \leq -K_{\text{rw}} \\ u_{\text{rw},k} & -K_{\text{rw}} < u_{\text{rw},k} < K_{\text{rw}} \\ K_{\text{rw}} & u_{\text{rw},k} \geq K_{\text{rw}}. \end{cases}$$

Assume that each panel is equipped with two magnetic torque rods lying orthogonally in the plane of the panel and to each other. Specifically, the torque rods on panel i are aligned with axes $\hat{\mathbf{b}}_1^{(i)}$ and $\hat{\mathbf{b}}_2^{(i)}$ and orthogonal to $\hat{\mathbf{b}}_3^{(i)}$. Assume the control input to each $u_1^{(i)}, u_2^{(i)}$ corresponds to the strength of the magnetic dipole generated, m_1, m_2. Assume that each torque rod has a maximum strength dipole that it can generate, denoted as K_{tr}. The magnetic dipole generated by the control inputs to panel i expressed in the body frame is

$$\boldsymbol{m} = \begin{bmatrix} m_1 & m_2 & 0 \end{bmatrix}^T \tag{4.28}$$

where

$$m_k = \begin{cases} -K_{\text{tr}} & u_k \leq -K_{\text{tr}} \\ u_k & -K_{\text{tr}} < u_k < K_{\text{tr}} \\ K_{\text{tr}} & u_k \geq K_{\text{tr}}. \end{cases} \tag{4.29}$$

The resulting moment in the body frame is

$$\boldsymbol{\tau}_{\text{tr}} = \boldsymbol{m} \times \boldsymbol{B} = \begin{bmatrix} m_2 B_3 & -m_1 B_3 & m_1 B_2 - m_2 B_1 \end{bmatrix}^T, \tag{4.30}$$

where $\boldsymbol{B}$ is the local magnetic field of the Earth expressed in the body frame of the spacecraft.

4.3 Two-Axis Attitude Control Using Two Magnetic Torque Rods

To determine a control law for the magnetic torque rods, consider a single panel from the flexible appendage with a magnetic torque rod pair as described in Section 4.2.3. Assume that its attitude is parameterized by a rotation matrix and the dynamics evolve on $SO(3)$ as described in Section 2.1. With only two magnetic torque rods, it is not possible to control the full attitude of the panel. When part of the flexible appendage, rotations about the $\hat{\boldsymbol{b}}_3^{(i)}$ axis relative to the hub or neighboring panels are not relevant, as the geometric constraints enforced by the panel connections render rotations in this direction negligible. The objective of controlling a panel's attitude, when it is part of the appendage, is to ensure that it and its neighbors remain flat relative to the hub. Explicitly, this objective can be defined as aligning the $\hat{\boldsymbol{b}}_3^{(i)}$ axis of each panel with the $\hat{\boldsymbol{a}}_3$ axis of the hub.

When considering the panel as a separate entity, akin to a small spacecraft actuated by only two magnetic torque rods, an analogous problem arises: pointing control of a spacecraft. Solving this analogous problem effectively addresses the challenge of performing shape control using two magnetic torque rods. The problem of pointing control of a spacecraft is now addressed.

Assume that the objective of the spacecraft is to point an onboard instrument in a desired direction, given that the instrument is fixed in the body frame. In a pointing application, rotations about the pointing direction are irrelevant; a reduced-attitude representation can be used instead. The pointing direction of the instrument can be described by a vector $\boldsymbol{b}$ on the two-sphere, defined as $\mathbb{S}^2 = \{\boldsymbol{x} \in \mathbb{R}^3 \,|\, ||\boldsymbol{x}|| = 1\}$. Assume that the body-fixed frame is aligned with the principal axes of the spacecraft and that the pointing vector $\boldsymbol{b}$ is aligned with the one of the body-frame axes. Without loss of generality, consider $\boldsymbol{b}$ to be aligned with the third principal axis, i.e., expressed in the body-fixed frame, $\boldsymbol{b} = [0 \quad 0 \quad 1]^T$. In the inertial frame, $\boldsymbol{\Gamma} = \boldsymbol{R}\boldsymbol{b} \in \mathbb{S}^2$ represents the pointing direction of the vector $\boldsymbol{b}$. Because $\boldsymbol{\Gamma}$ is invariant to rotations about $\boldsymbol{b}_3$, it is a reduced-attitude representation of the orientation of the spacecraft [67]. The use of the nonlinear $\mathbb{S}^2$ manifold motivates the use of nonlinear analysis and control design.

4.3.1 Error States for Reduced Attitude Control

A function Ψ that defines the pointing error between the spacecraft $\boldsymbol{b}$ and the desired pointing direction $\boldsymbol{R}^T\boldsymbol{r}_d$ is [72]

$$\Psi = 1 - \boldsymbol{b} \cdot \boldsymbol{R}^T\boldsymbol{r}_d, \tag{4.31}$$

where $\boldsymbol{r}_d$ is the desired pointing direction in the inertial frame. The error function 4.31 can also be expressed as $1 - \cos\theta$, where θ is the angle between the unit vectors $\boldsymbol{b}$ and $\boldsymbol{R}^T\boldsymbol{r}_d$. The error function is positive definite and has critical points occurring at $\theta = \pm\pi$, [72].

Define the pointing error vector as

$$\boldsymbol{e}_r = \boldsymbol{R}^T \boldsymbol{r}_d \times \boldsymbol{b}. \tag{4.32}$$

The error vector 4.32 can be interpreted as a gradient vector field on $\mathbb{S}^2$ induced by the potential function Ψ; $\boldsymbol{e}_r$ vanishes at the critical points of Ψ [72].

Define the angular velocity error as

$$\boldsymbol{e}_\omega = \boldsymbol{\omega} - \boldsymbol{R}^T \boldsymbol{\Omega}_d, \tag{4.33}$$

where $\boldsymbol{\Omega}_d$ is the desired angular velocity of the spacecraft in the inertial frame and $\boldsymbol{\omega}_d = \boldsymbol{R}^T \boldsymbol{\Omega}_d$ is the angular velocity of the spacecraft expressed in the body frame.

The dynamics of the pointing error are computed by taking the derivative of Ψ, which yields

$$\dot{\Psi} = 0 - \boldsymbol{b}^T \left(\dot{\boldsymbol{R}}^T \boldsymbol{r}_d + \boldsymbol{R}^T \dot{\boldsymbol{r}}_d \right) = -\boldsymbol{b}^T \left(-\boldsymbol{\omega}^\times \boldsymbol{R}^T \boldsymbol{r}_d + \boldsymbol{R}^T (\boldsymbol{\Omega}_d \times \boldsymbol{r}_d) \right). \tag{4.34}$$

Taking advantage of the triple product identity $\boldsymbol{a} \cdot (\boldsymbol{b} \times \boldsymbol{c}) = \boldsymbol{b} \cdot (\boldsymbol{c} \times \boldsymbol{a}) = \boldsymbol{c} \cdot (\boldsymbol{a} \times \boldsymbol{b})$ and rearranging Eq. (4.34) yields

$$\dot{\Psi} = (\boldsymbol{R}^T \boldsymbol{r}_d \times \boldsymbol{b}) \cdot (\boldsymbol{\omega} - \boldsymbol{R}^T \boldsymbol{\Omega}_d) = \boldsymbol{e}_\omega^T \boldsymbol{e}_r, \tag{4.35}$$

which conveniently contains $\boldsymbol{e}_r$ and $\boldsymbol{e}_w$.

The dynamics of the angular velocity error are computed by taking the derivative of $\boldsymbol{e}_\omega$ as follows:

$$\dot{\boldsymbol{e}}_\omega = \dot{\boldsymbol{\omega}} - \dot{\boldsymbol{R}}^T \boldsymbol{\Omega}_d - \boldsymbol{R}^T \dot{\boldsymbol{\Omega}}_d = \dot{\boldsymbol{\omega}} + \boldsymbol{\omega}^\times \boldsymbol{R}^T \boldsymbol{\Omega}_d - \boldsymbol{R}^T \dot{\boldsymbol{\Omega}}_d = \dot{\boldsymbol{\omega}} + \boldsymbol{\omega} \times \boldsymbol{\omega}_d - \dot{\boldsymbol{\omega}}_d. \tag{4.36}$$

The objective of a control law is to drive both error states, Ψ and $\boldsymbol{e}_\omega$, to zero.

4.3.2 Lyapunov-Based Control Design

The angular velocity of the spacecraft about the pointing vector $\boldsymbol{b}$ does not affect the kinematics of the reduced attitude representation. Therefore consideration of only the angular velocity orthogonal to $\boldsymbol{b}$ is required track a pointing angle reference because the reduced-attitude representation is invariant to rotations about itself. The projection of a vector $\boldsymbol{a}$ onto another vector $\boldsymbol{b}$, $\text{proj}_{\boldsymbol{b}}\boldsymbol{a}$, can be expressed in matrix form as $\Pi_{||}(\boldsymbol{b})\boldsymbol{a}$, where

$$\Pi_{||}(\boldsymbol{b}) = \boldsymbol{b}\boldsymbol{b}^T \tag{4.37}$$

The orthogonal projection of a vector in $\mathbb{R}^3$ can be expressed in matrix form as

$$\Pi_{\perp}(\boldsymbol{b}) = \boldsymbol{I}_3 - \Pi_{||}(\boldsymbol{b}) = \boldsymbol{I}_3 - \boldsymbol{b}\boldsymbol{b}^T. \tag{4.38}$$

The angular velocity error orthogonal to $\boldsymbol{b}$ can then be expressed as

$$\boldsymbol{e}_{\omega\perp} = \Pi_{\perp}\boldsymbol{e}_{\omega}. \tag{4.39}$$

The projection matrices about the pointing vector $\boldsymbol{b}$ will be denoted as $\Pi_{||}$ and $\Pi_{\perp}$ for simplicity.

Assume that the attitude dynamics occur on a significantly faster time scale than the orbital dynamics and so variations of the local magnetic field due to translation are neglected (an assumption commonly made in analysis of the B-dot algorithm [53]), therefore $\boldsymbol{B}$ in the inertial reference frame is assumed to be constant. Assume also that the local magnitude field is never exactly orthogonal to $\boldsymbol{b}$, i.e., $B_3 \neq 0$. A common spacecraft pointing objective is to orient a sensor or other instrument directly towards the body that it is orbiting (e.g., an Earth-imaging spacecraft). In these applications, for the instrument to remain correctly aligned, the desired angular velocity of the spacecraft must be equal to the angular velocity of its orbit and, for circular orbits, that angular velocity is constant. Therefore, assume that the angular velocity reference remains constant, i.e., $\dot{\Omega}_d = 0$.

Consider the following sum of the pointing angle error and the angular velocity error orthogonal to the pointing vector as a candidate Lyapunov function:

$$V = k_p\Psi + T = k_p(1 - \boldsymbol{b}^T\boldsymbol{R}^T\boldsymbol{r}_d) + \frac{1}{2}\boldsymbol{e}_{\omega\perp}^T J\boldsymbol{e}_{\omega\perp}, \tag{4.40}$$

Taking the derivative of the candidate Lyapunov function V yields

$$\dot{V} = k_p\boldsymbol{e}_{\omega\perp}^T\boldsymbol{e}_r + \boldsymbol{e}_{\omega\perp}^T J\dot{\boldsymbol{e}}_{\omega\perp} = k_p\boldsymbol{e}_{\omega\perp}^T\boldsymbol{e}_r + \boldsymbol{e}_{\omega\perp}^T J\left(\Pi_\perp\left[J^{-1}(\boldsymbol{\omega}\times J\boldsymbol{\omega} + J^{-1}\boldsymbol{\tau} - \boldsymbol{\omega}\times\boldsymbol{\omega}_d\right]\right). \tag{4.41}$$

Under the assumptions stated in Section 4.3, the matrices J and $\Pi_\perp$ commute, thus

$$\dot{V} = k_p\boldsymbol{e}_{\omega\perp}^T\boldsymbol{e}_r + \boldsymbol{e}_{\omega\perp}^T J\dot{\boldsymbol{e}}_{\omega\perp} = k_p\boldsymbol{e}_{\omega\perp}^T\boldsymbol{e}_r + \boldsymbol{e}_{\omega\perp}^T\Pi_\perp\left[\boldsymbol{\omega}\times J\boldsymbol{\omega} + \boldsymbol{\tau} - J\boldsymbol{\omega}\times\boldsymbol{\omega}_d\right] \tag{4.42}$$

Substituting $\boldsymbol{\omega}_d = \boldsymbol{\omega} - \boldsymbol{e}_\omega$ and utilizing the identity $\boldsymbol{a}\cdot(\boldsymbol{b}\times\boldsymbol{c}) = \boldsymbol{b}\cdot(\boldsymbol{c}\times\boldsymbol{a}) = \boldsymbol{c}\cdot(\boldsymbol{a}\times\boldsymbol{b})$, the expression Eq. (4.42) becomes

$$\dot{V} = k_p\boldsymbol{e}_{\omega\perp}^T\boldsymbol{e}_r + \boldsymbol{e}_{\omega\perp}^T\boldsymbol{\tau} + \boldsymbol{e}_\omega^T(J\boldsymbol{e}_{\omega\perp}\times\boldsymbol{\omega}) + \boldsymbol{e}_{\omega\perp}^T\times(\boldsymbol{\omega}\times J\boldsymbol{\omega}). \tag{4.43}$$

Consider the following control input to the magnetic torque rods:

$$\boldsymbol{m} = \Pi_\parallel\frac{1}{\boldsymbol{B}}\times\left(-k_p\boldsymbol{e}_r - \boldsymbol{\omega}\times J\boldsymbol{\omega} - \Pi_\perp J\boldsymbol{\omega}^\times\boldsymbol{e}_\omega\right) - k_\omega\Pi_\perp(\boldsymbol{B}\times\Pi_\perp\boldsymbol{e}_\omega). \tag{4.44}$$

Note that because the first term is a cross product with a vector parallel to $\boldsymbol{b}$ and the second term is an orthogonal projection relative to $\boldsymbol{b}$, this expression yields a vector orthogonal to $\boldsymbol{b}$. In the body frame, there are nonzero entries corresponding to the directions of the magnetic torque rods and a zero entry corresponding to the direction of $\boldsymbol{b}$. Therefore, $\boldsymbol{m}$ represents a valid expression for the specified control input model. Substituting the torque resulting from the control input in

Eq. (4.44) $\boldsymbol{\tau} = \boldsymbol{m} \times \boldsymbol{B}$ into Eq. (4.43) yields

$$\dot{V} = -k_w B_3^2 \|\boldsymbol{e}_{\omega\perp}\|^2 \leq 0 \quad \dot{V} = 0 \quad \text{iff} \quad \|\boldsymbol{e}_{\omega\perp}\| = 0. \tag{4.45}$$

Therefore, the proposed control law asymptotically drives the pointing error and angular velocity error orthogonal to the pointing vector to zero for any constantly-varying pointing reference.

4.3.3 Simulation Results

Numerical simulations illustrate the performance of the closed-loop system. A rigid spacecraft is simulated in a circular orbit around Earth. The orbit with the initial true anomaly is specified in Table C.4 The initial conditions of attitude and angular velocity used for the numerical simulation are

$$\boldsymbol{R}_0 = \mathbb{I}^{3\times 3}, \quad \boldsymbol{\omega}_0 = \begin{bmatrix} 4 & -5 & 2 \end{bmatrix}^T \times 10^{-3}$$

with a mass of $5kg$ and a moment of inertia matrix of

$$J = \text{diag}\begin{bmatrix} 0.25 & 0.25 & 0.4 \end{bmatrix}$$

The magnetic field is modeled as in Section 2.1.3 and the control authority available to the magnetic torque rods varies with orbital position. The gains used in the controller are $k_p = 5 \times 10^{-5}$, and $k_w = 0.1$.

The reference attitude trajectory supplied to the controller is a nadir-pointing attitude, i.e., pointing towards the Earth's center $\boldsymbol{r}_d = \boldsymbol{r}/\|\boldsymbol{r}\|$, with the reference angular velocity $\boldsymbol{\Omega}_d$ as the angular velocity of the spacecraft's orbit. The given initial conditions require a slewing maneuver to align with the reference attitude at the correct angular velocity. The results of the simulation are plotted below.

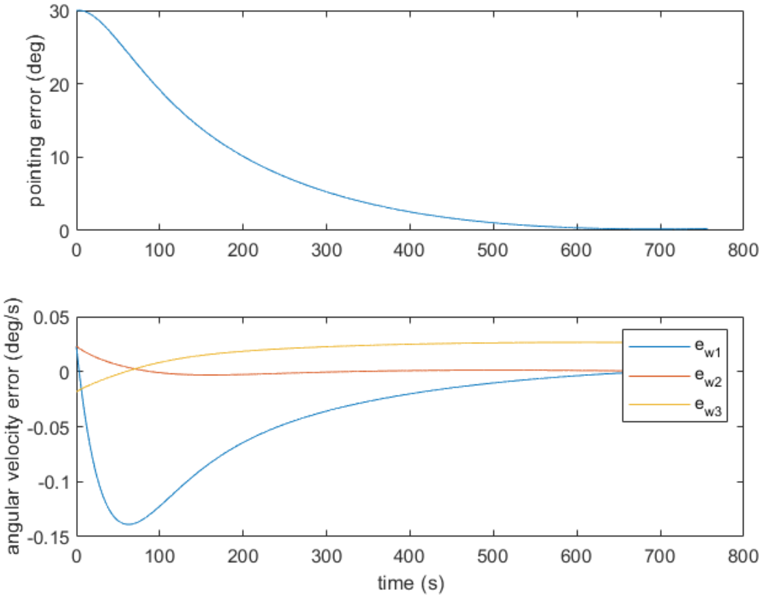

Figure 4.2: Magnitude of the pointing error and angular velocity error over a 750-second simulation. The error of the pointing angle and the angular velocity error orthogonal to the pointing vector both converge to zero.

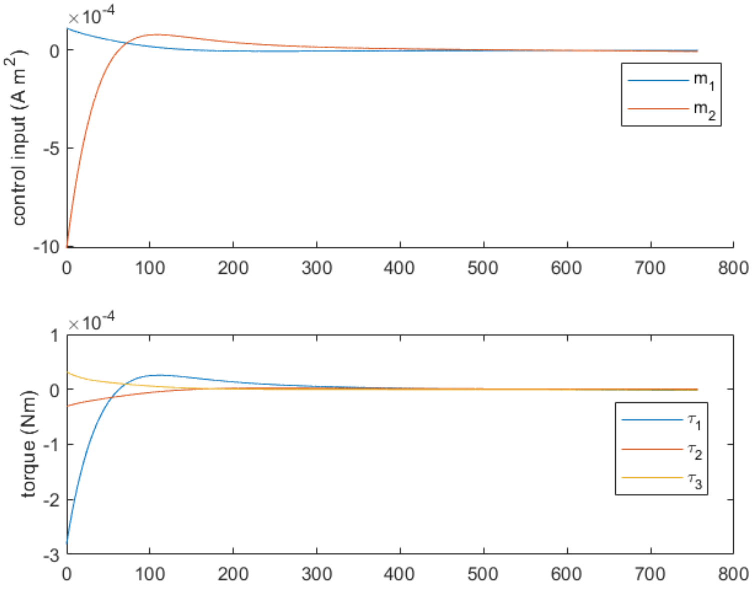

Figure 4.3: Control inputs and resulting torques over a 750-second simulation. The actuation torque is on the order of tenths of millinewton meters, which is a magnitude realistic to magnetic torque rods.

Simulation results demonstrate the asymptotic convergence of the error states representing pointing error and angular velocity error orthogonal to the pointing vector to zero. Note that there is some residual angular velocity about the pointing vector, which is akin to a nadir-pointing spacecraft that is rotating about its pointing axis. This outcome is expected because, with only two magnetic torque rods, full attitude stabilization is not possible. However, when the other error states have converged to zero, this residual angular velocity does not affect the pointing angle or its kinematics. Note also that because the magnetic field in the simulation is taken as a function of the spacecraft's position relative to Earth, the simulation suggests that the controller still stabilizes the closed-loop system even when relaxing the assumption of a constant magnetic field.

An additional simulation was performed with a larger initial angular velocity to represent the scenario of detumbling the spacecraft and then aligning it in the desired direction. The same parameters were used except the initial angular velocity, which is now set as $\boldsymbol{\omega}_0 = [-3 \quad -4 \quad 2]^T \times 10^{-2}$. The resulting simulations are shown below.

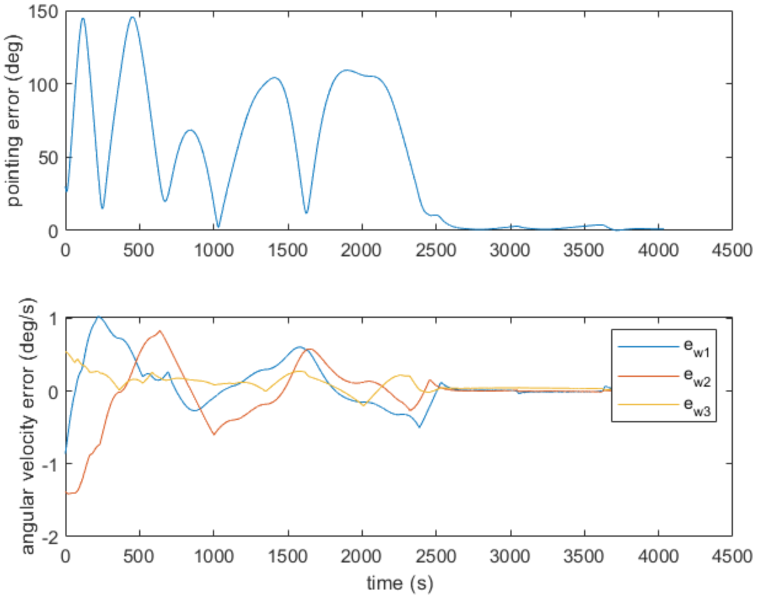

Figure 4.4: Magnitude of the pointing error and angular velocity error over a detumbling simulation. The error of the pointing angle and the angular velocity error orthogonal to the pointing vector both converge to zero.

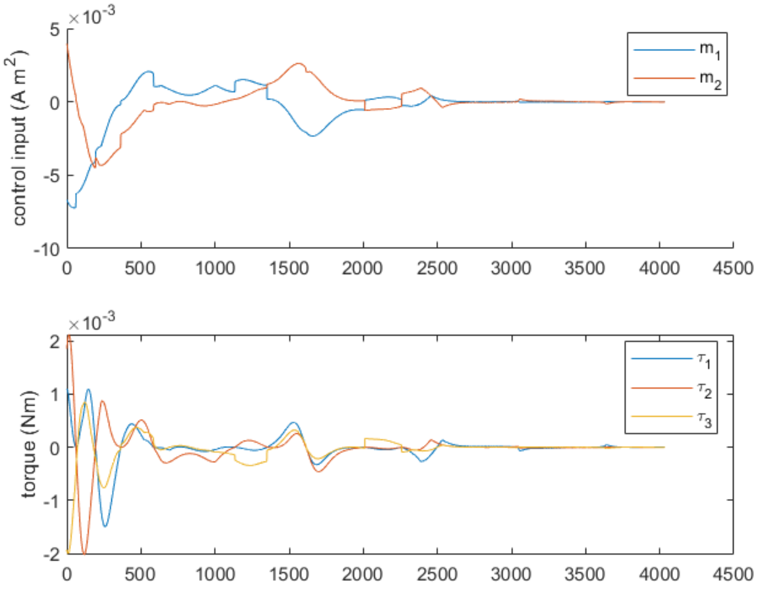

Figure 4.5: Control inputs and resulting torques over a 4000-second detumbling simulation. The torque developed by the magnetic torque rods is on the order of millinewton meters.

The simulation results demonstrate controller performance from a more demanding initial condition. Although it takes longer, the simulation shows that the controller does eventually remove enough rotational energy from the spacecraft to then successfully track the desired reference.

Finally, a simulation was performed where the control input is saturated as shown in Eq. (4.29) and with a demanding initial condition to ensure that that the control law still performs with the added constraint. The same parameters are used except the initial angular velocity, which is now set as $\boldsymbol{\omega}_0 = [0.2 \quad -0.25 \quad 0.1]^T$. The resulting simulations are shown below.

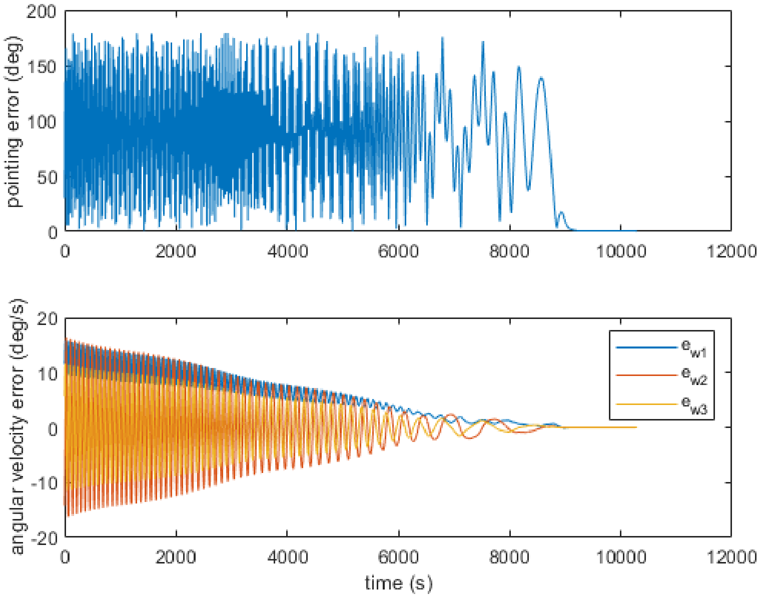

Figure 4.6: Magnitude of the pointing error and angular velocity error over a detumbling simulation with saturated control input. The error of the pointing angle and the angular velocity error orthogonal to the pointing vector both converge to zero.

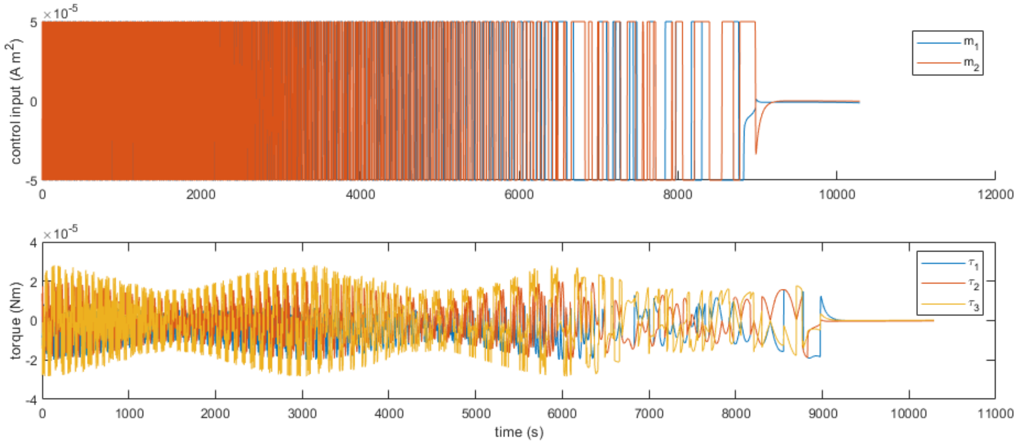

Figure 4.7: Control inputs and resulting torques over a detumbling simulation with saturated control input. The saturation of the inputs and the variation in output magnitude due to the local magnitude are visible

These simulations demonstrate that the attitude control law in Eq. (4.44) subject to saturation limits stabilizes the reduced attitude and angular velocity to a nadir reference despite an initial condition with very high rotational energy and a magnetic field varying with orbital position. Extending the theoretical analysis to demonstrate stability with the inclusion of saturation limits is the subject of ongoing work.

For shape control, the objective of aligning the $\hat{\boldsymbol{b}}_3^{(i)}$ axis of each panel with the $\hat{\boldsymbol{a}}_3$ axis of the hub is equivalent to the reduced attitude control problem, but with different references. With the analogous problem of controlling the reduced attitude of a single panel solved, the control law can be applied to the panels comprising the appendage for effective shape control.

4.4 State-Feedback Control of 3D Flexible Spacecraft Model

This section implements the derived magnetic torque rod control law to actuate the magnetic torque rod pairs attached to the panels in the flexible spacecraft model to achieve shape control. Simulations evaluate the effectiveness of the shape control in response to different types of disturbances, namely oscillations induced from performing an attitude maneuver, and shape deformations resulting from thermoelasticity.

Similar to the two-dimensional model, the control paradigm remains unchanged. The reaction wheels on the hub are employed to control the hub's attitude and angular velocity. The torque rods are used to maintain the appendage's flatness and to minimize structural vibrations.

Because the attitude of the hub is represented as a rotation matrix, a feedback controller using the full attitude R and angular velocity $\boldsymbol{\omega}$ is required. The controller used for the reaction wheels is taken from [67] which explores closed loop control on $SO(3)$. A control law to track a desired attitude R_d and angular velocity $\boldsymbol{\omega}_{C,\text{ref}}$ that uses a proportional derivative feedback control structure is given by [67]

$$u = -K_w \boldsymbol{e}_\omega - K_p \Omega_a(R_C) \tag{4.46}$$

where $\boldsymbol{e}_\omega = \boldsymbol{\omega}_C - \boldsymbol{\omega}_{\text{ref}}^{(C)}$, $K_\omega, K_p \in \mathcal{R}^{3x3}$ are positive definite matrices, $\boldsymbol{a} = [a_1 \; a_2 \; a_3]^T$ where $a_1, a_2,$ and a_3 are distinct positive integers and

$$\Omega_a(R_C) \triangleq \sum_{i=1}^{3} a_i e_i \times (R_d^T R e_i) \tag{4.47}$$

with $[e_1 \; e_2 \; e_3]^T$ the identity matrix.

For shape control, the torque rod control developed in Section 4.3 is used. Specifically Eq. (4.44) is taken as the control input with the saturation limits shown in Eq. (4.29) applied. Whereas in Section 4.3 the desired pointing direction $\boldsymbol{r}_d$ and angular velocity $\boldsymbol{\Omega}_d$ corresponded to a nadir-pointing reference, for shape control of the appendage, the reference pointing direction aligns with $\hat{\boldsymbol{a}}_3$ and the reference angular velocity is that of the hub. Specifically, the reduced attitude error for the ith panel is

$$\boldsymbol{e}_r^{(i)} = R_{B_i}^T R_C e_3 \times e_3, \tag{4.48}$$

and the angular velocity error is

$$\boldsymbol{e}_\omega^{(i)} = \boldsymbol{\omega}_i - R_{B_i}^T R_C \boldsymbol{\omega}_C. \tag{4.49}$$

To evaluate the impact of incorporating shape control, simulations are conducted with two different types of disturbances. First, the structural vibrations induced by an attitude maneuver are examined. Second, shape deformations resulting from thermoelastic effects are considered. A comparison between using reaction wheels for attitude control and the combined use of reaction wheels for attitude control and torque rods for shape stabilization is presented for each simulation.

In each set of simulations, the system is subjected to orbital effects. Specifically, the spacecraft experiences gravity gradient torque, and the magnetic field varies with orbital position, leading to fluctuations in control authority throughout an orbit. In each of the simulations the reference attitude and angular velocity is a nadir-pointing reference. The desired attitude is defined such that $\hat{\boldsymbol{a}}_3$ aligns with the vector from the center of the Earth to the spacecraft, $\hat{\boldsymbol{a}}_1$ is aligned with the local horizontal in the direction of orbital motion and $\hat{\boldsymbol{a}}_2 = \hat{\boldsymbol{a}}_3 \times \hat{\boldsymbol{a}}_1$, which is parallel with the angular momentum vector of the orbit. The orbit used for each simulation in this section is shown in Table C.5.

Because the considered orbit is circular, the reference attitude for the hub can be defined using its state. The vector from nadir to the hub is simply its position $\boldsymbol{r}_{C/O}$, thus the desired direction for $\hat{\boldsymbol{a}}_3$ is $\boldsymbol{r}_{C/O}/\|\boldsymbol{r}_{C/O}\|$. For a circular orbit, the local horizontal is parallel with the spacecraft's velocity vector, thus the desired direction for $\hat{\boldsymbol{a}}_1$ is $\boldsymbol{v}_{C/O}/\|\boldsymbol{v}_{C/O}\|$ Therefore, R_d is defined as

$$R_d = \left[\frac{\boldsymbol{v}_{C/O}}{\|\boldsymbol{v}_{C/O}\|}, \quad \frac{\boldsymbol{r}_{C/O}}{\|\boldsymbol{r}_{C/O}\|} \times \frac{\boldsymbol{v}_{C/O}}{\|\boldsymbol{v}_{C/O}\|}, \quad \frac{\boldsymbol{r}_{C/O}}{\|\boldsymbol{r}_{C/O}\|}\right]. \tag{4.50}$$

The angular velocity reference is the angular velocity of the orbit in the direction of the orbit's angular momentum. In the inertial frame

$$\boldsymbol{\omega}_{\text{ref}}^{(C)} = R_{313}(\Omega, i, \omega) \begin{bmatrix} 0 & 0 & \sqrt{\mu/a^3} \end{bmatrix}^T \tag{4.51}$$

where R_{313} is a 3-1-3 rotation matrix parametrized by the orbital parameters right ascension of the ascending node (Ω), inclination (i), and argument of periapsis (ω) that rotates from the perifocal frame to the Earth-centered inertial frame.

The spacecraft model used for the simulations has a 15 meters by 15 meter flexible appendage discretized into a 6x6 grid depicted in Fig. 4.1 with the physical parameters shown in

Table C.6.

To evaluate the performance in attitude control, the attitude and angular velocity of hub relative to the reference is measured. The attitude error of the hub ε_{R_C} is defined as the angular distance between its attitude and the reference

$$\varepsilon_{R_C} = \cos^{-1} \frac{\mathrm{Tr}(R_d^T R_C) - 1}{2} \tag{4.52}$$

The hub's angular velocity error ε_{ω_C} is defined as the magnitude of the angular velocity error vector.

$$\varepsilon_{\omega_C} = \|\boldsymbol{\omega}_C - \boldsymbol{\omega}_{\text{ref}}^{(C)}\| \tag{4.53}$$

To evaluate the performance in shape control, appendage flexures are characterized via two panel measurements. The first is the deviation in pointing angle of panels relative to the hub. This metric denoted $\varepsilon_{R_{B_i}}^{(i)}$ for the ith panel measures the rotation between the axes $\hat{\boldsymbol{a}}_3$ and $\hat{\boldsymbol{b}}_3^{(i)}$ and is zero when the panel is flat relative to the hub:

$$\varepsilon_{R_{B_i}}^{(i)} = \cos^{-1} \left(R_{B_i}^T R_C e_3 \cdot e_3 \right) . \tag{4.54}$$

The second metric $\varepsilon_{e_3}^{(i)}$ is the displacement of panels in the $\hat{\boldsymbol{a}}_3$ direction characterizing how far a panel is displaced from the flat configuration relative to the hub:

$$\varepsilon_{e_3}^{(i)} = |\boldsymbol{r}_{i/C} \cdot e_3| \tag{4.55}$$

To characterize the entire appendage, the mean and maximum values over all panels for each of these metrics are calculated. The mean provides an indication of the overall flatness of the entire appendage, while the maximum value highlights the most significant deviations that exist. To understand the effects of the moments generated by the torque rods on the attitude controller, the control inputs and the total angular momentum stored by the reaction wheels as they are actuated are also considered.

4.4.1 Maneuver-Induced Oscillation

The first disturbance investigated is the structural vibration of the appendage resulting from the moment generated by the reaction wheels. This moment excites the flexible modes of the appendage resulting in structural oscillation. To examine the impact of shape control via the magnetic torque rods, an initial value problem is formulated. In this scenario, the initial attitude of the hub is set some angle off nadir. The attitude control then drives the system towards a nadir-pointing reference, introducing structural oscillation. This scenario simulates an attitude maneuver performed in orbit, where the spacecraft switches attitude references, such as from aligning with the sun to a nadir-pointing reference.

The initial attitude of the hub is 16 degrees off nadir, with the initial angular velocity matching the angular velocity of the orbit. The appendage is initially at equilibrium, meaning it is flat and stationary relative to the hub. The control parameters used in this simulation are shown in Table C.7.

The results of the initial value problem simulation are shown below. For the hub, the attitude error ε_{R_C} and angular velocity error ε_{ω_C} are shown in Fig. 4.8. The appendage flatness metrics ($\varepsilon_{R_{B_i}}^{(i)}$ and $\varepsilon_{e_3}^{(i)}$) are shown in Fig. 4.9. The control inputs and total accumulation of angular momentum stored in the reaction wheels are shown in Fig. 4.10.

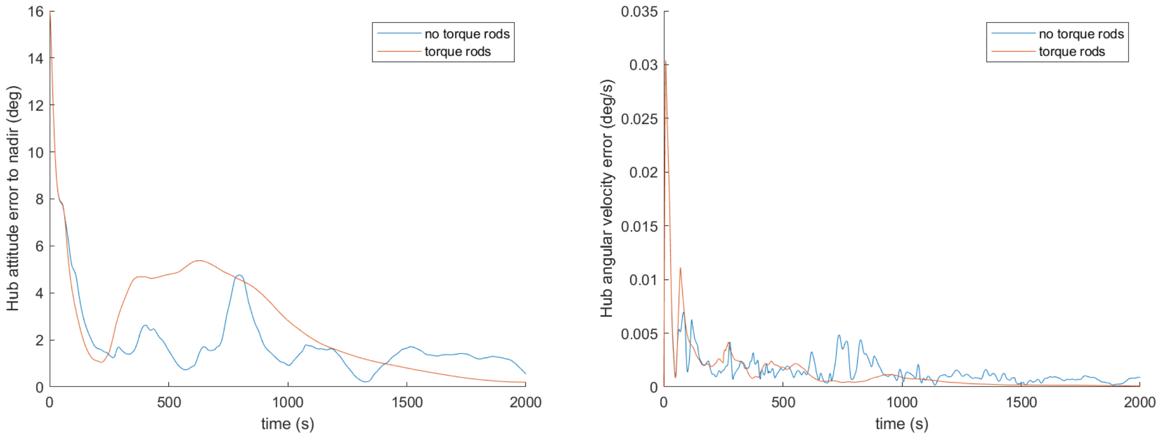

(a) Hub attitude error

(b) Hub angular velocity error

Figure 4.8: Comparison of the attitude control performance of an attitude maneuver simulation with and without the torque rod control. (a) the hub attitude error and (b) the hub angular velocity error. The torque rods improve attitude control performance

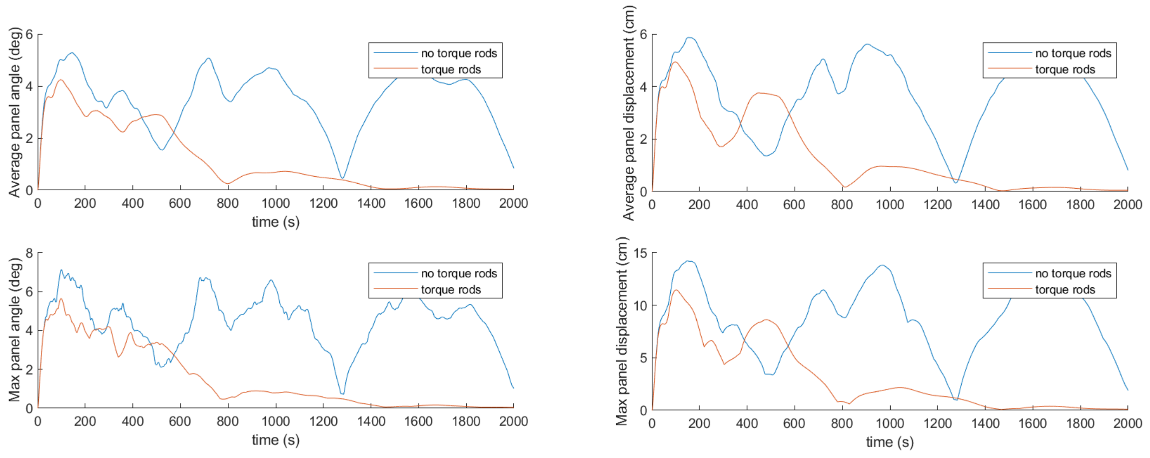

(a) Panel angular offset

(b) Panel displacement

Figure 4.9: Comparison of appendage flatness during an attitude maneuver simulation with and without shape control. Average and maximum (a) panel angle relative to hub and (b) panel displacement. Torque rods dampen oscillations and restore flatness.

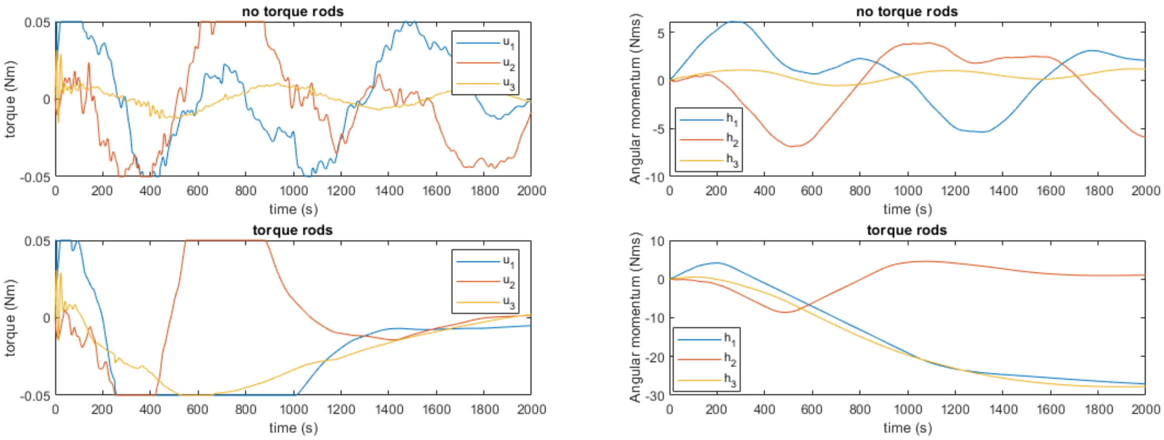

(a) Reaction wheel input

(b) Reaction wheel angular momentum

Figure 4.10: Comparison of control input and angular momentum accumulation of reaction wheels during an attitude maneuver simulation. (a) Control inputs to each reaction wheel. (b) Accumulation of reaction wheel angular momentum. The reaction wheels must accumulate additional angular momentum to maintain the desired attitude and angular velocity reference due to the moment generated by the torque rods for shape control.

Simulations show that using the torque rods to perform shape control significantly improves controller performance during an attitude maneuver. Fig. 4.8 illustrates that the attitude controller converges faster and with fewer vibrations when shape control is implemented compared to when it is not. This improvement is due to shape control reducing appendage bending, thereby causing less disturbance to the hub and enabling better performance by the attitude controller. Fig. 4.9 shows that the shape controller significantly reduces appendage deformations during an attitude maneuver. During the first 600 seconds of the simulation, the vibrations are damped, and by approximately 1400 seconds, the appendage converges to a flat configuration. Without shape control, the appendage continues to oscillate significantly after 1400 seconds, with average deformations of up 5 degrees offset and 6 cm of displacement, and maximum deformations of up to 6 degrees offset and 13 cm of displacement.

Fig. 4.10 illustrates the effect of the cumulative moment induced on the spacecraft by the torque rods over time. As the appendage oscillates, the reaction wheels generate a counteracting moment. Without shape stabilization, this counteracting moment changes direction along with the appendage deformation resulting in the accumulation of angular momentum due to oscillation generally averaging out. In contrast, with shape stabilization, each pair of torque rods exerts a moment that slightly influences the spacecraft's attitude. The reaction wheels must counteract these moments to maintain the desired attitude reference, leading to a higher accumulation of angular momentum in the reaction wheels during maneuvers. With the torque rods, the attitude maneuver necessitates approximately 25 Nms of angular momentum from the 1st and 3rd reaction wheels, whereas without them, it requires significantly less.

4.4.2 Thermoelastic Bending

The second disturbance investigated is shape deformations resulting from thermoelastic effects. As the spacecraft orbits the Earth, various parts of the spacecraft will intermittently face the sun. When one face of the appendage is exposed to sunlight, it heats up more than the opposite side, creating a significant temperature gradient. The heating causes thermal expansion and the temperature differential induces mechanical stress, leading to structural bending. In this case, the objective of shape control is to mitigate this bending and keep the appendage as flat as possible.

The discretization of the appendage provides a convenient way to model thermoelasticity. To model the thermal induced bending, the equilibrium angle of the hinge between each panel is varied. Let ϵ be a parameter that quantifies the degree of bending and $\boldsymbol{\epsilon}$ be a vector with magnitude ϵ that represents the difference in hinge equilibrium. For panels joined along the $\hat{\boldsymbol{a}}_1$ axis,

$$\boldsymbol{\epsilon}_{i,j} = \pm \begin{bmatrix} 0 \\ \epsilon \\ 0 \end{bmatrix}, \tag{4.56}$$

where $\boldsymbol{\epsilon}$ is positive if j is in the positive $\hat{\boldsymbol{a}}_1$ direction relative to i and negative otherwise. For panels joined along the $\hat{\boldsymbol{a}}_2$ axis,

$$\boldsymbol{\epsilon}_{i,j} = \pm \begin{bmatrix} \epsilon \\ 0 \\ 0 \end{bmatrix}, \tag{4.57}$$

where $\boldsymbol{\epsilon}$ is positive if j is in the positive $\hat{\boldsymbol{a}}_2$ direction relative to i and negative otherwise. The moment between panels i and j becomes

$$\mathbf{M}_{i,j} = -k_t(\theta \boldsymbol{\xi}_{i,j} + \boldsymbol{\epsilon}_{i,j}) - c_t \boldsymbol{\omega}_{i,j}. \tag{4.58}$$

Assume that rate at which the incidence of the sun on the spacecraft changes periodically with the orbit. Assume also that the incidence of the sun determines the rate of change of ϵ. The evolution of ϵ over time can then be approximated as a function of the true anomaly of the orbit

$$\dot{\epsilon} = A \sin \nu, \tag{4.59}$$

where A encapsulates the factors that determine the magnitude of thermal deformation. ϵ is added as a state to the system and integrated according to Eq. (4.59).

For the thermal deformation simulations, the initial condition of the spacecraft is its reference configuration. Specifically the hub is in a nadir-pointing reference and the appendage is flat and stationary relative to the hub. The initial condition for ϵ is 0 and the value of A is 2.7×10^{-5}. The control parameters in Table C.7 are used.

For illustration, the bending parameter over several orbital periods is plotted in Fig. 4.11. The appendage flatness metrics are shown in Fig. 4.12, and the control inputs and total accumulation of angular momentum stored in the reaction wheels are shown in Fig. 4.13a.

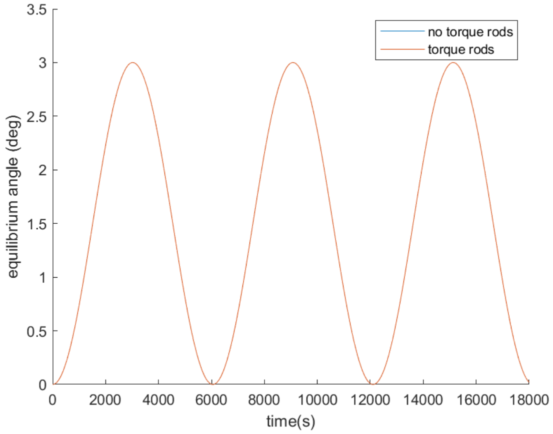

Figure 4.11: Panel interface equilibrium angle over three orbital periods

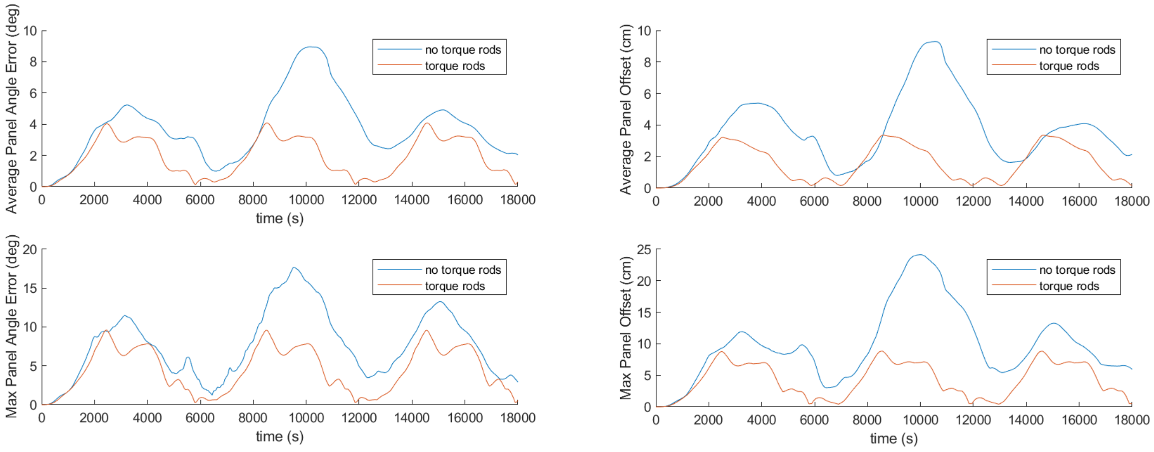

(a) Panel angular offset

(b) Panel displacement

Figure 4.12: Effects of torque rods in mitigating thermal deformations of the appendage. (a) Average and maximum panel angle relative to hub and (b) average and maximum panel displacement. The torque rods significantly reduce the magnitude of structural deformation.

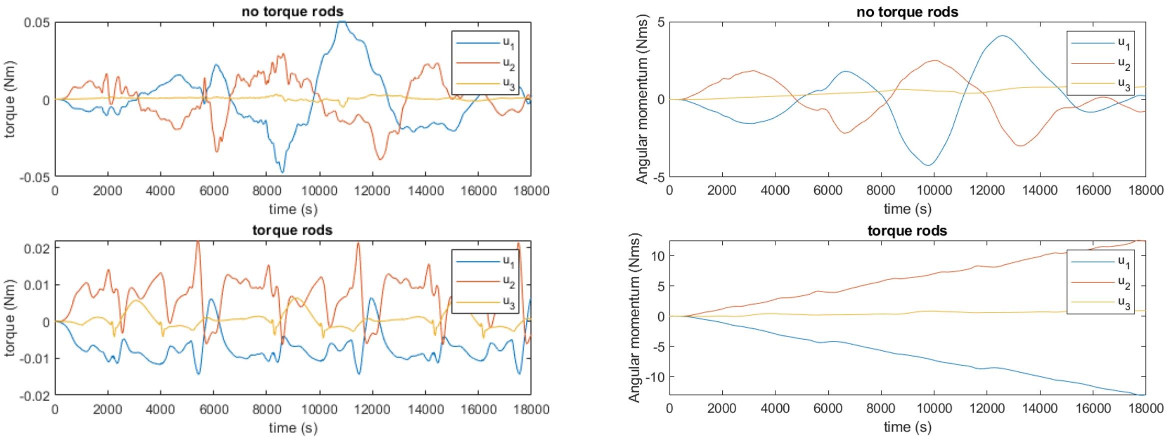

(a) Reaction wheel input

(b) Reaction wheel angular momentum

Figure 4.13: Control input and angular momentum accumulation of reaction wheels due to thermal deformations. (a) Control inputs to each reaction wheel and (b) the accumulation of reaction wheel angular momentum. The reaction wheels require taking on additional angular momentum to maintain the desired attitude and angular velocity reference due to the moment generated by the torque rods.

Simulations show that the shape-stabilizing controller counteracts the effects of thermal deformation. Fig. 4.9 illustrates the effect that the torque rods have on the appendage flatness. Over the three orbital periods, the use of torque rods reduces the average and maximum angular deviation of the panels uniformly. When ϵ is at its highest, the effect is more pronounced with maximum displacements being reduced from nearly 25 cm to less than 10 cm. The torque rods are unable to maintain perfect flatness with the parameters used in the simulation. This is because torque rods can only produce a very small amount of torque, insufficient to overcome the stiffness of the structure. In reality, the structure would need to have almost no rigidity for the magnetic torque rods to maintain perfect flatness. However, despite not maintaining perfect flatness, the benefit they provide is still significant.

The reduction in shape deformation, however, comes at the cost of the reaction wheels accumulating angular momentum to counteract the torque generated by the torque rods, as illustrated by Fig. 4.10b. Without shape control, the angular momentum introduced into the system is minimal, resulting in a small net angular momentum stored in the reaction wheels to maintain the attitude reference. In contrast, with shape stabilization, the reaction wheels must store approximately 4 Nms of angular momentum per orbit along the $\hat{\boldsymbol{a}}_1$ and $\hat{\boldsymbol{a}}_2$ axes to maintain the attitude reference.

4.4.3 Parameter Study

To assess a more generalized impact of shape-stabilizing control, a parameter study was conducted to investigate how the torque rods influence the system across a range of torsional spring and damping coefficients, which determine the flexibility and behavior of the appendage. For the given spacecraft design, maintaining consistent parameters except for the spring constant k_t and damping coefficient c_t, an angular impulse is applied to the spacecraft and the system response is simulated for 1000 seconds. The torque rods are then activated to dampen the vibrations from the flexible appendage and stabilize it to a flat shape. In each simulation, the average displacement magnitude of the panels, averaged over time, was calculated to quantify the flatness of the appendage over the simulation. For every simulation, a spring and damping coefficient pair is selected from a sample space, and the system's response, with and without the torque rods, is simulated and the metric computed. The results are shown in Fig. 4.14.

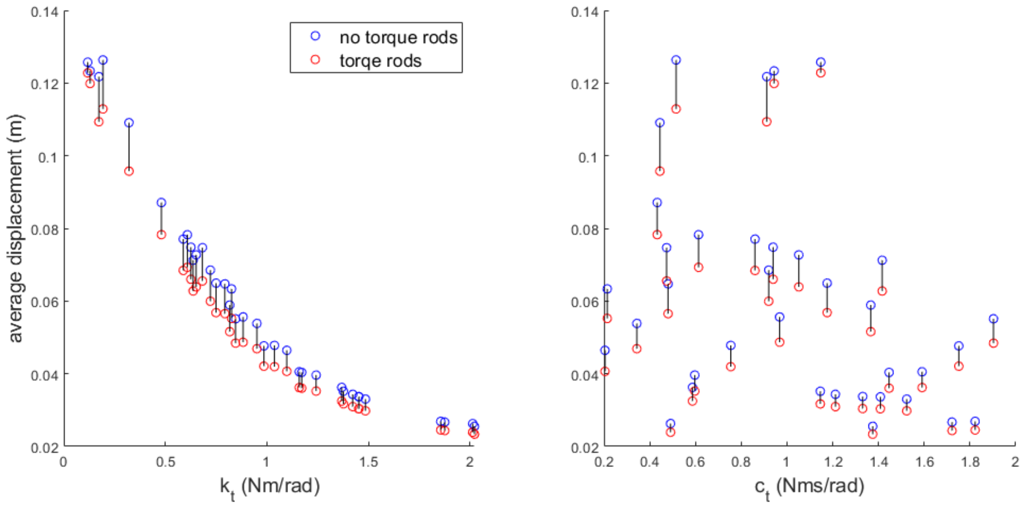

Figure 4.14: Average displacement of the panels comprising the appendage over a 1000 second impulse response simulation of differing levels of flexibility and damping of the appendage.

Simulations indicate that across the examined parameter space, the shape-stabilizing control uniformly leads to reduced overall deformation of the appendage. The results in Fig. 4.14 also indicate a correlation in the magnitude of impact that the torque rods have on shape stabilization. For lower spring coefficients, the difference in displacement is larger, suggesting that the torque rods appear have a larger affect on performance for less rigid structures. This makes intuitive sense because a stiffer system would deform less and require less help from the controller to return to its natural configuration. There does not appear to be a similar correlation for the damping coefficient. The outcome of this parameter study suggests that the shape-stabilizing control is generally effective for spacecraft of this design, even for structures with varying flexibility properties.

4.5 Conclusion

This chapter addresses the use of distributed pairs of magnetic torque rods across a flexible spacecraft structure to regulate its shape. A three-dimensional dynamic spacecraft model consisting of a hub and flexible appendage modeled by a discretized series of flexibly connected rigid elements is proposed. The hub is actuated by a set of reaction wheels and each element (panel) is actuated by a magnetic torque rod pair. To develop a control law for a magnetic torque rod pair, control of the reduced attitude of a single panel is considered. The panel considered separately could also be thought of as its own spacecraft actuated by two magnetic torque rods. To achieve this objective, a novel control law is proposed and analyzed using Lyapunov analysis. The theoretical analysis suggests that the proposed control law effectively stabilizes the reduced attitude and angular velocity of a rigid spacecraft using only two magnetic torque rods. Numerical simulations are conducted to validate the performance of the proposed control law. The results of these simulations demonstrate that the proposed control law successfully stabilizes the defined error states. Although developed for shape control of a flexible appendage, the control law has applicability to the field of smallscale satellites such as a CubeSat.

The magnetic torque rod control law is applied to the three-dimensional spacecraft model to implement shape control of a flexible appendage. Simulations are conducted under two different types of disturbances: attitude maneuvers that induce structural oscillations and shape deformations caused by periodic solar heating. The implementation of shape stabilization using distributed pairs of torque rods throughout the appendage significantly dampens oscillations and mitigates deformations under both disturbances and over a wide parameter space. This has several important implications.

First, a flexible spacecraft structure, such as an antenna, may only be functional if deformations are limited within a certain range. Second, if the speed of attitude maneuvers is constrained to prevent excitation of a flexible appendage, there may be a loss of mission time due to the additional time required for maneuvers. Consequently, the reduction in deformation provided by the torque rods could render an otherwise infeasible design feasible.

However, the cost of shape stabilization is that the reaction wheels on the hub accumulate additional angular momentum to counteract the moment generated by the torque rods. Since reaction wheels have a finite capacity for storing angular momentum before needing to offload, this would result in the spacecraft spending more time over its lifespan dumping momentum from the reaction wheels.

Chapter 5: State Estimation of Flexible Spacecraft

5.1 Introduction

This chapter addresses state estimation of the flexible spacecraft model in Section 4.2. The control law presented in Section 4.4 requires knowledge of the state of each panel comprising the appendage. In practice, only a limited set of measurements is available, necessitating the estimation of the system's state for the control law to be applied. Given the computational challenges of state estimation for high-dimensional nonlinear systems and the limited computational resources onboard a spacecraft, model reduction is explored.

To obtain a linear reduced-order model from a high-dimensional nonlinear system, dynamic mode decomposition (DMD) originating from the field of fluid dynamics is applied to the flexible spacecraft model. The most significant mode shapes are identified. The error resulting from using a reduced-order model is computed for varying numbers of modes, considering both finer and coarser discretizations of the flexible appendage. The DMD Kalman filter is then applied to perform state estimation of mode amplitudes using limited measurements, and the quality of the resulting state estimates is evaluated. The linearized representation of the mode amplitudes' evolution and the DMD modes provide a measure of observability for a given set of state measurements. This measure is used to optimize the number and placement of sensors to maximize observability.

The contributions of this chapter are as follows: (1) the application of dynamic mode decomposition to the flexible spacecraft model to produce a reduced-order representation; (2) using the reduced order model to enable full state estimation with a limited set of measurements; and (3) optimization of the number and placement of sensors to maximize observability for state estimation.

This chapter is organized as follows. Section 5.2 applies dynamic mode decomposition to the flexible spacecraft model and investigates the resulting modes. Section 5.3 uses the DMD Kalman filter to perform state estimation of the dynamic model and investigates the performance of the state estimator. Section 5.4 describes the framework for optimizing sensor number and placement to maximize observability of the mode amplitudes. Section 5.5 provides a concluding summary of the chapter

5.2 Dynamic Mode Decomposition of Flexible Spacecraft Model

In this section, dynamic mode decomposition (DMD) is used to generate a modal decomposition of the flexible spacecraft model. The goal of the modal decomposition is to be able to estimate the attitude shape of the spacecraft. To decouple the spacecraft's attitude and shape dynamics from its translational dynamics, consider the term $\frac{\boldsymbol{F}_i}{m_i} - \frac{\boldsymbol{F}_C}{m_C}$ appearing in Eq. (4.10) for the translational dynamics for each panel. Substituting the total forces 4.25, 4.23 into this expression yields

$$\frac{\boldsymbol{F}_i}{m_i} - \frac{\boldsymbol{F}_C}{m_C} = -\mu\frac{\mathbf{r}_{i/O}}{\|\mathbf{r}_{i/O}\|^3} + \mu\frac{\mathbf{r}_{C/O}}{\|\mathbf{r}_{C/O}\|^3} + \frac{1}{m_i}\sum_{j\in\mathcal{N}_i}\boldsymbol{F}_{i,j} - \frac{1}{m_C}\boldsymbol{F}_{C,1}. \tag{5.1}$$

For a large spacecraft, the difference between $\mathbf{r}_{i/O}$ and $\mathbf{r}_{C/O}$ might be on the order of 10s of meters at most while their magnitude is on the order of thousands of kilometers. Consequently, the gravitational influence on each term differs minimally, allowing for the approximation $\mathbf{r}_{i/O} \approx \mathbf{r}_{C/O}$. As a result, the gravitational contributions cancel out in Eq. (5.1), i.e.,

$$\frac{\boldsymbol{F}_i}{m_i} - \frac{\boldsymbol{F}_C}{m_C} \approx \frac{1}{m_i} \sum_{j \in \mathcal{N}_i} \boldsymbol{F}_{i,j} - \frac{1}{m_C} \boldsymbol{F}_{C,1} \tag{5.2}$$

Any relative acceleration between panel i and the hub induced by the differing gravitational forces is negligible compared to the system's structural dynamics. With this approximation, the dynamics of the appendage no longer depend on the inertial position and velocity of the spacecraft. As a result, the attitude and shape of the flexible spacecraft can be written as a state-space system independent of the translational dynamics of the hub. The state of this reduced system is

$$\boldsymbol{\eta} = [R_C \quad \boldsymbol{\omega}_C \quad \boldsymbol{\eta}_1 \quad \boldsymbol{\eta}_2 \quad \dots \quad \boldsymbol{\eta}_N]^T \tag{5.3}$$

and its dynamics can be written entirely as a function of its state, i.e.,

$$\dot{\boldsymbol{\eta}} = \boldsymbol{f}(\eta). \tag{5.4}$$

5.2.1 Modal Decomposition

To perform DMD on the flexible spacecraft model, a training dataset is required. To generate training data, a time-varying control input profile is applied to the system via $\boldsymbol{u}_C(t)$ for some amount of time, and the resulting unforced dynamics are measured and collected as a training dataset. For DMD to accurately capture the behavior of the underlying system, it is important that the training data contain all relevant modes. Because different magnitudes and frequencies of the control input will excite different modes of the structure, using a single set of data would likely not yield a representative modal decomposition. To mitigate this, many different datasets resulting from varying control input profiles were collected. These datasets concatenated together form a single dataset that ideally reflects all the relevant modes of the system to which can DMD can be applied.

The training dataset is generated in simulation via a Monte Carlo approach as follows: (1) a control input profile bounded in magnitude and time is randomly generated and applied to the system; (2) the resulting unforced dynamic response is measured and collected for the subsequent 1200 seconds (about a fifth of a period of a low Earth orbit). This procedure is performed a number of times and each of the resulting datasets is concatenated together.

Training datasets are generated for a spacecraft model with different discretization sizes of the flexible appendage. In both cases the flexible appendage is a 15 meter by 15 meter square structure. The coarse discretization consists of a 6x6 grid of larger panels, whereas the finer discretization consists of an 18x18 grid of smaller panels. The snapshot matrices are constructed from the compiled training data and DMD was performed via the procedure described in Section 2.2.1 to obtain a modal decomposition for each discretization size. To rank the relative importance of each mode, the procedure described in [63] computing projection coefficients over all snapshot data is applied here. The 9 mode shapes of the appendage that contribute most to the system's response for each discretization are shown below. The hub is located at $(0, 0)$.

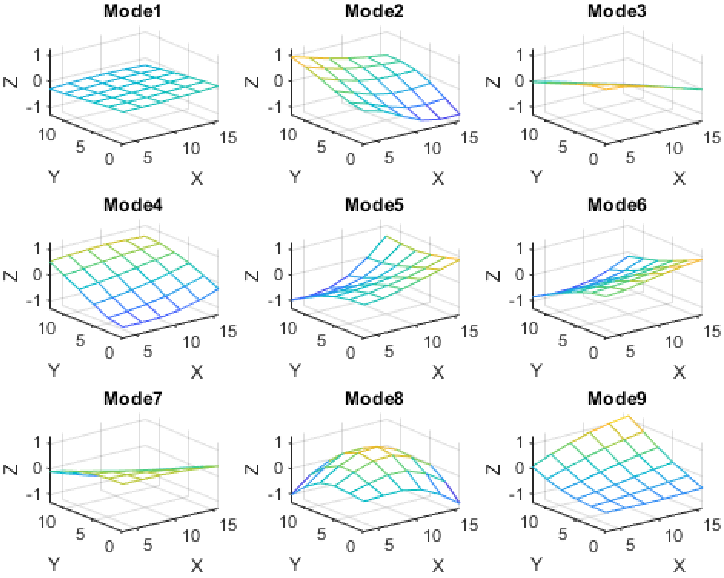

Figure 5.1: First 9 modes of spacecraft model with the 6x6 discretization of the flexible appendage.

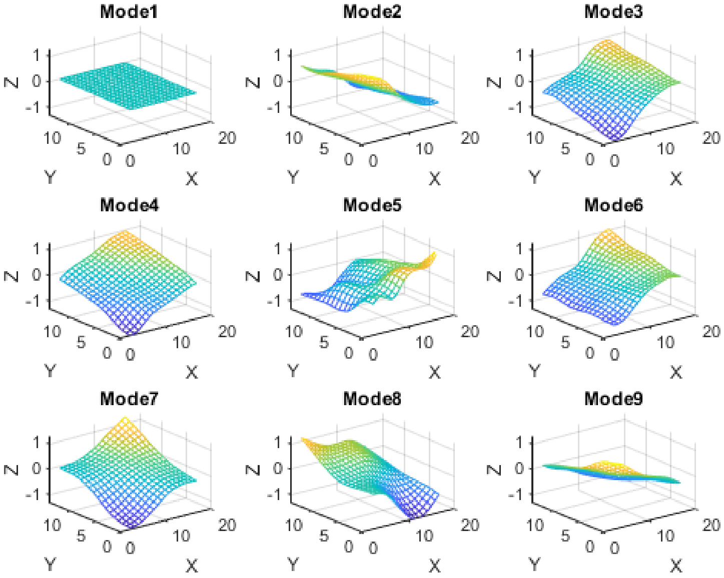

Figure 5.2: First 9 modes of spacecraft model with the 18x18 discretization of the flexible appendage.

5.2.2 Impact of Mode Selection on Reconstruction Error

To evaluate how well the decomposition captures the underlying behavior of the system, dynamics of the spacecraft model from an initial condition separate from any in the training dataset can be projected onto the DMD modes. The projection, defined by $\hat{\boldsymbol{\eta}} = CC^{\dagger}\boldsymbol{\eta}$ is used to quantify the information lost due to projecting onto a lower-dimensional model. A separate dataset is generated using the same procedure as before and the projection computed. To compute the error of a projection compared to the actual state, the following metrics are used. For position, the distance between the projected and actual position of an element is computed

$$\varepsilon_{r_i} = ||\tilde{r}_i - r_i||. \tag{5.5}$$

For velocity, the magnitude of the difference in the projected and actual velocity vectors of an element is computed

$$\varepsilon_{v_i} = ||\tilde{v}_i - v_i||. \tag{5.6}$$

For attitude, the angle between the attitudes of the actual and projection is computed

$$\varepsilon_{R_i} = \cos^{-1}\frac{\mathrm{Tr}(\hat{R}_i^T R_i) - 1}{2}. \tag{5.7}$$

For angular velocity, the magnitude of the difference between the actual and projected angular velocity is computed

$$\varepsilon_{\omega_i} = ||\tilde{\omega}_i - \omega_i||. \tag{5.8}$$

To quantify the projection error for each type of panel state (position, velocity, attitude, and angular velocity), the root mean square (RMS) error for each is taken over time and averaged over all the panels comprising the appendage. The results are shown in Fig. 5.3. To quantify error with a single quantity, a normalized root mean square error (NRMSE) metric is used. The error for each state type is normalized by the maximum of the absolute value of the measured values of that state type for the simulation, i.e., for position

$$r_{\text{err}} = \frac{1}{N} \sum_{i=1}^{N} \frac{\|\tilde{\boldsymbol{r}}_i - \boldsymbol{r}_i\|}{\max(|\boldsymbol{r}_i)|}. \tag{5.9}$$

The normalized quantities for position, velocity, attitude, and angular velocity are summed together to represent the total projection error of a simulation.

is summed together to . The sum and contribution of each state type is shown in Fig. 5.4. These metrics illustrate the effect of using different numbers of modes to represent the system dynamics. The resulting number of modes represents a significant reduction in the size of the original state-space model, which has 660 states.

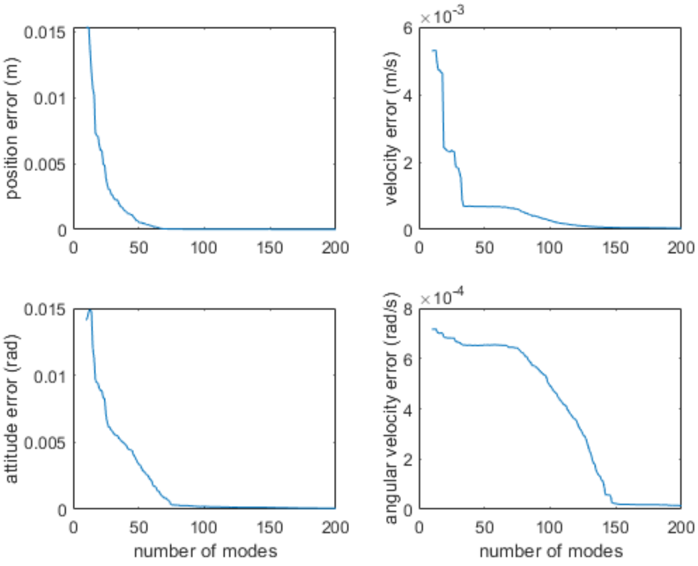

Figure 5.3: Projection error of the position, velocity, attitude, and angular velocity of resulting from using varying numbers of DMD modes to represent the underlying system dynamics.

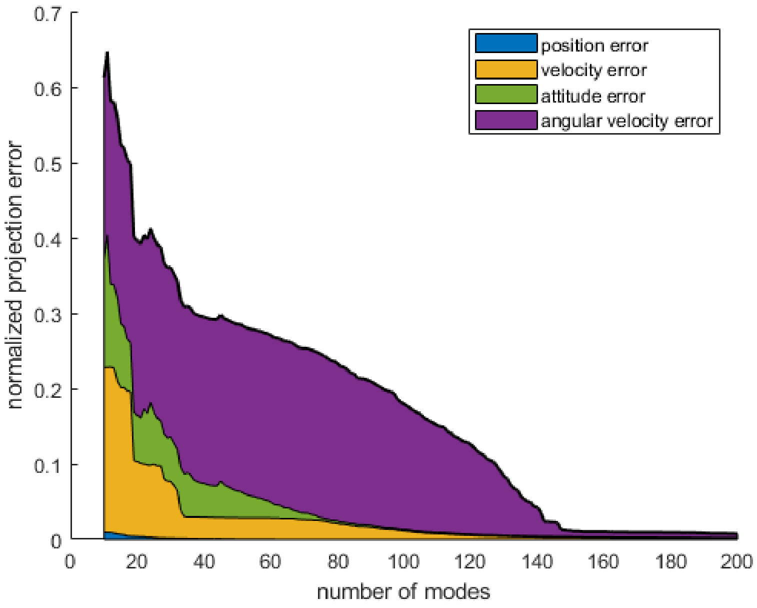

Figure 5.4: Normalized projection error resulting from using varying numbers of DMD modes to represent the underlying system dynamics.

The projection error results show that differing numbers of modes are required for different state quantities. For example, with about 50 modes, the position of each panel can be almost fully recovered from the reduced order model. For angular velocity, about 150 modes are required for minimal projection loss. In the sum of normalized errors, the angular velocity contributes most to the total error. There are also two elbows occurring around 50 and 150 modes. Until around 50 modes, significantly less error is incurred with each additional mode added. At 150 modes, there is very little benefit to adding additional modes.

To assess whether the decomposition described in 5.2.1 captures all relevant modes, the total projection error resulting from different initial conditions can be compared. total projection error is computed using the same procedure. If the decomposition is representative, the total error across a variety of samples should only vary by small magnitudes. However, if certain initial conditions result in significantly larger projection errors than others, it suggests that those initial conditions may be exciting a mode not captured by the modal decomposition. To conduct this evaluation, simulations are run across 150 samples of randomly generated initial conditions. The Monte Carlo-generated modal decomposition, using a fixed number of modes, is then employed to compute the total projection error for each simulation. The results are presented in a histogram illustrating the distribution of projection errors, as shown in Fig. 5.5. The standard deviation of the projection error is 7.25×10^{-5}. The extremely small variance in projection error suggests that the modal decomposition successfully captures all relevant modes of the system. Additionally, this consistency in error distribution provides evidence that the underlying structural dynamics can be accurately represented as linear.

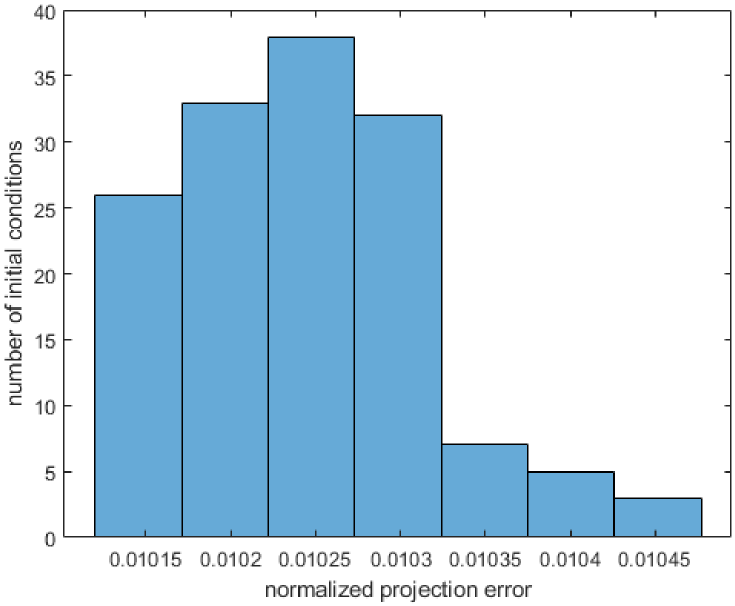

Figure 5.5: Normalized projection error resulting from using varying numbers of DMD modes to represent the underlying system dynamics.

5.3 State Estimation via a Mode Amplitude Kalman Filter

In this section, a DMD Kalman filter shown in Section 2.2.2 is applied to the flexible spacecraft model to perform state estimation given a limited set of measurements. A measurement function is proposed and numerical simulations are performed to evaluate the performance of the observation.

5.3.1 Simulation Results

Assume that there are sensors on the hub that measure the attitude and angular velocity of the hub. Assume also that there is a sensor package such as an optical sensor on the hub or some array of differential GPS sensors distributed across the appendage that capture the shape deformation of the appendage. Specifically, assume that the relative offset of a subset of the panels along the $\hat{\boldsymbol{a}}_3$ axis, i.e., $\zeta_i = \boldsymbol{r}_{i/C} \cdot \hat{\boldsymbol{a}}_3$, is measured. If there are M panels measured, the measurement vector of the system is

$$\boldsymbol{y} = \begin{bmatrix} \boldsymbol{\eta}_C & \zeta_{\mathcal{M}_1} & \dots & \zeta_{\mathcal{M}_M} \end{bmatrix}^T, \tag{5.10}$$

where $\mathcal{M}$ is the set of panels that are measured and M is the size of $\mathcal{M}$.

To perform state estimation, the unforced dynamics of the system are simulated in response to an angular impulse imparted by the reaction wheels. The modal decomposition shown in Section 5.2 is used to generate the mode amplitude state transition matrix F and observation matrix C. The initial state estimate is set assuming that the initial state of the appendage is flat and unmoving relative to the hub. Other simulation parameters are shown in Appendix C.3. The DMD Kalman filter algorithm is then applied to the measurements of the test simulation data to estimate the mode amplitudes from the shape measurements Eq. (5.10), which in turn are used to estimate the full state of the system. To evaluate the effect of model reduction on the quality of the resulting state estimate, the elbows shown in Fig. 5.4 at 50 and 150 modes are selected to represent the system. For each discretization size the measurements will be taken at the same locations on the appendage. For the 6x6 discretization, $\mathcal{M}$ is selected to be all 36 panels. For the 18x18 discretization, $\mathcal{M}$ corresponds to measuring the center panel in each 3x3 group of panels. The spacecraft parameters for each discretization size are shown below. The parameters used for the DMD Kalman filter are found in Appendix C.3. Gaussian measurement noise with a standard deviation of $0.5\ \mathrm{cm}$ is applied to the panel measurements.

To quantify the performance of the DMD Kalman filter, the state estimate is compared to the true state values. The same metrics as in Eqs. (5.5) to (5.8) are used (with the state estimate instead of the projected state) to quantify the state estimate error. Specifically, the magnitude of the difference in position, velocity, and angular velocity between the estimated and real states and the angle between the real and estimated attitude estimate are computed and averaged over each panel. The results are shown in Fig. 5.6 for the coarse discretization and Fig. 5.7 for the fine discretization. The total normalized error is again computed by normalizing each of these quantities by the maximum measured value as in Eq. (5.9). The procedure is applied to the position, velocity, attitude, and angular velocity estimates, and the normalized quantities are summed. The summed normalized error plots are shown in Fig. 5.8a and Fig. 5.8b.

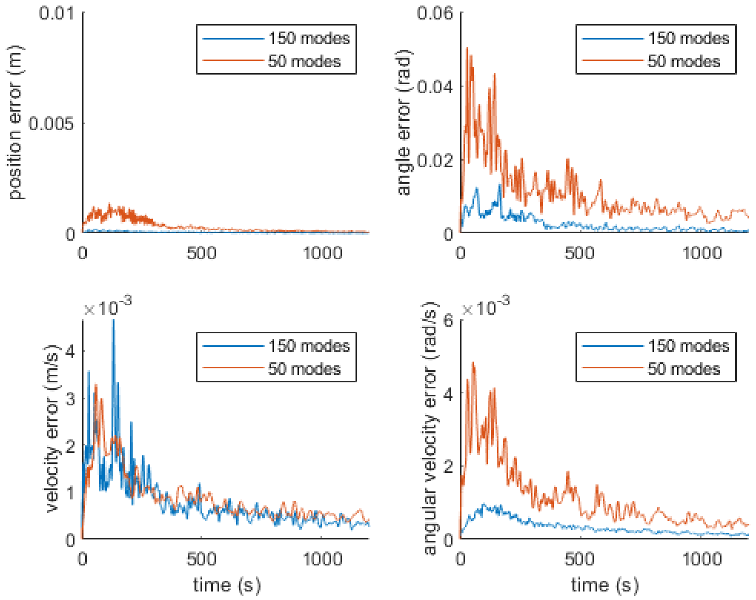

Figure 5.6: Average estimation error of the position, velocity, attitude, and angular velocity of each panel for the 6x6 discretization of the flexible appendage.

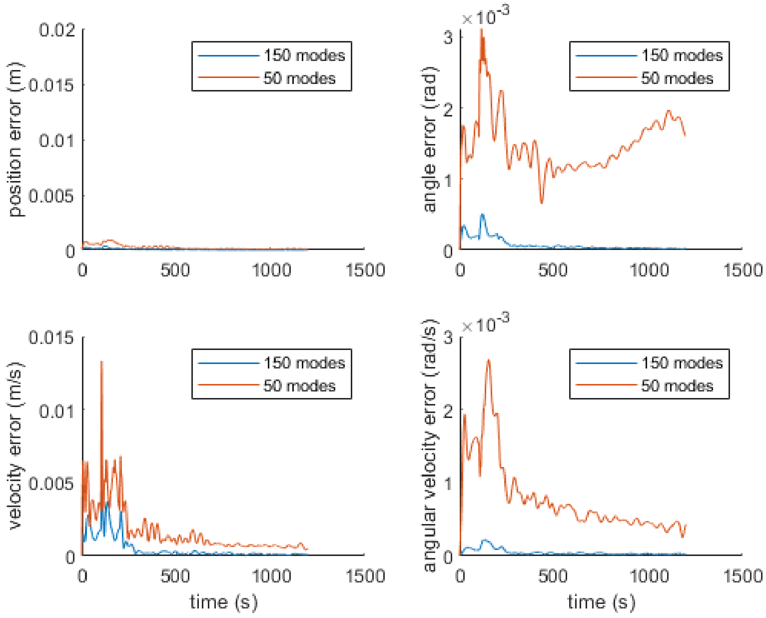

Figure 5.7: Average estimation error of the position, velocity, attitude, and angular velocity of each panel for the 18x18 discretization of the flexible appendage.

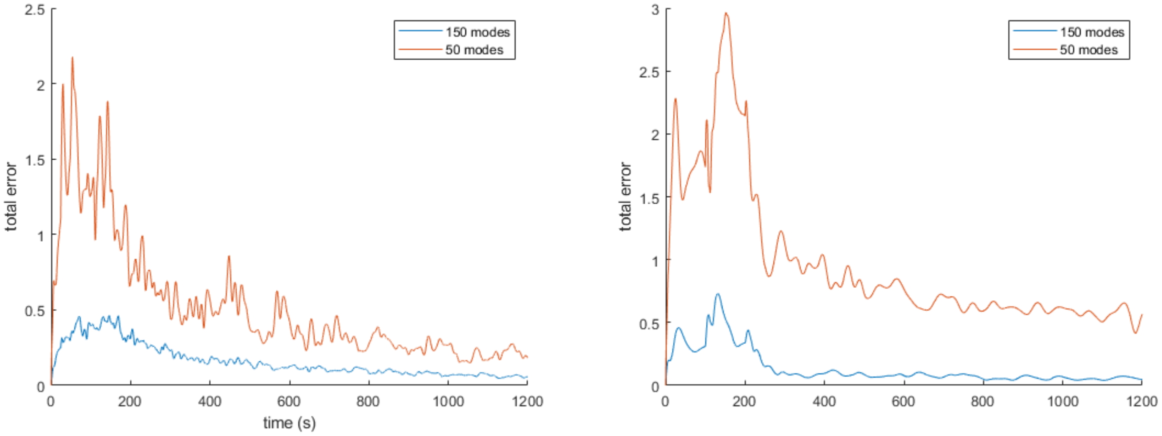

(a) 6x6 discretization

(b) 18x18 discretization

Figure 5.8: Normalized estimation error of the state of each panel of the flexible appendage compared using 50 and 150 modes for the (a) 6x6 discretization and (b) 18x18 discretization.

The results demonstrate that the estimator is able to estimate the states accurately, particularly when using 150 modes. For 150 modes, the position error is on the order of millimeters, the velocity error is on the order of millimeters per second, the attitude error is on the order of hundredths of a radian, and the angular velocity error is on the order of milliradians per second.

The difference in performance between the number of modes in estimation corresponds to what is seen in the projection error in Fig. 5.3. For position and velocity, the projection error suggests only marginal improvement going from 50 to 150 modes, whereas in attitude and angular velocity, the improvement is more substantial. This is seen in the estimation error, as the estimation of attitude and angular velocity improves more significantly by increasing to 150 modes.

5.3.2 Impact of Model Fidelity and Mode Number on Computation Time

The results from Section 5.3.1 also suggest that despite using a finer discretization, the estimator is able to accurately estimate the underlying dynamics with a similar number of modes as the coarser discretization. Consequently, the computation savings from using DMD to perform state estimation becomes more valuable the larger the state size is. For the 6x6 discretization, there are 660 states, which can be represented using 150 modes and both can be estimated using 36 measurements. For the 18x18 discretization, there are 5844 states, which also can be represented using 150 modes and estimated with only 36 measurements. Whereas estimation of such a high degree system in real time on space hardware would be computationally infeasible, the computational burden is significantly reduced using DMD and the DMD Kalman filter. To illustrate the comparison of performance versus computation time, the computation time to perform state estimation for the 1200 second simulation and the resulting steady state error was measured and shown in Fig. 5.9. The hardware that computation is measured on is a Dell Precision 3570 laptop with an Intel Core i5-1235U processor.

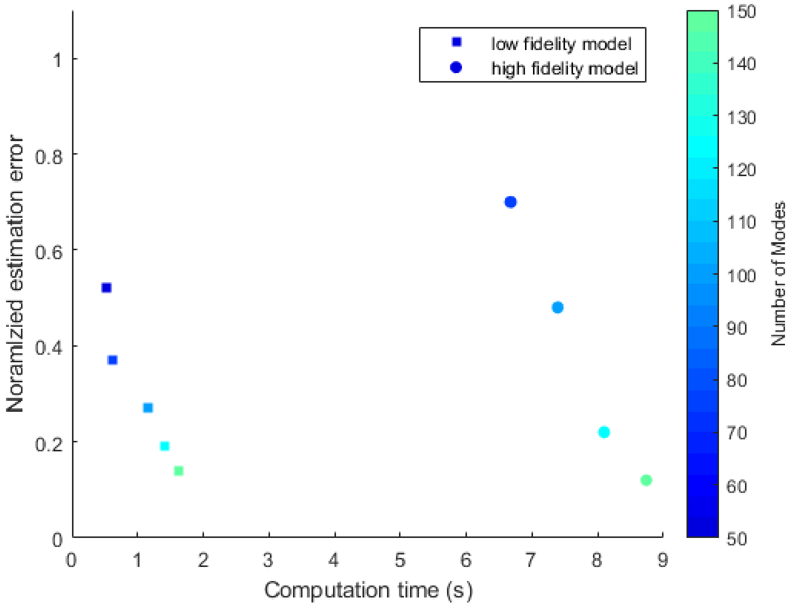

Figure 5.9: Computation time compared with performance of state estimation across different modes and discretization sizes

5.4 Optimizing Observability via Sensor Placement

The DMD Kalman Filter framework provides a structure that identifies a set of modes with amplitudes that evolve linearly, while the modes themselves are a transformation between the mode space and the state space. This framework, being inherently linear, allows the application of linear systems theory to gain deeper insights. Specifically, the observability check, which involves determining if the observability matrix is full rank, can be used to assess whether the mode amplitudes can be estimated from a given set of state measurements. A measurement function of the form Eq. (5.10) can be defined for $\hat{\boldsymbol{a}}_3$ displacement measurements of any subset of panels. Using this measurement function, a corresponding observation matrix can be constructed as described in Eq. (2.23). Together with the mode amplitude evolution matrix, this forms a linear system from which the observability Gramian can be constructed, allowing the rank test to be performed.

The measurement function and thus the observability of the system depends on both the number of sensors and sensor locations as well. To address this without exhaustively searching the entire measurement function space, a random sampling of the space of measurement functions is taken for each possible number of sensors. The rank test for observability is performed for each sample, and the percentage of samples that yield an observable system is determined. The number of random samples is chosen as 20,000 and the results of this procedure are shown in Table 5.1.

number of sensors	≤ 6	7	8	9	≥ 10
% observable systems	0	< 1	33	> 99	100

Table 5.1: Percentage of observable systems from 20,000 random samplings of the measurement function space for m sensors

The results of this observability test suggest that the critical number of measurements needed is 8. In many configurations 8 displacement measurements is sufficient to fully observe the system. For 7 sensors, almost no configuration of placements yield an observable system and for 9 sensors, almost all configurations of placements yield an observable system. To illustrate this effect state estimation using varying numbers of sensors is simulated and a plot of the total normalized error for various number of sensors is shown in Fig. 5.10.

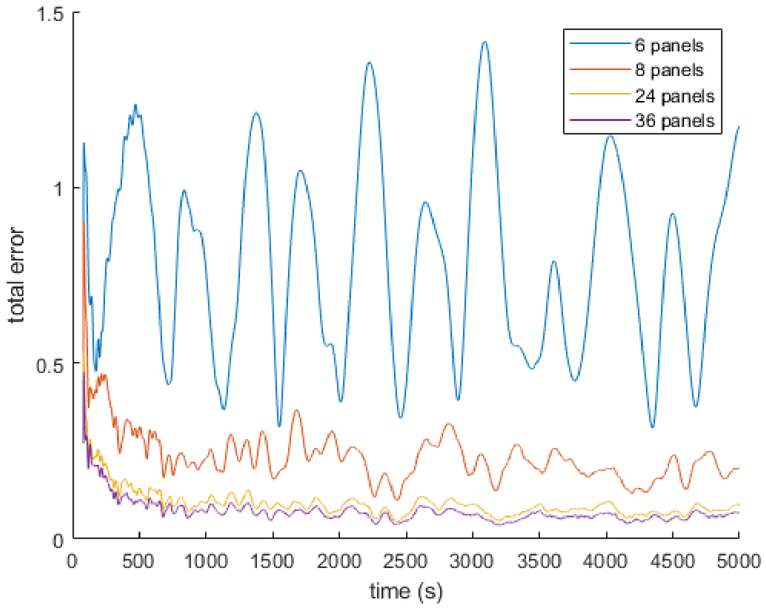

Figure 5.10: Total normalized estimation error resulting from using varying numbers of measurements of panel displacements.

The simulation demonstrates the effects of using additional sensors. Going from 6 to 8 sensors results in an observable system, and thus state estimates of reasonable quality. Increasing the numbers of sensors beyond 8 does yield better state estimates, but the gains become marginal.

More recent research addresses the use of the observability Gramian to not only answer the question of if a system is observable, but to give a qualitative metric of how observable a system is. In [73] the local unobservability index and the local estimation condition number are introduced to quantify the observability of a system. Given an observability Gramian $\mathcal{W}_O$, the local unobservability index is defined as $\frac{1}{\sqrt{\lambda_{\min}}}$, where $\lambda_{\min}$ is the smallest eigenvalue of $\mathcal{W}_O$. The local unobservability index represents a measure of the impact that measurement noise will have on estimation error. A larger index indicates a greater impact of measurement noise and thus less observability of the system. The local estimation condition number is defined as $\frac{\sqrt{\lambda_{\max}}}{\sqrt{\lambda_{\min}}}$, where $\lambda_{\max}$

is the largest eigenvalue of $\mathcal{W}_O$. The local estimation condition number quantifies how sensitive the system's output is to changes in the initial conditions. A higher local estimation condition number indicates greater sensitivity to initial conditions, which means the system's output is more affected by small changes in its initial conditions. This increased sensitivity makes it more difficult to observe or estimate the system's state accurately, thus indicating less observability of the system.

These metrics can be computed analytically for the modal decomposition of the flexible spacecraft model for any given measurement function, enabling the comparison of the quality of different measurement functions. This capability allows for optimization over different measurement functions to maximize the observability of the resulting system.

Assume that the only type of measurements of the appendage that are available are the displacements of each panel along the $\hat{\boldsymbol{a}}_3$ axis, as shown in Eq. (5.10). Assume also that there are N possible locations that M different sensors can be placed. The objective is to determine which set of M sensor locations out of the N possible locations will yield a measurement function that provides the system with the highest observability.

To generate the globally optimal location of M sensors, then all possible size M combinations of N sensor locations must be computed and the observability index checked. This requires checking $\frac{N!}{(N-M)!\ M!}$ possible measurement functions. To find the optimal location for all possible numbers of sensors in N, the number of measurement functions that must be checked is $\sum_{M=1}^{N} \frac{N!}{(N-M)!\ M!}$. For example, for $N = 36$, this quantity is on the order of billions. Increasing N (for finer discretizations or more possible sensor locations), makes it very quickly become computationally infeasible to ensure that the global optimum is found. This motivates investigating methods to find locally optimal solutions.

Assume that the for the $6x6$ discretization the set of available sensor locations are at the center of each panel. This defines the set of possible sensor locations, which has a size of $N = 36$. To find locally optimal solutions to the sensor placement problem for this configuration, two different optimization algorithms are employed. The first is a greedy algorithm to significantly reduce the search space, and the second uses a Monte Carlo approach to randomly sample the search space.

The first optimization technique utilized is a greedy algorithm. In this approach, the optimal position for the first sensor is determined and fixed. Subsequently, the optimal position for the second sensor is determined while keeping the first sensor's position fixed. This process continues iteratively, with each previously selected sensor location remaining fixed while the position of each new sensor is optimized. With this method, the search space for determining the location of the ith sensor is $N - i$. To determine the optimal location for all possible number of sensors in N, the total number of measurement functions that must be checked is $N + (N-1) + (N-2) + ... + 1 = \frac{N(N+1)}{2}$. This approach reduces the order of magnitude of the entire search space to N^2 which for $N = 36$ makes an exhaustive search feasible.

The second optimization technique employs a Monte Carlo approach. This approach utilizes random sampling and perturbation to explore the solution space and identify configurations that maximize observability. In this approach, to determine the optimal location of M sensors in N possible locations, the iterative process shown in Algorithm 1 is followed:

Algorithm 1 Monte Carlo Optimization Algorithm

```
Initialization:
Generate $S$ random samples of different size $M$ combinations of $N$.
Compute the measurement function and observability index for each sample.
Keep the $U$ samples with the best observability and discard the rest.
repeat
    for each of the $U$ samples do
        Randomly perturb sample $P$ times to generate $P$ new sample measurement functions.
    end for
    Compare observability index of the original $U$ and the new $U \times P$ samples
    Collect $U$ samples with the highest observability
until convergence or maximum number of iterations $J$ is reached
```

This iterative process continues until a convergence criterion is met or a maximum number of iterations is reached. The best sample from the final set of U samples is selected and represents a local optimum. The maximum total number of measurement functions that need to be checked with this approach is $S + J(UP)$. The parameters $S,\ U,\ P,$ and J can be chosen such that the search space is limited to a computationally feasible size.

Using the 150 mode decomposition for the 6x6 discretization and displacement measurements of the form shown in Eq. (5.10), both optimization procedures were performed for varying numbers of sensors, specifically for all even numbers from 6 to 32. For the Monte Carlo approach, the search parameters are set as $S = 20,000$, $U = 100$, $P = 20$, and $J = 50$ The results are visualized in Fig. 5.11 which shows a heatmap indicating the frequency with which each sensor location was selected across the optimization solutions.

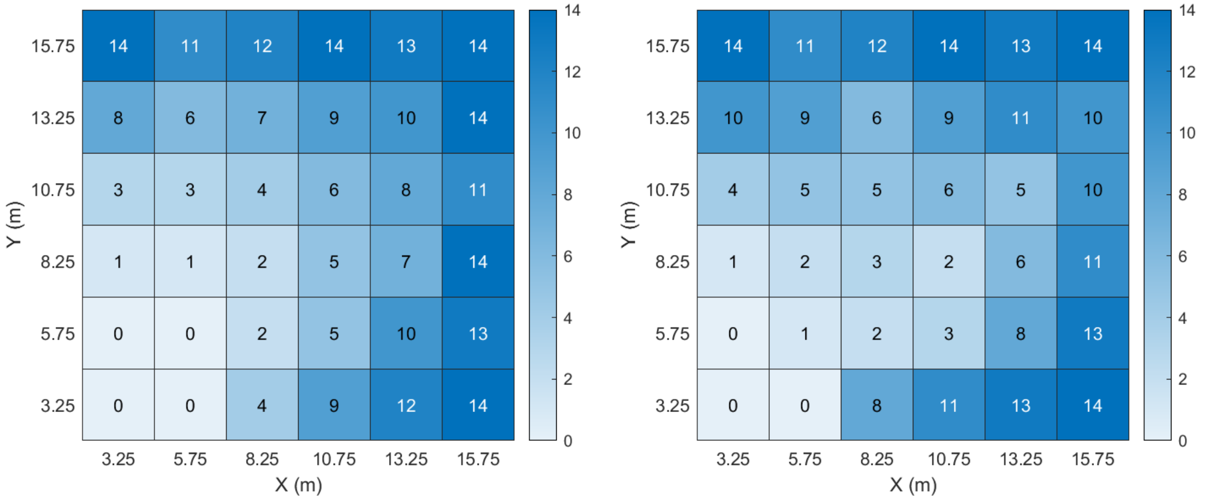

	3.25	5.75	8.25	10.75	13.25	15.75
15.75	14	11	12	14	13	14
13.25	8	6	7	9	10	14
10.75	3	3	4	6	8	11
8.25	1	1	2	5	7	14
5.75	0	0	2	5	10	13
3.25	0	0	4	9	12	14

(a) Greedy Optimization

	3.25	5.75	8.25	10.75	13.25	15.75
15.75	14	11	12	14	13	14
13.25	10	9	6	9	11	10
10.75	4	5	5	6	5	10
8.25	1	2	3	2	6	11
5.75	0	1	2	3	8	13
3.25	0	0	8	11	13	14

(b) Monte Carlo Optimization

Figure 5.11: Heatmap of sensor locations for varying number of sensors optimized via a greedy approach and a Monte Carlo approach. The optimization tends to favor sensors on the edges of the appendage

The distribution of sensors in the heatmap indicates that sensors are most valuable on the edges and corners of the appendage, and away from the diagonal running from $(0, 0)$ to $(15, 15)$. This suggests that for displacement measurements, the most informative data for estimating the mode amplitudes is obtained from those locations. This observation is consistent with the mode shape plots in Fig. 5.1, where the most significant modes exhibit the largest displacements in these areas. As the appendage oscillates, the most substantial motions occur at the corners and edges, away from the central diagonal. Placing sensors at these locations effectively captures these motions, enabling better estimations of the mode amplitudes and highlighting the utility of understanding the shapes of the most impactful modes.

5.5 Conclusion

This chapter explores the use of dynamic mode decomposition (DMD) for state estimation of the flexible spacecraft model. First, the attitude and shape dynamics of the spacecraft are decoupled from the translational dynamics of the hub. A Monte Carlo approach simulating the system's response to random control input profiles generates a set of training data to encompass all the relevant modes of the system. DMD is then applied to yield a modal decomposition of the training data, and the mode shapes are analyzed for two different discretization sizes of the flexible appendage.

The modal decomposition results in a linear framework wherein the mode amplitudes of the reduced-order model evolve linearly over time, and the mode shapes serve as a linear operator transforming between the mode amplitude space and the system state space. This linear framework facilitates the implementation of a Kalman filter to estimate the mode amplitudes of the system from a set of state space measurements. Numerical simulations demonstrate that this observer provides accurate state estimates from displacement measurements of the panels comprising the appendage in the $\hat{\boldsymbol{a}}_3$ direction. Additionally, the reduced-order model requires less computation time for state estimation.

The observer framework facilitates the computation of the observability matrix and Gramian. The rank condition for observability with varying numbers of measurements offers insight into the minimum number of measurements required to make the system observable. The eigenvalues of the observability Gramian for a given measurement function provide a metric that quantifies the level of observability. This metric enables the optimization of the measurement function to maximize system observability. The optimization process involves varying the number and placement of displacement sensors. The results highlight the optimal locations on the appendage where measurements will contribute most to system observability. Comparing these optimal locations with the mode shapes reveals that the best sensor positions correspond to areas with the largest displacements.

Chapter 6: Conclusion

6.1 Summary of Dissertation

This dissertation explores the use of magnetic torque rods to stabilize the shape of a flexible spacecraft. This dissertation has contributed to the dynamic modeling, estimation, and control of a flexible spacecraft. The spacecraft model utilizes a hub and appendage framework such that the hub is rigid, actuated by reaction wheels and is responsible for attitude control, and the appendage is a flexible, thin, planar structure and has magnetic torque rods distributed across it to stabilize its shape. A multibody model consisting of rigid elements connected by damped spring-like hinges models the flexibility of the structure.

Initially the flexibility of the appendage is restricted to one direction, enabling the dynamics of the model to be restricted to the orbital plane. Springs to model internal forces and moments, external disturbances, and actuator constraints are considered in modeling the dynamics of the system. The nonlinearities in the model suggest a Lyapunov-based approach to the control design. Lyapunov analysis yields an attitude and shape-stabilizing control law that asymptotically drives the attitude to a desired orientation and the shape of the appendage to flat.

Numerical simulations demonstrate that the magnetic torque rods contribute significantly to a reduction in deformations and oscillations of the appendage compared to a system without torque rods and a system with torque rods but with a different control law. The faster stabilization of the appendage also improves the performance of the attitude controller. Simulations further illustrate the impact of time-varying control authority of the magnetic torque rods, showing reduced performance with diminished control authority, yet still performing better than an unactuated appendage.

The application of an extended Kalman filter (EKF) to the planar model enables state estimation of the flexible spacecraft. Using a measurement function that includes the translational and angular rates of the appendage's elements results in an observable system. The state estimate serves as feedback for the controller within an output feedback control framework. Numerical simulations compare the performance of controllers in output feedback with the Lyapunov-based controller in state feedback, demonstrating that control objectives are still achievable with the output feedback controller with nearly the same performance.

The flexible spacecraft model is extended to three dimensions, using rotation matrices to represent the attitude dynamics. The appendage is discretized in two directions, allowing for unrestricted bending between elements. To compensate for the additional degrees of freedom, an additional torque rod is incorporated, resulting in pairs of torque rods distributed across the appendage. Lyapunov analysis is employed to derive a control law for the reduced attitude of a single element. Numerical simulations validate the effectiveness of this control law for a single rigid element, highlighting its applicability to the field of pointing control for small-scale satellites Additional simulations demonstrate that the control law remains effective even when saturation nonlinearities are introduced.

The reduced attitude control law for a pair of magnetic torque rods is implemented to stabilize the shape of the flexible appendage. To evaluate the impact and robustness of this shape stabilization, two types of disturbances are considered. The first disturbance focuses on the excitation of the flexible modes of the appendage resulting from an attitude maneuver performed by the hub. The second disturbance examines periodic shape deformations caused by thermal gradients, which induce bending as the faces of the appendage are unevenly heated throughout an orbit. In response to maneuver-induced oscillations, numerical simulations demonstrate that the shape-stabilizing control effectively dampens vibrations and returns the appendage to its flat state more quickly compared to performing the same maneuver without the torque rods. Additionally, the average deformation of the appendage over time is significantly reduced. In response to thermoelastic bending, the torque rods significantly mitigate the deformation experienced by the appendage, reducing the deformation magnitude by up to half. The simulations also show that the reaction wheels must exert more control effort to maintain an attitude reference when the torque rods are actuated.

To enable computationally feasible state estimation, dynamic mode decomposition (DMD) is employed. Using a set of training data generated via simulation, DMD yields a modal decomposition of the spacecraft dynamics. By reducing the number of modes used, the spacecraft dynamics can be represented by a reduced-order model with significantly fewer states than the original state-space system. Additionally, the reduced order model is linear in the mode-amplitude space. Using the mode shapes, a linear observation function transforms between the mode amplitude space and the state space. This linear framework allows for the application of a Kalman filter that estimates the mode amplitudes from a limited set of state space measurements.

Numerical simulations demonstrate the DMD Kalman filter is able to estimate the state of the spacecraft accurately using the reduced order model with measurement noise and with a significant reduction in states, which represents significant savings in computation cost. The linear framework resulting from DMD enables the observability to be computed for various measurement functions corresponding to different numbers and locations of sensors. The observability rank condition shows that generally 8 displacement sensors are needed to fully observe the system. The eigenvalues of the observability Gramian quantify observability and facilitate the optimization of sensor locations to maximize observability for a given number of sensors. The optimization results for various sensor quantities reveal the critical locations on the appendage where measurements most significantly contribute to the system's overall observability.

The results of this research provide a promising approach to shape stabilization of flexible spacecraft. However, there are still some uncertainties about what was studied. The validation done via simulation can demonstrate effective performance for particular designs, configurations, and parameters, but inherently does not guarantee performance generally. The theoretical results for the planar problem and for two-axis control using two magnetic torque rods provide confidence that this approach is generally effective, but additional theoretical analysis, which is the subject of ongoing work, is required to fully generalize the results.

6.2 Suggestions for Future Research

The modeling approach to structural flexibility in this dissertation seeks to approximate the flexibility of both continuous and multibody structures via a multibody discretization. Ongoing and future work should seek to examine the accuracy with which this approach approximates the dynamics of a continuous flexible body. Investigating the trade between modeling accuracy and discretization size is also of interest.

The results in this dissertation The analysis for the reduced attitude control of a rigid body using only two magnetic torque rods can be improved by relaxing some of the simplifying assumptions made in this dissertation to provide additional robustness guarantees of the control law. Specifically, future analysis should include the periodic variations of the local magnetic field corresponding to orbital periods, which make the dynamics non-autonomous and requires additional analysis to characterize. Analysis that explicitly considers the saturation nonlinearities typical of a physical system should also be explored.

Dynamic mode decomposition (DMD) is a promising approach for estimating high-dimensional representations of flexible spacecraft. However, because DMD requires training data that cannot be directly obtained from a physical system without measuring all the system states, this presents a challenge. To address this challenge future work should investigate methods for performing system identification to estimate parameters that characterize the spacecraft dynamics. System identification would facilitate the correlation of physical data with simulated data, allowing the simulation data to accurately represent the dynamics of the real system. Consequently, the dynamic modes derived from numerical simulation data would be valid for the physical system, thereby making the training data appropriate for DMD applications.

In optimizing the number and location of sensors, this dissertation only considers measurements of displacements at various points on the appendage. Optimizations that consider other types of measurements, such as the attitude and angular rate at various locations on the appendage should be considered.

Appendix A: Additional Equations

A.1 Two-Dimensional Internal Forces and Moments

The force terms for each spacecraft component are shown. For an appendage that has two appendages on either side of it and is on the right side of the hub, $i \in [2, N-1]$, the forces and moments are as follows:

$$
\begin{aligned}
X_{i/i+1} = k_s &\left(x_{(i+1)/C} - x_{i/C} - \frac{L_{i+1}}{2}\cos\alpha_{i+1} - \frac{L_i}{2}\cos\alpha_i \right) \\
&+ c_s \left(\dot{x}_{(i+1)/C} - \dot{x}_{i/C} + \frac{L_{i+1}}{2}\dot{\alpha}_{i+1}\sin\alpha_{i+1} + \frac{L_i}{2}\dot{\alpha}_i\sin\alpha_i \right)
\end{aligned}
$$

$$
\begin{aligned}
X_{i/i-1} = -k_s &\left(x_{i/C} - x_{(i-1)/C} - \frac{L_i}{2}\cos\alpha_i - \frac{L_{i-1}}{2}\cos\alpha_{i-1} \right) \\
&+ c_s \left(\dot{x}_{i/C} - \dot{x}_{(i-1)/C} + \frac{L_i}{2}\dot{\alpha}_i\sin\alpha_i + \frac{L_{i-1}}{2}\dot{\alpha}_{i-1}\sin\alpha_{i-1} \right)
\end{aligned}
$$

$$
\begin{aligned}
Y_{i/i+1} = k_s &\left(y_{(i+1)/C} - y_{i/C} - \frac{L_{i+1}}{2}\sin\alpha_{i+1} - \frac{L_i}{2}\sin\alpha_i \right) \\
&+ c_s \left(\dot{y}_{(i+1)/C} - \dot{y}_{i/C} + \frac{L_{i+1}}{2}\dot{\alpha}_{i+1}\cos\alpha_{i+1} + \frac{L_i}{2}\dot{\alpha}_i\cos\alpha_i \right)
\end{aligned}
$$

$$
\begin{aligned}
Y_{i/i-1} = -k_s &\left(y_{i/C} - y_{(i-1)/C} - \frac{L_i}{2}\sin\alpha_i - \frac{L_{i-1}}{2}\sin\alpha_{i-1} \right) \\
&+ c_s \left(\dot{y}_{i/C} - \dot{y}_{(i-1)/C} + \frac{L_i}{2}\dot{\alpha}_i\cos\alpha_i + \frac{L_{i-1}}{2}\dot{\alpha}_{i-1}\cos\alpha_{i-1} \right)
\end{aligned}
$$

$$T_{i/i+1} = \frac{L_i}{2} \cos\alpha_i Y_{i/i+1} - \frac{L_i}{2} \sin\alpha_i X_{i/i+1}$$

$$T_{i/i-1} = -\frac{L_i}{2} \cos\alpha_i X_{i/i-1} + \frac{L_i}{2} \sin\alpha_i Y_{i/i-1}$$

$$M_{i/i+1} = k_t(\alpha_{i+1} - \alpha_i) + c_t(\dot{\alpha}_{i+1} - \dot{\alpha}_i)$$

$$M_{i/i-1} = -k_t(\alpha_i - \alpha_{i-1}) - c_t(\dot{\alpha}_i - \dot{\alpha}_{i-1})$$

For appendages on the left that have a appendage on either side, $i \in [N+2, 2N-1]$, the forces and moments are the negation of what is shown above, because the indexing goes in the opposite direction.

For the appendage where $i = 1$ the forces and moments are as follows.

$$X_{1,2} = k_s \left(x_{2/C} - x_{1/C} - \frac{L_2}{2} \cos\alpha_2 - \frac{L_1}{2} \cos\alpha_1 \right) + c_s \left(\dot{x}_{2/C} - \dot{x}_{1/C} + \frac{L_2}{2} \dot{\alpha}_2 \sin\alpha_2 + \frac{L_1}{2} \dot{\alpha}_1 \sin\alpha_1 \right)$$

$$\begin{aligned} X_{1/C} &= -k_s \left(x_{1/C} - x_{c/c} - \frac{L_1}{2} \cos\alpha_1 - \frac{L_C}{2} \cos\gamma \right) + c_s \left(\dot{x}_{1/C} - \dot{x}_{c/c} + \frac{L_1}{2} \dot{\alpha}_1 \sin\alpha_1 + \frac{L_C}{2} \dot{\alpha}_c \sin\gamma \right) \\ &= -k_s \left(x_{1/C} - \frac{L_1}{2} \cos\alpha_1 - \frac{L_C}{2} \right) + c_s \left(\dot{x}_{1/C} + \frac{L_1}{2} \dot{\alpha}_1 \sin\alpha_1 \right) \end{aligned}$$

$$Y_{1/2} = k_s \left(y_{2/C} - y_{1/C} - \frac{L_2}{2} \sin\alpha_2 - \frac{L_1}{2} \sin\alpha_1 \right) + c_s \left(\dot{y}_{2/C} - \dot{y}_{1/C} + \frac{L_2}{2} \dot{\alpha}_2 \cos\alpha_2 + \frac{L_1}{2} \dot{\alpha}_1 \cos\alpha_1 \right)$$

$$Y_{1/C} = -k_s\left(y_{1/C} - y_{c/c} - \frac{L_1}{2}\sin\alpha_1 - \frac{L_C}{2}\sin\gamma\right) + c_s\left(\dot{y}_{1/C} - \dot{y}_{c/c} + \frac{L_1}{2}\dot{\alpha}_1\cos\alpha_1 + \frac{L_C}{2}\dot{\alpha}_c\cos\gamma\right)$$
$$= -k_s\left(y_{1/C} - \frac{L_1}{2}\sin\alpha_1\right) + c_s\left(\dot{y}_{1/C} + \frac{L_1}{2}\dot{\alpha}_1\cos\alpha_1\right)$$

$$T_{1/2} = \frac{L_1}{2}\cos\alpha_1 Y_{1,2} - \frac{L_1}{2}\sin\alpha_1 X_{1,2}$$

$$T_{1/C} = -\frac{L_1}{2}\cos\alpha_1 X_{1,C} + \frac{L_1}{2}\sin\alpha_1 Y_{1,C}$$

$$M_{1/2} = k_t(\alpha_2 - \alpha_1) + c_t(\dot{\alpha}_2 - \dot{\alpha}_1)$$

$$M_{1/C} = -k_t(\alpha_1 - \gamma) - c_t(\dot{\alpha}_1 - \dot{\alpha}_C)$$
$$= -k_t(\alpha_1) - c_t(\dot{\alpha}_1)$$

For the appendage $i = N + 1$, which is the appendage directly to the left of the hub

$$X_{(N+1)/C} = k_s\left(-x_{(N+1)/C} - \frac{L_C}{2} - \frac{L_{N+1}}{2}\cos\alpha_{N+1}\right) + c_s\left(-\dot{x}_{(N+1)/C} + \frac{L_{N+1}}{2}\dot{\alpha}_{N+1}\sin\alpha_{N+1}\right)$$

$$X_{(N+1)/(N+2)} = -k_s\left(x_{(N+1)/C} - x_{(N+2)/C} - \frac{L_{N+1}}{2}\cos\alpha_{N+1} - \frac{L_{N+2}}{2}\cos\alpha_{N+2}\right)$$
$$+ c_s\left(\dot{x}_{(N+1)/C} - \dot{x}_{(N+2)/C} + \frac{L_{N+1}}{2}\dot{\alpha}_{N+1}\sin\alpha_{N+1} + \frac{L_{N+2}}{2}\dot{\alpha}_{N+2}\sin\alpha_{N+2}\right)$$

$$Y_{(N+1)/C} = k_s\left(-y_{(N+1)/C} - \frac{L_{N+1}}{2}\sin\alpha_{N+1}\right) + c_s\left(-\dot{y}_{(N+1)/C} + \frac{L_{N+1}}{2}\dot{\alpha}_{N+1}\cos\alpha_{N+1}\right)$$

$$\begin{aligned}Y_{(N+1)/(N+2)} =& - k_s \left(y_{(N+1)/C} - y_{(N+2)/C} - \frac{L_{N+1}}{2} \sin \alpha_{N+1} - \frac{L_{N+2}}{2} \sin \alpha_{N+2} \right) \\ & + c_s \left(\dot{y}_{(N+1)/C} - \dot{y}_{(N+2)/C} + \frac{L_{N+1}}{2} \dot{\alpha}_{N+1} \cos \alpha_{N+1} + \frac{L_{N+2}}{2} \dot{\alpha}_{N+2} \cos \alpha_{N+2} \right)\end{aligned}$$

$$T_{(N+1)/C} = \frac{L_{N+1}}{2} \cos \alpha_{N+1} Y_{(N+1)/C} - \frac{L_{N+1}}{2} \sin \alpha_{N+1} X_{(N+1)/C}$$

$$T_{(N+1)/(N+2)} = -\frac{L_{N+1}}{2} \cos \alpha_{N+1} X_{N+1,N+2} + \frac{L_{N+1}}{2} \sin \alpha_{N+1} Y_{N+1,N+2}$$

$$M_{(N+1)/C} = k_t(-\alpha_{N+1}) + c_t(-\dot{\alpha}_{N+1})$$

$$M_{(N+1)/(N+2)} = -k_t(\alpha_{N+1} - \alpha_{N+2}) - c_t(\dot{\alpha}_{N+1} - \dot{\alpha}_{N+2})$$

For the case of the end appendage, $i = N$, the same equations as the middle appendages between $i = 1$ and $i = N$ are used, except $X_{i/(i+1)}$, $Y_{i/(i+1)}$, $T_{i/(i+1)}, M_{i/(i+1)}$ are all zero, because there is only one adjacent appendage. Similarly, for the other end appendage, $i = 2N$, the equations for $i \in [N + 2, 2N - 1]$ can be used, where $X_{i/(i+1)}, Y_{i/(i+1)}, T_{i/(i+1)}, M_{i/(i+1)}$ are also all zero. The forces and moments acting on the hub are equal and opposite to those acting on the appendages attached to the hub, i.e.,

$$
\begin{aligned}
X_{C/1} &= -X_{1/C} \\
X_{C/(N+1)} &= -X_{(N+1)/C} \\
Y_{C/1} &= -Y_{1/C} \\
Y_{C/(N+1)} &= -Y_{(N+1)/C} \\
T_{C/1} &= \tfrac{L_c}{2} Y_{C/1} \\
T_{C/(N+1)} &= -\tfrac{L_c}{2} Y_{C/(N+1)} \\
M_{C/1} &= -M_{1/C} \\
M_{C/(N+1)} &= -M_{(N+1)/C}
\end{aligned}
$$

The total forces and moments are

$$
\begin{aligned}
X_i &= X_{i/(i+1)} + X_{i/(i-1)} \\
Y_i &= Y_{i/(i+1)} + Y_{i/(i-1)} \\
T_i &= T_{i/(i+1)} + T_{i/(i-1)} \\
M_i &= M_{i/(i+1)} + M_{i/(i-1)}
\end{aligned}
$$

$$\begin{aligned}
X_c &= X_{C,1} + X_{C,N} \\
Y_c &= Y_{C,1} + Y_{C,N} \\
T_c &= T_{C,1} + T_{C,N} \\
M_c &= M_{C,1} + M_{C,N}
\end{aligned}$$

Appendix B: Lyapunov Stability Analysis

B.1 Lyapunov's Direct Method

The behavior of an equilibrium point of an autonomous system can be characterized using Lyapunov's direct method [74]. This method utilizes a scalar potential candidate function and its derivative to assess the stability of the system near the equilibrium point. Consider the autonomous system

$$\dot{\boldsymbol{x}} = \boldsymbol{f}(\boldsymbol{x}).$$

Let $\boldsymbol{x}^* = \mathbf{0}$ be an equilibrium point for the system and $D \subset \mathcal{R}^n$ be a domain containing $\boldsymbol{x}^*$. Let $V : D \rightarrow R$ the scalar function such that $V(\mathbf{0}) = \mathbf{0}$ and $V(\boldsymbol{x}) > 0 \quad \forall x \neq \boldsymbol{x}^*$, i.e., V is positive definite. If V is continuously differentiable and $\dot{V}$ is negative definite, i.e., [74]

$$\dot{V}(\boldsymbol{x}) < 0 \quad \forall \boldsymbol{x} \neq \boldsymbol{x}^*,$$

then the equilibrium point $\boldsymbol{x}^* = \mathbf{0}$ is asymptotically stable.

B.2 LaSalle's Invariance Principle

LaSalle's theorem extends Lyapunov's direct method by allowing the use of Lyapunov functions that do not have a negative definite derivative. It provides a way to determine the asymptotic behavior of the system, leading to conclusions about stability based on the largest invariant set where the derivative of the Lyapunov function is zero. The main idea of the invariance principle is if it can be established that no trajectory can stay at points where $\dot{V}(\boldsymbol{x}) = \mathbf{0}$ except at the origin, then the origin is asymptotically stable [74]. Consider the autonomous system

$$\dot{\boldsymbol{x}} = \boldsymbol{f}(\boldsymbol{x}).$$

If there exists a Lyapunov function $V(\boldsymbol{x})$ such that $V(\boldsymbol{x}) > \mathbf{0}$ and $\dot{V}(\boldsymbol{x}) \leq 0$, then the system will converge to the largest invariant set of the set where $\dot{V}(\boldsymbol{x}) = \mathbf{0}$. If it can be shown that the largest invariant set in $\boldsymbol{x} \ : \ \dot{V}(\boldsymbol{x}) = 0$ is the origin, $\boldsymbol{x}^* = \mathbf{0}$, then $\boldsymbol{x}^*$ is asymptotically stable [74].

B.3 Proof of Lemma 1

Proof: Assume $\dot{V}(\boldsymbol{x}) < 0$ along solutions of the closed loop linear system Eq. (3.52), which implies

$$\frac{\partial V}{\partial \boldsymbol{x}}(A\boldsymbol{x} + B\boldsymbol{g}(\boldsymbol{x})) < 0$$

Assume solutions of the closed loop linear system Eq. (3.52) can be be shown to be bounded

$$\frac{\partial V}{\partial \boldsymbol{x}}(A\boldsymbol{x} + B\boldsymbol{g}(\boldsymbol{x})) < -c\|\boldsymbol{x}\|^2,$$

for some constant $c > 0$. Then,

$$\frac{\partial V}{\partial \boldsymbol{x}} f(\boldsymbol{x}) = \frac{\partial V}{\partial \boldsymbol{x}}(A\boldsymbol{x} + B\boldsymbol{g}(\boldsymbol{x})) + \frac{\partial V}{\partial \boldsymbol{x}}\text{H.O.T.} < -c\|\boldsymbol{x}\|^2 + \frac{\partial V}{\partial \boldsymbol{x}}\text{H.O.T.}$$

Because $\frac{\partial V}{\partial x}\text{H.O.T.}$ is $O(\|x\|^3)$, then $\frac{\partial V}{\partial x} f(x) < 0$ for sufficiently small $\|x\|$ and $\frac{\partial V}{\partial x} f(x) = 0$ when $\|x\| = 0$.

Appendix C: Simulation Parameters

C.1 Parameters Used in Chapter 3

parameter name	symbol	value	units
semi-major axis	a	6778	km
eccentricity	e	0	
inclination	i	90	deg
right ascension of the ascending node	Ω	0	deg
argument of periapsis	ω	0	deg
latitude at epoch	u_0	90	deg
attitude	γ_0	112	deg
angular velocity	$\dot{\gamma}_0$	0.07	$\frac{\text{deg}}{\text{s}}$

Table C.1: Hub initial conditions

Control Parameters

$$Q_c = \mathrm{diag}(300, 5)$$

$$Q_i = \mathrm{diag}(1, 1, 1000, 1, 10, 10)$$

$$Q = \mathrm{diag}(Q_c, Q_1, ..., Q_{2N})$$

$$R_c = 20000$$

$$R_i = 0.001$$

$$R = \mathrm{diag}(R_c, R_1, ..., R_{2N})$$

$$k_p = 10$$

$$k_L = 1100$$

Spacecraft Parameters

parameter	symbol	value	unit
panels per appendage	N	12	
hub mass	m_C	100	kg
panel mass	m_i	1	kg
hub moment of inertia	I_C	50	kgm^2
panel moment of inertia	I_i	0.1	kgm^2
panel length	L_i	1	m
hub length	L_C	2	m
connection spring coefficient	k_s	100	$\frac{\mathrm{N}}{\mathrm{m}}$
connection damping coefficient	c_s	0.1	$\frac{\mathrm{Ns}}{\mathrm{m}}$
torsional spring coefficient	k_t	10	$\frac{\mathrm{Nm}}{\mathrm{rad}}$
torsional damping coefficient	c_t	0.1	$\frac{\mathrm{Nms}}{\mathrm{rad}}$
orbit angular speed	w_0	1.2×10^{-3}	$\frac{\mathrm{rad}}{\mathrm{s}}$
reaction wheel saturation	K_{rw}	0.01	Nm
torque rod saturation	K_{tr}	1×10^{-4}	Nm

Table C.2: Spacecraft Parameters

State Estimation Simulation Parameters

parameter	value	unit
$\sigma_{\dot{xy}}$	0.01	$\frac{m}{s}$
$\sigma_{\dot{\alpha}}$	0.5	$\frac{\mathrm{deg}}{\mathrm{s}}$
σ_{γ}	0.3	deg
$\sigma_{\dot{\gamma}}$	0.3	$\frac{\mathrm{deg}}{\mathrm{s}}$
ρ_{γ}	0.6	deg
$\rho_{\dot{\gamma}}$	0.6	$\frac{\mathrm{deg}}{\mathrm{s}}$
ρ_{xy}	0.01	m
ρ_{α}	0.25	deg
$\rho_{\dot{xy}}$	0.01	$\frac{\mathrm{m}}{\mathrm{s}}$
$\rho_{\dot{\alpha}}$	0.2	$\frac{\mathrm{deg}}{\mathrm{s}}$

Table C.3: State Estimation Measurement and Process Noise Parameters

$$Q_c = \mathrm{diag}(\rho_{\gamma}^2, \rho_{\dot{\gamma}}^2)) \quad Q_i = \mathrm{diag}(\rho_{xy}^2, \rho_{xy}^2, \rho_{\alpha}^2, \rho_{\dot{xy}}^2, \rho_{\dot{\alpha}}^2)$$

$$Q = \textbf{diag}(Q_c, Q_i, ..., Q_i)$$

$$R_c = \mathrm{diag}(\sigma_{\gamma}, \sigma_{\dot{\gamma}}) \quad R_i = \mathrm{diag}(\sigma_{\dot{xy}}, \sigma_{\dot{xy}}, \sigma_{\dot{\alpha}})$$

$$Q = \textbf{diag}(R_c, R_i, ..., R_i)$$

C.2 Parameters Used in Chapter 4

Single Panel Simulation Parameters

parameter	symbol	value	units
semi-major axis	a	7178	km
eccentricity	e	0	\
inclination	i	70	deg
right ascension of the ascending node	Ω	0	deg
argument of periapsis	ω	0	deg
true anomaly at epoch	ν_0	90	deg

Table C.4: Orbit parameters for rigid body simulations

Flexible Spacecraft Model Simulation Parameters

parameter	symbol	value	units
semi-major axis	a	7178	km
eccentricity	e	0	
inclination	i	70	deg
right ascension of the ascending node	Ω	0	deg
argument of periapsis	ω	0	deg
true anomaly at epoch	ν_0	85	deg

Table C.5: Orbit parameters for flexible model simulations

parameter	symbol	value	unit
connection spring coefficient	k_s	1000	$\frac{\mathrm{N}}{\mathrm{m}}$
connection damping coefficient	c_s	5	$\frac{\mathrm{Ns}}{\mathrm{m}}$
torsional spring coefficient	k_t	0.1	$\frac{\mathrm{Nm}}{\mathrm{rad}}$
torsional damping coefficient	c_t	0.05	$\frac{\mathrm{Nms}}{\mathrm{rad}}$
hub mass	m_C	1000	kg
panel mass	m_i	50	kg
panel side length	L_i	2.5	m
hub side length	L_C	4	m

Table C.6: Spacecraft physical parameters

The moment of inertia matrix for each component is as follows:

$$\begin{aligned} I_C &= \mathrm{diag}\left(2400,\ 2400,\ 3600\right) \\ I_i &= \mathrm{diag}\left(25,\ 25,\ 50\right) \end{aligned}$$

parameter	symbol	value	units
hub proportional gain	K_p	0.8	/
hub derivative gain	K_ω	700	/
panel proportional gain	k_p	6.5×10^{-3}	/
panel derivative gain	k_ω	3	/
reaction wheel saturation	K_{rw}	0.05	Nm
torque rod saturation	K_{tr}	5×10^{-4}	Am^2

Table C.7: Section 4.4.1 Control parameters

C.3 Parameters Used in Chapter 5

parameter	symbol	value	unit
connection spring coefficient	k_s	1000	$\frac{\mathrm{N}}{\mathrm{m}}$
connection damping coefficient	c_s	5	$\frac{\mathrm{Ns}}{\mathrm{m}}$
torsional spring coefficient	k_t	0.1	$\frac{\mathrm{Nm}}{\mathrm{rad}}$
torsional damping coefficient	c_t	0.05	$\frac{\mathrm{Nms}}{\mathrm{rad}}$
hub mass	m_C	1000	kg
panel mass	m_i	100	kg
panel side length	L	2.5	m

Table C.8: 6x6 discretization DMD simulation parameters

parameter	symbol	value	unit
connection spring coefficient	k_s	1000	$\frac{\mathrm{N}}{\mathrm{m}}$
connection damping coefficient	c_s	5	$\frac{\mathrm{Ns}}{\mathrm{m}}$
torsional spring coefficient	k_t	0.1	$\frac{\mathrm{Nm}}{\mathrm{rad}}$
torsional damping coefficient	c_t	0.05	$\frac{\mathrm{Nms}}{\mathrm{rad}}$
hub mass	m_C	1000	kg
panel mass	m_i	11.11	kg
panel side length	L	0.83	m

Table C.9: 18x18 discretization DMD simulation parameters

DMD Kalman Filter Parameters

$$Q = 0.1\,\mathcal{I}_{nm\text{x}nm}$$

$$R = \begin{bmatrix} 0.01\,\mathcal{I}_{9x9} & 0 \\ 0 & 0.1\,\mathcal{I}_{m\text{x}m} \end{bmatrix}.$$

Bibliography

[1] Nicolo Woodward and Riccardo Bevilacqua. Onboard estimation of unknown dynamics of flexible spacecraft. *Acta Astronautica*, 217:363–381, 2024.

[2] S. Di Gennaro. Active vibration suppression in flexible spacecraft attitude tracking. *Journal of Guidance, Control, and Dynamics*, 21(3):400–408, May 1998.

[3] Reza Nadafi, Mansour Kabganian, Ali Kamali, and Mahboobeh Hossein Nejad. Super-twisting sliding mode control design based on lyapunov criteria for attitude tracking control and vibration suppression of a flexible spacecraft. *Measurement and Control*, 52(7-8):814–831, 2019.

[4] Ruidong Yan and Zhong Wu. Attitude stabilization of flexible spacecrafts via extended disturbance observer based controller. *Acta Astronautica*, 133:73–80, 2017.

[5] Ning Ji and Jinkun Liu. Distributed vibration control for flexible spacecraft with distributed disturbance and actuator fault. *Journal of Sound and Vibration*, 475:115274, 2020.

[6] Chenxing Zhong, Zhiyong Chen, and Yu Guo. Attitude control for flexible spacecraft with disturbance rejection. *IEEE Transactions on Aerospace and Electronic Systems*, 53(1):101–110, 2017.

[7] Guido Fracchia, James D. Biggs, and Matteo Ceriotti. Analytical low-jerk reorientation maneuvers for multi-body spacecraft structures. *Acta Astronautica*, 178:1–14, 2021.

[8] Mehdi Golestani, Majid Esmaeilzadeh, and Saleh Mobayen. Constrained attitude control for flexible spacecraft: attitude pointing accuracy and pointing stability improvement. *IEEE Transactions on Systems, Man, and Cybernetics: Systems*, 53(3):1566–1572, 2023.

[9] Wanwan Zhu, Qun Zong, Bailing Tian, and Wenjing Liu. Disturbance observer-based active vibration suppression and attitude control for flexible spacecraft. *IEEE Transactions on Systems, Man, and Cybernetics: Systems*, 52(2):893–901, 2022.

[10] Qinglei Hu and Bing Xiao. Intelligent proportional-derivative control for flexible spacecraft attitude stabilization with unknown input saturation. *Aerospace Science and Technology*, 23(1):63–74, Dec 2012.

[11] Gianluca Tagliani, Mauro Mancini, and Elisa Capello. Attitude control system design for multibody flexible spacecraft. In *2023 American Control Conference (ACC)*, pages 4820–4825, 2023.

[12] Ti Chen, Jinjun Shan, and Hao Wen. Distributed passivity-based control for multiple flexible spacecraft with attitude-only measurements. *Aerospace Science and Technology*, 94:105408, 2019.

[13] Umair Javaid, Ziyang Zhen, Sami Shahid, Dauda Sh Ibrahim, and Salman Ijaz. Output feedback attitude control of flexible spacecraft under actuator misalignment and input non-linearities. *Journal of Vibration and Control*, 30(7–8):1783–1801, Aug 2023.

[14] Zhaohui Wang, Ming Xu, Yinghong Jia, Shijie Xu, and Liang Tang. Vibration suppression-based attitude control for flexible spacecraft. *Aerospace Science and Technology*, 70:487–496, Nov 2017.

[15] Jixiang Fan and Di Zhou. Nonlinear attitude control of flexible spacecraft with scissored pairs of control moment gyros. *Journal of Dynamic Systems, Measurement, and Control*, 134(5):054502, 06 2012.

[16] Shunan Wu, Weimeng Chu, Xue Ma, Gianmarco Radice, and Zhigang Wu. Multi-objective integrated robust h∞ control for attitude tracking of a flexible spacecraft. *Acta Astronautica*, 151:80–87, 2018.

[17] Hiroshi Okubo and Shinsuke Kuwamoto. Agile attitude control and vibration suppression of flexible spacecraft using control moment gyros. *IFAC Proceedings Volumes*, 46(19):417–422, 2013. 19th IFAC Symposium on Automatic Control in Aerospace.

[18] Marco Sabatini, Giovanni B. Palmerini, Nazareno Leonangeli, and Paolo Gasbarri. Analysis and experiments for delay compensation in attitude control of flexible spacecraft. *Acta Astronautica*, 104(1):276–292, 2014.

[19] Linlin Hou and Haibin Sun. Anti-disturbance attitude control of flexible spacecraft with quantized states. *Aerospace Science and Technology*, 99:105760, 2020.

[20] Behrad Vatankhahghadim and Marco Lovera. Attitude control of flexible multibody spacecraft via shape change. *Journal of Guidance, Control, and Dynamics*, 47(5):995–1004, 2024.

[21] Xibin Cao, Chengfei Yue, and Ming Liu. Flexible satellite attitude maneuver via constrained torque distribution and active vibration suppression. *Aerospace Science and Technology*, 67:387–397, 2017.

[22] Jun Sun, Shuang Li, Jing Huang, and Dongfang Zhu. Robust coordinated control for large flexible spacecraft based on consensus theory. *Journal of the Franklin Institute*, 357(9):5359–5379, 2020.

[23] JoAnna Fulton and Hanspeter Schaub. Deployment dynamics analysis of an origami-folded spacecraft structure with elastic hinges. *Journal of Spacecraft and Rockets*, 59(2):401–420, 2022.

[24] Yizhe Zhang and Xin Guan. Active damping control of flexible appendages for spacecraft. *Aerospace Science and Technology*, 75:237–244, 2018.

[25] Quan Hu, Yinghong Jia, and Shijie Xu. Dynamics and vibration suppression of space structures with control moment gyroscopes. *Acta Astronautica*, 96:232–245, 2014.

[26] Xiao Feng, Yinghong Jia, and Shijie Xu. Dynamics of flexible multibody systems with variable-speed control moment gyroscopes. *Aerospace Science and Technology*, 79:554–569, 2018.

[27] Curtis Merrill and Derek A. Paley. Distributed control of the attitude and shape of a flexible spacecraft. *AIAA SCITECH 2023 Forum*, Jan 2023.

[28] P. Morin and C. Samson. Time-varying exponential stabilization of a rigid spacecraft with two control torques. *IEEE Transactions on Automatic Control*, 42(4):528–534, 1997.

[29] Hirohisa Kojima. Stabilization of angular velocity of asymmetrical rigid body using two constant torques. *Journal of Guidance, Control, and Dynamics*, 30(4):1163–1168, 2007.

[30] Panagiotis Tsiotras and James M. Longuski. Spin-axis stabilization of symmetric spacecraft with two control torques. *Systems & Control Letters*, 23(6):395–402, 1994.

[31] Katsuhiko Yamada, Ichiro Jikuya, and Okgyu Kwak. Rate damping of a spacecraft using two single-gimbal control moment gyros. *Journal of Guidance, Control, and Dynamics*, 36(6):1606–1623, 2013.

[32] Hirohisa Kojima. Backstepping-based steering control for spacecraft attitude control using two-skewed control moment gyroscopes. *Journal of Guidance, Control, and Dynamics*, 46(1):80–96, 2023.

[33] Chengfei Yue, Krishna Dev Kumar, Qiang Shen, Cher Hiang Goh, and Tong Heng Lee. Attitude stabilization using two parallel single-gimbal control moment gyroscopes. *Journal of Guidance, Control, and Dynamics*, 42(6):1353–1364, 2019.

[34] Robert J. Mcelvain. Satellite angular momentum removal utilizing the earth's magnetic field. *Applied Mathematics and Mechanics*, page 137–158, 1964.

[35] P. J. Camillo and F. L. Markley. Orbit-averaged behavior of magnetic control laws for momentum unloading. *Journal of Guidance and Control*, 3(6):563–568, 1980.

[36] Marco Lovera. Optimal magnetic momentum control for inertially pointing spacecraft. *European Journal of Control*, 7(1):30–39, 2001.

[37] Giulio Avanzini and Fabrizio Giulietti. Magnetic detumbling of a rigid spacecraft. *Journal of Guidance, Control, and Dynamics*, 35(4):1326–1334, 2012.

[38] Marco Lovera. Magnetic satellite detumbling: The b-dot algorithm revisited. *2015 American Control Conference (ACC)*, 2015.

[39] M. Yu. Ovchinnikov, D.S. Roldugin, S.S. Tkachev, and V.I. Penkov. B-dot algorithm steady-state motion performance. *Acta Astronautica*, 146:66–72, 2018.

[40] Yaguang Yang. Controllability of spacecraft using only magnetic torques. *IEEE Transactions on Aerospace and Electronic Systems*, 52(2):954–961, 2016.

[41] Rafał Wiśniewski and Mogens Blanke. Fully magnetic attitude control for spacecraft subject to gravity gradient. *Automatica*, 35(7):1201–1214, 1999.

[42] Ping Wang and Yuri Shtessel. Satellite attitude control using only magnetic torquers. In *Guidance, Navigation, and Control Conference and Exhibit*, page 4430, 1998.

[43] Mohammad Abdelrahman, Insu Chang, and Sang-Young Park. Magnetic torque attitude control of a satellite using the state-dependent riccati equation technique. *International Journal of Non-Linear Mechanics*, 46(5):758–771, 2011.

[44] J. Kulkarni and M. Campbell. An approach to magnetic torque attitude control of satellites via 'h/sub /spl infin//' control for ltv systems. In *2004 43rd IEEE Conference on Decision and Control (CDC) (IEEE Cat. No.04CH37601)*, volume 1, pages 273–277 Vol.1, 2004.

[45] Koki Kimura, Yasuhiro Shoji, Satoshi Satoh, and Katsuhiko Yamada. Attitude control experiment of a spinning spacecraft using only magnetic torquers. *Advances in Space Research*, 71(12):5386–5399, 2023.

[46] Javier Cubas and Anton de Ruiter. Magnetic control without attitude determination for spinning spacecraft. *Acta Astronautica*, 169:108–123, 2020.

[47] Huaizu You, Ying-Wen Jan, and Jih-Run Tsai. Sun pointing attitude control with magnetic torquers only. In *57th International Astronautical Congress*, pages C1–2, 2006.

[48] Javier Cubas, Assal Farrahi, and Santiago Pindado. Magnetic attitude control for satellites in polar or sun-synchronous orbits. *Journal of Guidance, Control, and Dynamics*, 38(10):1947–1958, 2015.

[49] Giulio Avanzini, Emanuele L. de Angelis, and Fabrizio Giulietti. Acquisition of a desired pure-spin condition for a magnetically actuated spacecraft. *Journal of Guidance, Control, and Dynamics*, 36(6):1816–1821, 2013.

[50] Mohammed A. A. Desouky and Ossama Abdelkhalik. Improved spacecraft magnetic attitude maneuvering. *Journal of Spacecraft and Rockets*, 56(5):1611–1623, 2019.

[51] Fabio Celani. Spacecraft attitude stabilization using magnetorquers with separation between measurement and actuation. *Journal of Guidance, Control, and Dynamics*, 39(9):2184–2191, 2016.

[52] Everett J. Findlay, Anton de Ruiter, James R. Forbes, Hugh H. T. Liu, Christopher J. Damaren, and James Lee. Magnetic attitude control of a flexible satellite. *Journal of Guidance, Control, and Dynamics*, 36(5):1522–1527, 2013.

[53] Kota Kondo, Ilya Kolmanovsky, Yasuhiro Yoshimura, Mai Bando, Shuji Nagasaki, and Toshiya Hanada. Nonlinear model predictive detumbling of small satellites with a single-axis magnetorquer. *Journal of Guidance, Control, and Dynamics*, 44(6):1211–1218, 2021.

[54] Mike Alger and Anton de Ruiter. Magnetic spacecraft attitude stabilization with two torquers. *Acta Astronautica*, 192:157–167, 2022.

[55] Curtis Merrill and Derek A. Paley. Lyapunov-based two-axis magnetic attitude control of a rigid spacecraft. *AIAA SCITECH 2024 Forum*, Jan 2024.

[56] Matthew Brownell, Andrew J. Sinclair, and Puneet Singla. A subspace method for shape estimation of flexible spacecraft membrane. *AIAA SCITECH 2022 Forum*, Jan 2022.

[57] Thibaud Talon, Yulu Luke Chen, and Sergio Pellegrino. Shape reconstruction of planar flexible spacecraft structures using distributed sun sensors. *Acta Astronautica*, 180:328–339, 2021.

[58] M.D. Lichter and S. Dubowsky. Shape, motion, and parameter estimation of large flexible space structures using range images. In *Proceedings of the 2005 IEEE International Conference on Robotics and Automation*, pages 4476–4481, 2005.

[59] Toshio Kashiwase, Masaki Tabata, Kazuo Tsuchiya, and Sadao Akishita. Shape control of flexible structures. *Journal of Intelligent Material Systems and Structures*, 2(1):110–125, 1991.

[60] L.W. Taylor and J.L. Williams. Maximum likelihood estimation for distributed parameter models of flexible spacecraft. *IFAC Proceedings Volumes*, 21(9):415–420, 1988. 8th IFAC/IFOORS Symposium on Identification and System Parameter Estimation 1988, Beijing, PRC, 27-31 August.

[61] Olga-Orsalia Christidi-Loumpasefski, Kostas Nanos, and Evangelos Papadopoulos. On parameter estimation of flexible space manipulator systems. In *2020 IEEE/RSJ International Conference on Intelligent Robots and Systems (IROS)*, pages 1843–1848, 2020.

[62] Zhiyu Ni, Ruinan Mu, Guangbin Xun, and Zhigang Wu. Time-varying modal parameters identification of a spacecraft with rotating flexible appendage by recursive algorithm. *Acta Astronautica*, 118:49–61, 2016.

[63] Miha Rot, Martin Horvat, and Gregor Kosec. Dynamic mode decomposition as an analysis tool for time-dependent partial differential equations. *2022 7th International Conference on Smart and Sustainable Technologies (SpliTech)*, Jul 2022.

[64] Jonathan H. Tu, Clarence W. Rowley, Dirk M. Luchtenburg, Steven L. Brunton, and J. Nathan Kutz. On dynamic mode decomposition: Theory and applications. *Journal of Computational Dynamics*, 1(2):391–421, 2014.

[65] Nathan J. Kutz, Steven L. Brunton, Bingni W. Brunton, and Joshua L. Proctor. *Dynamic mode decomposition: Data-driven modeling of Complex Systems*. Society for industrial and applied mathematics, 2016.

[66] Amit Surana and Andrzej Banaszuk. Linear observer synthesis for nonlinear systems using koopman operator framework. *IFAC-PapersOnLine*, 49(18):716–723, 2016. 10th IFAC Symposium on Nonlinear Control Systems NOLCOS 2016.

[67] Nalin A. Chaturvedi, Amit K. Sanyal, and N. Harris McClamroch. Rigid-body attitude control. *IEEE Control Systems Magazine*, 31(3):30–51, 2011.

[68] Bong Wie. *Space Vehicle Dynamics and Control*. American Institute of Aeoronautics and Astronautics, Inc., 2008.

[69] Mark L. Psiaki. Magnetic torquer attitude control via asymptotic periodic linear quadratic regulation. *Journal of Guidance, Control, and Dynamics*, 24(2):386–394, 2001.

[70] Daniel F. Gomez, Francis D. Lagor, Phillip B. Kirk, Andrew H. Lind, Anya R. Jones, and Derek A. Paley. Data-driven estimation of the unsteady flowfield near an actuated airfoil. *Journal of Guidance, Control, and Dynamics*, 42(10):2279–2287, Oct 2019.

[71] John L. Crassidis and John L. Junkins. *Optimal Estimation of Dynamic Systems*. CRC Press, 2012.

[72] Taeyoung Lee. Robust global exponential attitude tracking controls on so(3). *American Control Conference*, 2013.

[73] Arthur J. Krener and Kayo Ide. Measures of unobservability. In *Proceedings of the 48th IEEE Conference on Decision and Control (CDC) held jointly with 2009 28th Chinese Control Conference*, pages 6401–6406, 2009.

[74] Hassan K. Khalil. *Nonlinear systems*. Prentice Hall, 2002.